NASA Technical Memorandum 4085

Research Highlights of the Global Modeling and Simulation Branch for 1986–1987

Edited by
Wayman Baker
Goddard Space Flight Center
Greenbelt, Maryland

Co-editors:
Joel Susskind
Goddard Space Flight Center
Greenbelt, Maryland

James Pfaendtner
Sigma Data Services Corporation
Reston, Virginia

David Randall and Robert Atlas
Goddard Space Flight Center
Greenbelt, Maryland

National Aeronautics
and Space Administration

Scientific and Technical
Information Division

1988

FOREWORD

The Global Modeling and Simulation Branch has been the focal point for global weather and climate prediction research in the Laboratory for Atmospheres at the Goddard Space Flight Center for the past 10 years. Through the retrieval and use of satellite data, the development of global models and data assimilation techniques, the simulation of future observing systems, and the performance of atmospheric diagnostic studies, significant advances have been made in our understanding and ability to predict the atmosphere. From this global research perspective and with ongoing collaborative efforts with scientists outside the Branch in the development of coupled models of the atmosphere and oceans and the atmosphere and biosphere, the Branch should play a pivotal role in Eos (Earth Observing System), NASA's program for studying global change.

This document provides a synopsis of the research conducted in the Global Modeling and Simulation Branch and highlights the most significant accomplishments in 1986-87. It is hoped that those individuals who might be contemplating postdoctoral or visiting scientist appointments with the Branch will find the research topics highlighted here to be as exciting as do those of us in the Branch pursuing them.

Wayman Baker
Global Modeling and Simulation Branch
February 1988

RESEARCH HIGHLIGHTS OF THE GLOBAL MODELING AND SIMULATION BRANCH FOR 1986 - 1987

FOREWORD - W. Baker

I. INTRODUCTION - W. Baker 1

II. SATELLITE RETRIEVAL RESEARCH - J. Susskind (Editor) 2

Physically Based Retrievals 2

Interactive Analysis/Forecast/Retrieval System 3

Retrievals of Total O_3 Burden 10

Computation of Outgoing Longwave Radiation 14

Precipitation Estimates Derived from HIRS2/MSU Soundings 22

Results Depicting the 1979 FGGE Year 25

III. NUMERICAL WEATHER PREDICTION - J. Pfaendtner (Editor) 28

Fourth-Order Model Development (H. M. Helfand, Y. Sud) 28

Four-Dimensional Data Assimilation (W. Baker, S. Bloom, J. Pfaendtner) 38

Stratospheric/Tropospheric Data Assimilation System (W. Baker, K. Takano) 40

Numerical Prediction Experiments Related to the Summer 1980 U.S. Heat Wave (R. Atlas, N. Wolfson, Y. Sud) 41

Global Surface Wind and Flux Fields from the Assimilation of Seasat Data (R. Atlas, A. J. Busalacchi, S. Bloom, M. Ghil, E. Kalnay) 43

IV. CLIMATE RESEARCH HIGHLIGHTS - D. Randall (Editor) 47

Cloud-Climate Studies (D. Randall) 47

Atmosphere-Ocean Interactions (M. Suarez) 50

Atmosphere-Land Surface Interactions (Y. Sud) 52

Seasonal Cycle Simulation Studies (D. Straus) 55

V. OBSERVING SYSTEM SIMULATION EXPERIMENTS - R. Atlas (Editor) 59

Background 59

Current Simulation Studies 63

Recent Results 65

I. INTRODUCTION (W. Baker)

Since its inception in 1977, the Global Modeling and Simulation Branch has led the global weather and climate prediction research in the Laboratory for Atmospheres (formerly Laboratory for Atmospheric Sciences) at the Goddard Space Flight Center. In the first few years, the numerical weather prediction effort in the Branch was focused on the testing and evaluation of NOAA operational satellite temperature soundings in atmospheric general circulation models (GCM's) for the purpose of extending weather forecast skill. This rather limited use of satellite data has evolved to a highly sophisticated research program aimed at furthering our understanding and prediction of weather and climate with the utilization of satellite data now an integral part of the effort.

Today, we are using satellite temperature soundings produced with a physically-based retrieval system developed in the Branch (see Section II). Generating these retrievals interactively as part of a data assimilation system not only produces accurate temperature soundings, but also a broad range of geophysical parameters (e.g., land and sea surface temperature, ice and snow extent, cloud height and amount, precipitable water, total ozone burden, outgoing longwave radiation, and precipitation). These kinds of data, which are already being used in the preparation of boundary conditions for various model integrations, in the evaluation of climate simulations, and in trying to understand the reasons for the depletion of ozone over the Antarctic, should be extremely valuable in investigating global change under the Eos (Earth Observing System) program.

As mentioned above, satellite temperature soundings are produced interactively as part of the data assimilation system. This capability, which is unique to the Branch's numerical weather prediction effort, is discussed in Section III. Another unique data assimilation capability is the development of a coupled stratospheric/tropospheric assimilation system extending up to 0.4 mb which is also described in Section III.

Climate research conducted in the Global Modeling and Simulation Branch includes a wide variety of topics. Section IV presents the highlights from some of these including cloud-climate studies, coupled ocean-atmosphere experiments, earth-atmosphere interaction studies, and seasonal cycle simulation experiments.

Finally, in addition to the global modeling, satellite retrieval algorithm development, and data assimilation research conducted in the Branch, which are highly relevant to Eos, a comprehensive program is underway to conduct observing system simulation experiments for proposed future instruments (discussed in Section V). This effort, which is in collaboration with the European Centre for Medium Range Weather Forecasts (ECMWF), should help to insure that *those things needed* to advance our current modeling and prediction capabilities are given the highest priority.

II. SATELLITE RETRIEVAL RESEARCH (J. Susskind)

Physically-Based Retrievals

Research in satellite retrievals is oriented primarily toward the development of improved techniques for determination of geophysical parameters from observations taken by the HIRS2 (High resolution Infra-red Radiation Sounder 2) and MSU (Microwave Sounding Unit) on the NOAA operational satellites, and toward the utilization of the fields of geophysical parameters derived from the satellite soundings in weather and climate research.

HIRS2 and MSU are the 20 channel infra-red and 4 channel microwave passive sounders on the operational low earth orbiting satellites. They monitor emission arising primarily from the earth's surface and the atmosphere up to the mid stratosphere. These, together with the SSU (Stratospheric Sounding Unit), a three channel pressure modulated infra-red radiometer, which monitors emission from the middle and upper stratosphere, comprise the TOVS system (TIROS Operational Vertical Sounder).

The TOVS data are analyzed operationally by the NOAA National Environmental Satellite and Data Information Service (NESDIS) to produce vertical temperature and humidity profiles using a method based primarily on statistical regression relationships between observed radiances and atmospheric parameters. The approach used at GLA is fundamentally different from the current operational approach. Rather than rely on empirical relationships between observations and meteorological conditions, we attempt to find surface and atmospheric conditions which match the observations to a specified amount, when substituted into the radiative transfer equations describing the dependence of the observations on the meteorological conditions. A physically-based method easily allows for incorporation of model forecast information to help improve the retrievals. This produces not only a better set of retrievals, but also results in better analyses and forecasts, as discussed below. In addition, a physically-based system has the ability to correct for the effects of auxiliary factors such as total ozone, surface temperature, surface emissivity, surface elevation, reflected solar radiation, satellite zenith angle, and most significant of all, clouds. All of these parameters are either solved for, or directly accounted for, together with the atmospheric temperature and humidity profiles, in an iterative fashion. As a result of this, the data have been analyzed to produce not only atmospheric temperature and humidity profiles globally, which can be used for initialization of atmospheric general circulation models, but also to produce the following fields: total ozone burden of the atmosphere; sea/land surface temperature and their day-night difference which, over land, is related to soil moisture; fractional cloud cover, cloud top temperature, and cloud top pressure and their day-night differences; and ice and snow cover, which is derived from the combined use of the surface emissivity at 50.3 GHz and the ground temperature. Fields of outgoing longwave radiation and estimates of precipitation have also been computed based on the retrieved surface and atmospheric geophysical parameters.

One of the crucial elements in the physical retrieval scheme is the ability to accurately compute radiances which the instrument would see as a function of atmospheric and surface conditions. The details of the calculation of channel-averaged radiances as a function of atmospheric temperature-humidity-ozone profiles, surface temperature, elevation, emissivity, and zenith angle of observation are described in Susskind *et al.* (1983). The basic retrieval scheme is described in Susskind *et al.* (1984), with improvements in the determination of surface temperature described in Susskind and Reuter (1985). Improvements in the determination of cloud fields are described in Susskind *et al.* (1987), and a description of a new humidity algorithm is given in Reuter *et al.* (1988).

The most recent developments have been with regard to retrieval of total O_3 burden, computation of outgoing longwave radiation (OLR) and precipitation estimates from the HIRS2/MSU soundings, and various items related to the development and implementation of the GLA interactive analysis/forecast/retrieval system, which has been used to process data for the whole FGGE year, December 1978 - November 1979.

Interactive Analysis/Forecast/Retrieval System

One of our major research efforts has been the development of an interactive analysis/forecast/retrieval system which is an automated system to produce satellite retrievals, global analyses, and six-hour forecasts in an interactive fashion. The system was designed for long term use and so far has been used to process the entire FGGE year. The current interactive assimilation system is envisioned as the prototype of the one required for Eos (see Section III.) It was also used to produce near real time (same day) retrievals and analyses for the period August-September 1987 in conjunction with the experiment to monitor the "ozone hole" over Antarctica.

In each six hour period, the interactive cycle starts with the 6-hour forecast field generated by the GCM (Kalnay *et al.*, 1983). The 6-hour forecast temperature and humidity profiles are used as an initial guess for all soundings occurring in the interval ± 3 hours of the forecast time. An SCM analysis (Baker, 1983) is then performed using the satellite soundings and all other information measured in the time interval (such as radiosonde and ship reports, etc.). While satellite soundings of all the previously mentioned variables are produced in the 6 hour period, only retrieved atmospheric thicknesses have been assimilated at this time. Research is being done regarding assimilation of satellite-derived humidity profiles and sea-surface temperatures. The retrieved atmospheric thicknesses are assimilated over both continental and oceanic areas, but are weighted in the analysis with weights which decrease with increasing retrieved cloudiness and which are larger over ocean than over land. This differs from procedures used operationally at NMC and ECMWF which do not assimilate any soundings over land.

It is felt that using the same 6 hour forecast field as a first guess for the retrievals and also as first guess for the analysis is advantageous for the analysis and subsequent forecast. It is true that to some extent retrieval errors are correlated with forecast errors, which must be accounted for in the analysis. On the other hand, after the system has achieved a balance, the retrievals generally improve, but do not differ significantly from the 6-hour first guess. Therefore, the modifications to the first guess from the point of view of the analysis are small and allow for a better dynamic balance in the initial conditions for the next six-hour forecast. Satellite retrievals which differ significantly from the forecast field used to initialize the analysis not only disturb the dynamic balance of the forecast field, but also are likely to be rejected to some extent by the analysis procedure.

Development of this interactive system involved interfacing the retrieval program with the GLA GCM and the SCM analysis scheme and speeding up the retrieval production (50,000 retrievals per day per satellite are now done in 30 minutes CPU on the Cyber 205). An automated systematic error correction scheme, which insures unbiased retrievals throughout the whole year with no outside intervention, also had to be developed and implemented.

The GLA retrieval system computes brightness temperatures for the sounding channels utilizing a first guess profile, compares the computed brightness temperatures to the observations, and modifies the first guess according to the above differences and the derivative of the computed brightness temperatures with respect to changes in the temperature profile (Susskind et al., 1983, 1984). The ability to compute accurate brightness temperatures as a function of surface and atmospheric conditions is crucial to the success of a physically-based method. In particular, one must guard against systematic differences between observed and computed brightness temperatures. Such differences can arise from systematic computation errors, systematic observation (calibration) errors, or a combination of both. Removal of these biases is referred to as tuning, and is an integral part of the retrieval program. Radiances computed with the global six-hour forecast first guess are compared to the observations in order to generate empirical bias correction coefficients. The global six-hour forecast first guess is taken as "truth" to the extent that it is assumed to be unbiased, though not necessarily accurate. In the course of producing a retrieval, the cloud fraction and ground temperature are routinely determined and radiances are computed for the temperature sounding channels using the retrieved ground temperature and the first guess profile. These computed radiances are then used for comparisons with the observations to modify the atmospheric profiles. The same comparisons are also used to generate the bias coefficients. Comparisons are done only in cases determined to be clear and in cases for which the final retrieval is accepted and not changed appreciably from the first guess. This latter criterion is added to remove cases with a very bad first guess, and the first criterion eliminates problems with clouds and other nonhomogeneities in the scene.

Even using this tuning procedure, comparison of retrievals with radiosonde reports showed small biases at different pressure levels. These were of an oscillatory nature similar in form to the empirical orthogonal functions used as a constraint on the solution (Susskind et al., 1984). These retrieval biases, which changed only very slowly with time, did not respond to changes in tuning. They were removed in the retrieval program by subtracting biases as a function of pressure computed from the previous run (typically 2 days long), and from the retrievals for the following time period.

A comparison of retrieval and forecast first guess temperature profile accuracies obtained from the interactive cycle using the automated bias correction is given in Figures 1 and 2 for a winter and a summer month of FGGE. Co-locations are for all oceanic radiosondes within 110 km and 6 hours of the satellite soundings. It is apparent that while the six hour forecast guess, resulting from the interactive analysis system, is very good at all

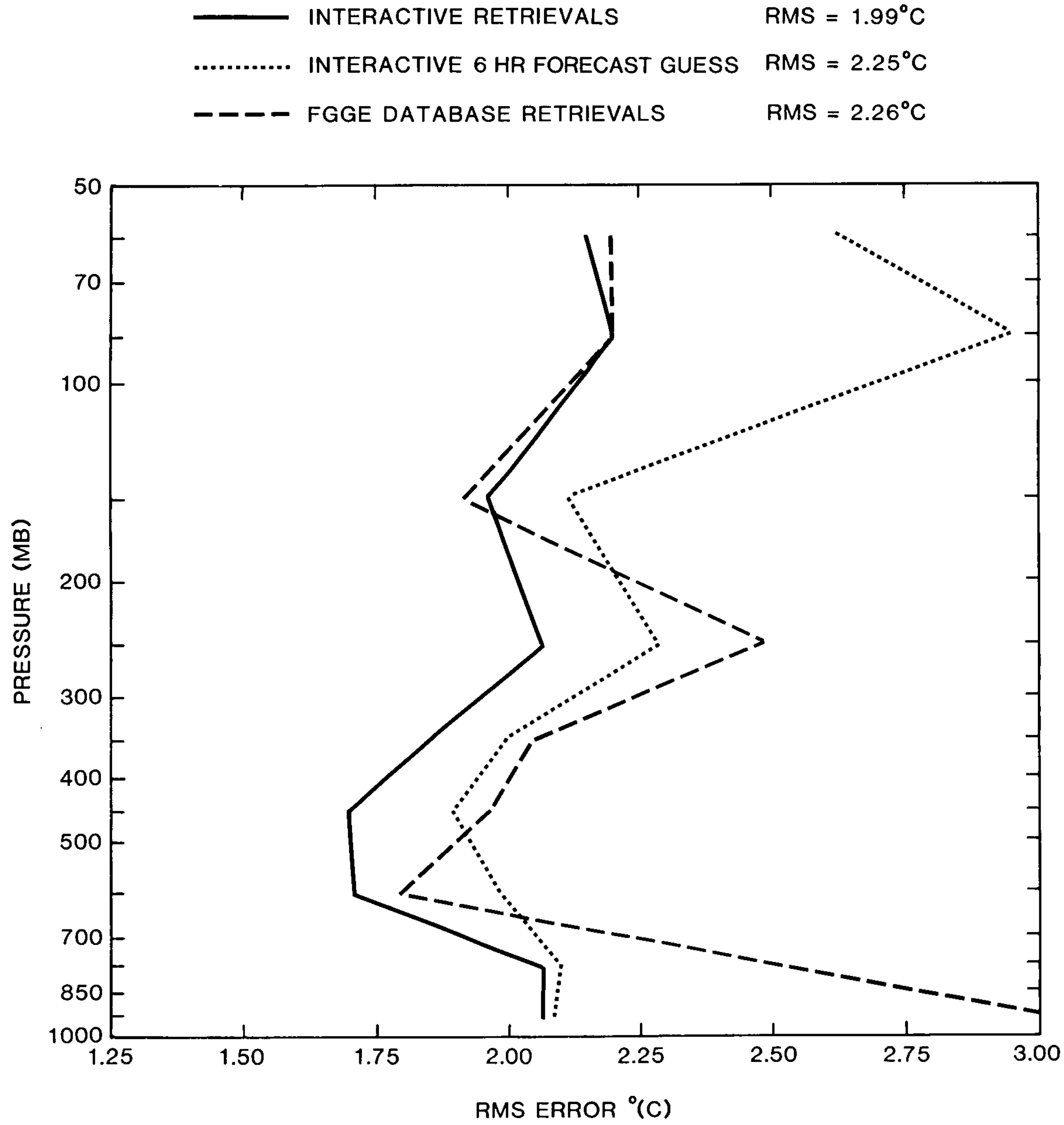

Figure 1 RMS layer mean temperature errors compared to co-located oceanic radiosondes for GLA interactive retrievals, GLA interactive first guess, and FGGE database retrievals for February 1-February 28, 1979.

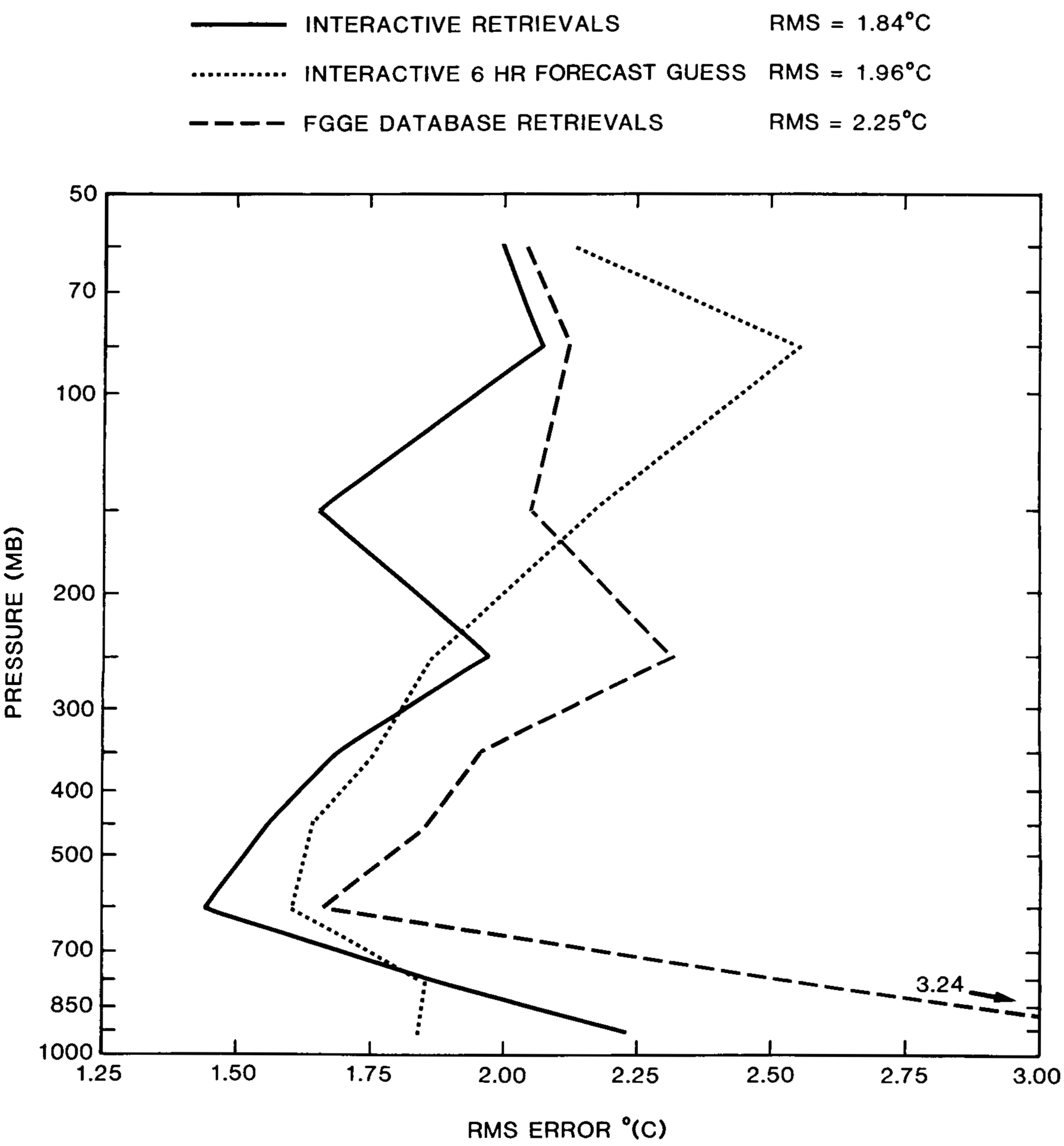

Figure 2 As in Figure 1 for July 1- July 31, 1979.

levels, the retrievals further improve the forecast in the middle and upper atmosphere. In fact, the accuracy of both the forecast and the retrievals improve throughout the course of the year. The results shown are for retrievals and forecasts in the vicinity of radiosondes, where the forecasts are expected to be most accurate, often having had the benefit of a previous radiosonde report within 6-12 hours. Reuter et al. (1988) showed that temperature retrievals degrade much more slowly than the first guess. Therefore, one would expect larger improvements in the forecast temperature profiles, and hence, in the subsequent analyses in areas away from radiosondes where the forecast is likely to be poorer. Also included in Figures 1 and 2 are the RMS errors of the FGGE retrievals (produced by NOAA NESDIS) for the same periods. It is clear that the accuracy of the FGGE retrievals is poorer than that of either the GLA retrievals or the interactive forecast itself. Hence, the FGGE retrievals may not produce as accurate an analysis when used to initialize the model as the GLA retrievals.

One way of judging the quality of an analysis is the accuracy of a forecast generated from it. A number of 5 day forecasts have been run from analyses using the interactive system with the GLA retrievals and compared with those produced from a forecast/analysis cycle utilizing the standard FGGE retrievals, which is otherwise identical with respect to the data used in the interactive cycle. Both sets of forecasts have been verified against the ECMWF analysis. Figure 3 shows the average anomaly correlation score for 13 five day (a) 500 mb height and (b) sea level pressure forecasts, verified over the northern hemisphere extratropics, taken from the period January 9 to March 2, 1979 (every 4 days of FGGE SOP 1 except February 22 and 26, for which verification was lacking). It is clear that the average forecast anomaly correlation of the interactive forecasts are superior to those of the forecasts initialized using the standard FGGE soundings. The interactive forecasts exhibit an improvement in all individual regions, but the improvement in forecast skill is largest when verified over Europe, as shown in Figure 4a, in which the regime of skillful 500 mb height forecasts, which is indicated by an anomaly correlation greater than 0.6, is extended roughly 6 hours to a period of 5 days using the interactive analysis. Figure 4b shows the 500 mb height anomaly correlation score, comparing the forecasts over Europe initialized with the interactive analysis with those initialized with an analysis having no satellite data. It is apparent that the satellite data improve the forecast (Figure 4b), and the improvement has been enhanced after 4 days by using the interactive retrievals in place of the FGGE retrievals (Figure 4a).

Atmospheric humidity profiles are much more difficult to determine with high precision than are temperature profiles. This is because the sensitivity of the radiances to water vapor distribution in different atmospheric levels is roughly proportional to the difference between the temperatures of the water vapor in the atmospheric level and the surface temperature. Therefore, sensitivity to low level humidity is reduced. Reuter et al. (1988) have shown that retrieved humidity beneath 700 mb is very sensitive to the first guess profile, but retrievals can improve on the first guess at low levels if the guess is relatively poor. Table 1 shows winter and summer RMS errors compared to co-located radiosondes of retrieved and first guess precipitable water. Also shown in parentheses is the error expressed as the mean value of the radiosonde reports. Statistics are shown for precipitable water in three atmospheric layers and for the total atmosphere.

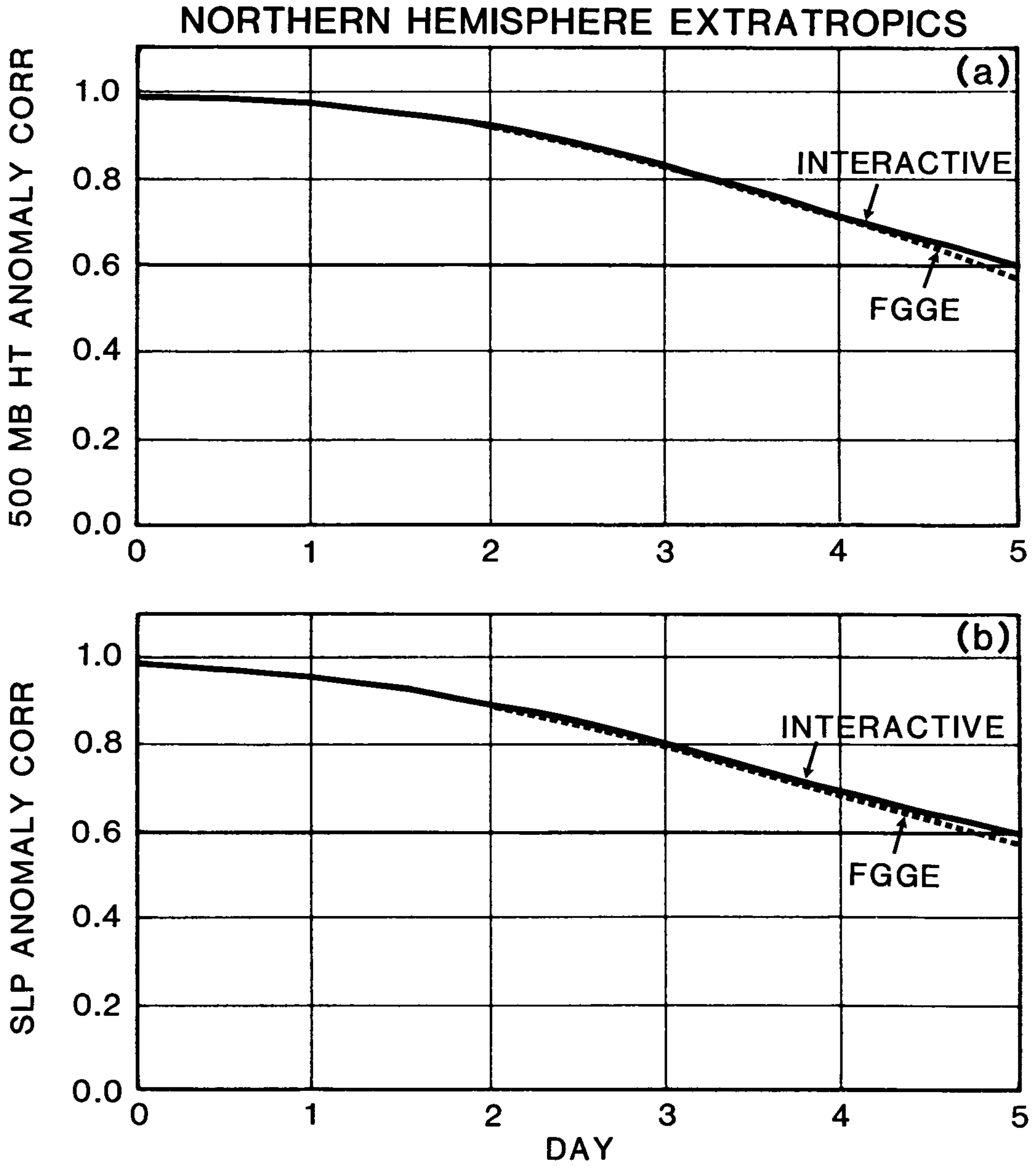

Figure 3 (a) 500 mb height anomaly correlation coefficients averaged for 13 1-5 day GLA GCM forecasts in SOPI, verified over the Northern Hemisphere extratropics against the ECMWF analysis, initialized utilizing either the full FGGE database, or the full FGGE database, but using GLA interactive retrievals in place of FGGE retrievals. (b) As in (a) but for sea level pressure anomaly correlation coefficients.

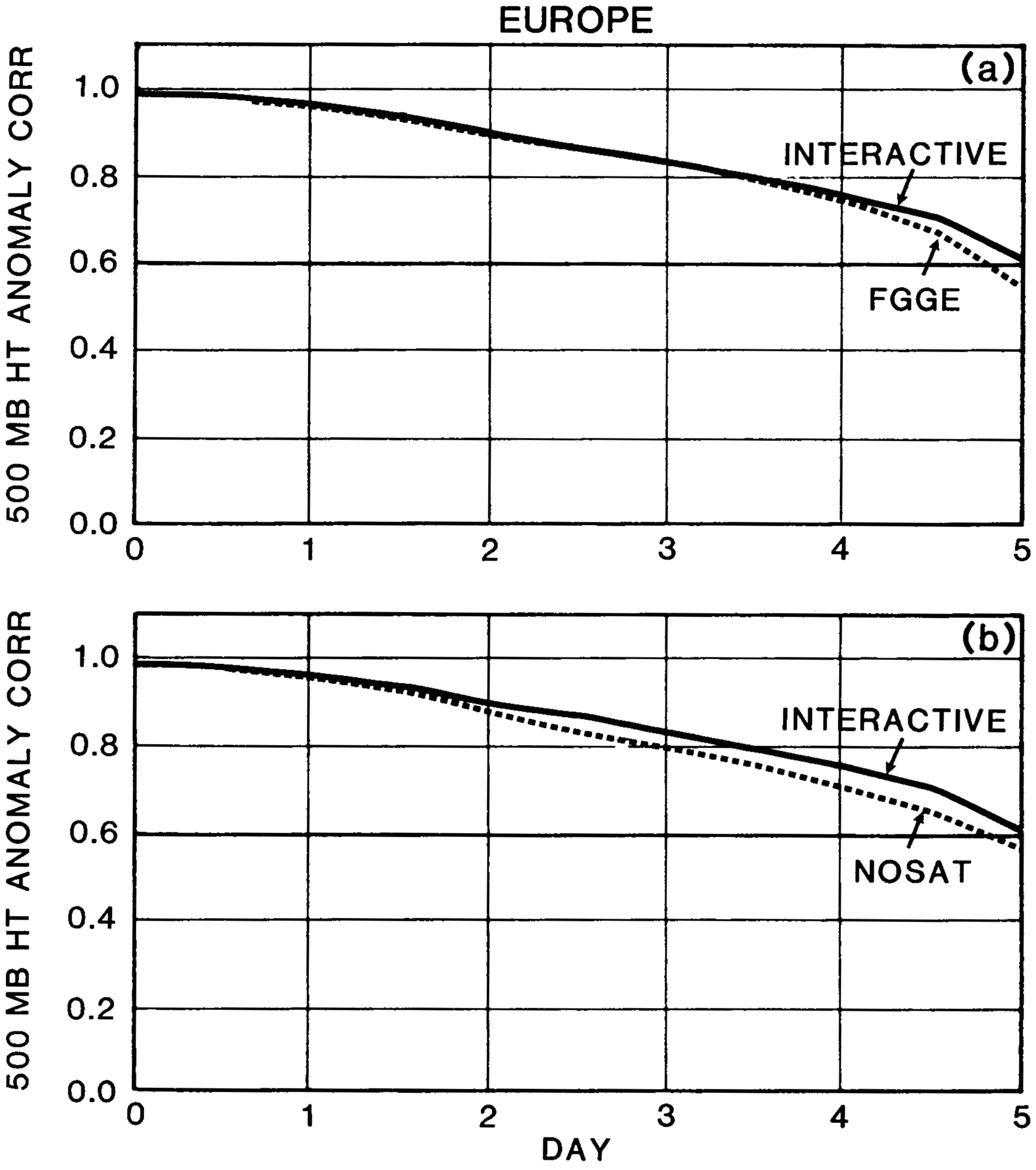

Figure 4 (a) As in Figure 3(a), but verified only over Europe. (b) As in (a), but with statistics for forecasts initialized utilizing no satellite data in place of those using the full FGGE database.

TABLE 1

RMS ERRORS (MM) OF LAYER PRECIPITABLE WATER COMPARED TO GLOBAL OCEANIC RADIOSONDES ± 6 HRS ± 110 KM

	FEB 1 - FEB 28 1979		JULY 1 - JULY 31 1979	
LAYER (MB)	FORECAST	RETRIEVAL	FORECAST	RETRIEVAL
1000-700	7.70 (30.4%)	7.68 (30.2%)	8.99 (31.8%)	8.88 (31.4%)
700-500	2.36 (49.5%)	2.22 (46.5%)	2.72 (40.2%)	2.68 (39.6%)
500-300	0.99 (70.2%)	0.89 (63.1%)	1.42 (68.6%)	1.06 (51.2%)
1000-1	8.82 (29.2%)	8.22 (27.2%)	10.46 (29.5%)	9.48 (26.7%)

It is apparent that the retrievals improve the model first guess, but only slightly at the lowest level with increasing amounts at higher levels. The total precipitable water is retrieved to an accuracy of about ±27%. Part of this error is most likely due to sampling differences in space and time between the radiosonde point measurement and the satellite area measurement.

Retrievals of Total O_3 Burden

The total ozone content of the atmosphere is an important variable for at least two reasons, indicative of both stratospheric and tropospheric processes. The ozone content of the stratosphere is determined by photochemical processes dependent on the amount of sunlight and various trace constituents. Long term trends of total ozone, as well as the annual cycle, are measures of natural phenomena, as well as the effects of the accumulation of man-made trace constituents upon the ozone layer in the stratosphere. The total ozone content is also indicative of the depth of the ozone rich stratosphere, or equivalently, the height of the tropopause. This is related to the tropospheric air mass and is a useful quantity in monitoring air mass and in improving the sounding accuracy of remote sensors.

Ozone has been monitored almost exclusively, whether from the ground or space, using measurements at ultra-violet frequencies. For example, the Total Ozone Mapping Spectrometer (TOMS) and Solar Backscatter Ultra-Violet (SBUV) instruments monitor total radiation backscattered by the atmosphere in frequencies sensitive to ozone absorption. Consequently, these measurements can be taken only during the day, and in polar regions, only during the summer half of the year. HIRS2 has a channel in the 9.6µm ozone absorption band. Radiances in this channel are sensitive to total ozone absorption, but are also sensitive to the ground temperature and atmospheric temperature-humidity profile, as well as cloud characteristics. Therefore, all of these factors must be accounted for accurately before accurate total O_3 soundings can be performed. There is no constraint on the location of the sun in the analysis, and hence, soundings can be produced day and night, as well as all year in polar regions. This gives the potential of twice daily monitoring of the total ozone as well as the ability to study for the first time the entire winter portion of the ozone annual cycle in the polar regions.

The ozone retrieval is performed as part of the GLA retrieval process (Susskind et al., 1984; Reuter et al., 1988) after the surface temperature and atmospheric temperature-humidity profiles have been retrieved. The method of retrieving ozone is analogous to the retrieval of humidity, but only one channel is used in a manner which scales the entire first guess ozone profile taken to be zonally-averaged climatology. The retrieved field of total O_3 for June 11, 1979 0Z ±12 hours is shown in Figure 5a. Black areas mean no O_3 soundings were obtained in a given 4° x 5° latitude-longitude bin during the 24 hour period, either because no satellite data were present or all retrievals were rejected. It is apparent that single day retrieval coverage is quite good (provided orbits are not missing as often occurs) even in areas of extensive cloudiness. The atmospheric circulation is clearly depicted in the total O_3 fields, with high values generally indicating a polar air-mass and low values a tropical air mass. This relationship is quite apparent when comparing Figure 5a with Figure 5b, which shows retrieved 500-1000 mb thickness for the same period. In fact, the thermal fronts are more sharply depicted in both the northern and southern hemispheres in the O_3 field than in the height field. We are currently examining ways of incorporating the O_3 information into the analysis procedure.

While single day O_3 fields clearly show synoptic features, long term mean values average out these tropospheric phenomena and are indicative of trends of O_3 concentrations in the stratosphere. Figure 6a shows zonal mean values of total O_3 determined from analysis of HIRS2/MSU data for every 1/3 of a month from December 21, 1978 to November 30, 1979. The TOMS zonal mean field for 1979 is shown in Figure 6b. Values are absent in the polar winter because of the lack of sunlight. Comparison of Figures 6a and 6b indicates reasonable agreement of TOMS and HIRS data. The HIRS values in the polar winter also appear reasonable, but there is no basis for comparison.

Tropical values in both fields are uniformly low and ozone generally increases polewards, especially in the northern hemisphere winter and spring. The southern hemisphere shows an interesting structure in late winter and spring (August-October) in which a strong maximum occurs at about 50° south latitude coupled with an intense minimum at about 70° south. This latter feature is known as the "ozone hole" which occurs every year at this time. Total ozone has been continuously monitored by TOMS since 1979 and the zonal mean values of the ozone minimum in the "hole" have decreased from 260 Dobson units in 1979 to 150 Dobson units in 1985. The reason for this is unknown and is cause for much interest and concern.

An aircraft experiment was conducted in the period August 17, 1987 - September 28, 1987 to monitor O_3 and other atmospheric species involved in the O_3 photochemical cycle in the region of the O_3 minimum. Flights went from Punta Arenas, Chile to the Antarctica and back. TOMS was the main instrument used to monitor O_3 from space in this experiment, but we also provided back-up O_3, temperature, and cloud data in near real time with the HIRS2/MSU system. These data may shed some light on the factors affecting total O_3 in the south polar winter and spring.

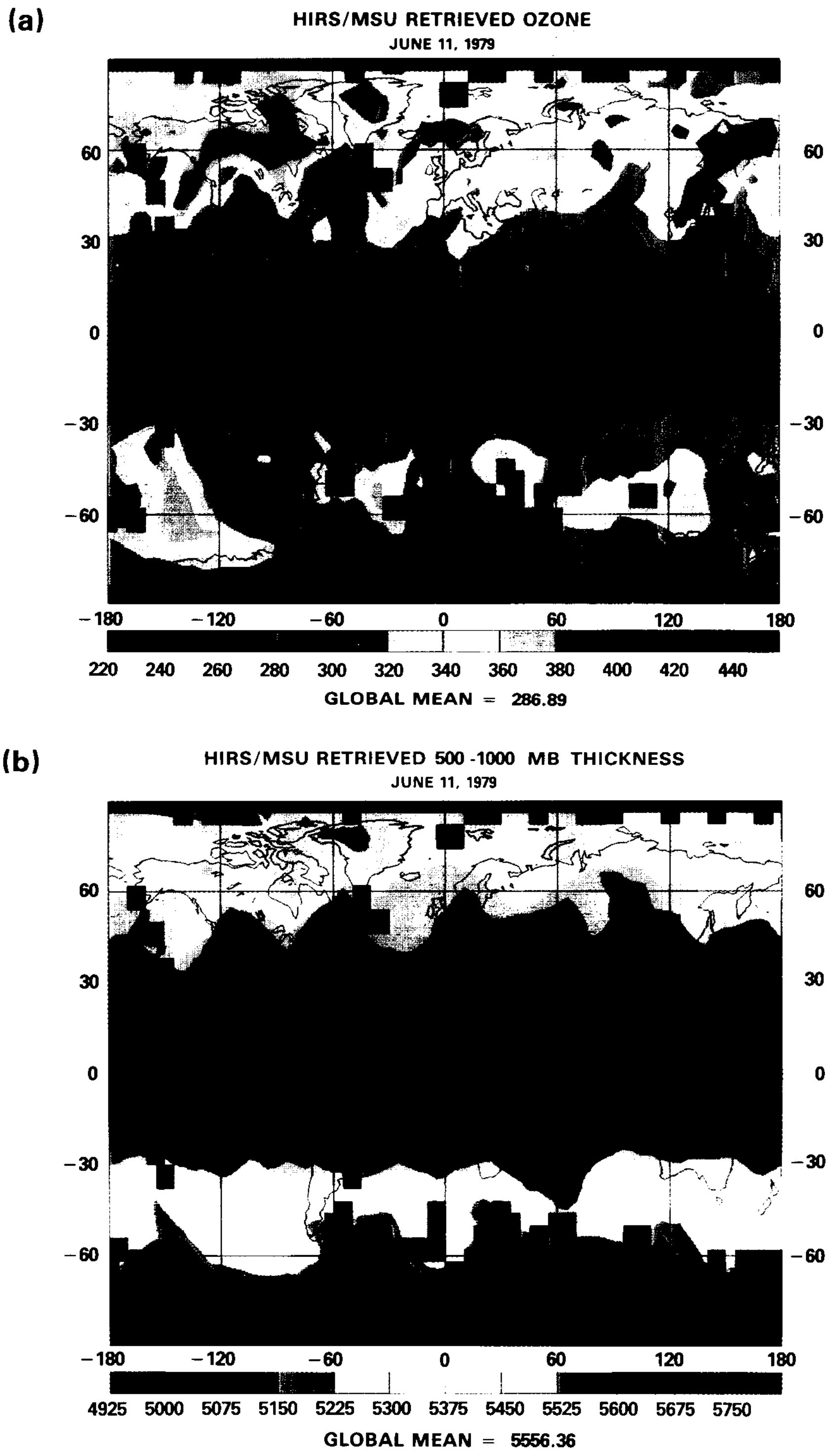

Figure 5 (a) Total O_3 (Dobson units) retrieved from TIROS-N HIRS2/MSU soundings for June 11, 1979 on a 4° x 5° grid. Black indicates no soundings in the grid box. (b) 500 - 1000 mb thickness (meters) retrieved from TIROS-N HIRS2/ MSU soundings on June 11, 1979.

ORIGINAL PAGE

ORIGINAL PAGE
COLOR PHOTOGRAPH

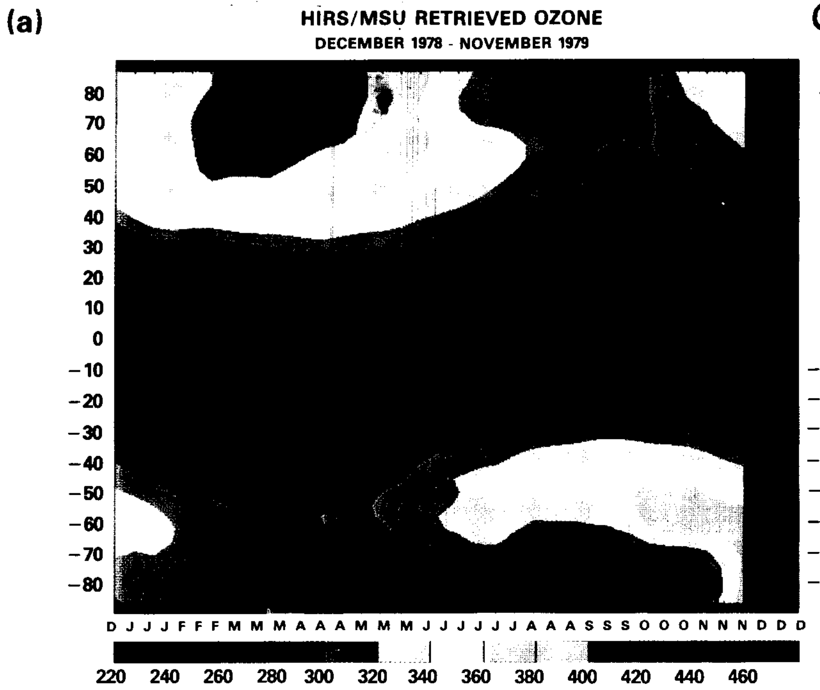

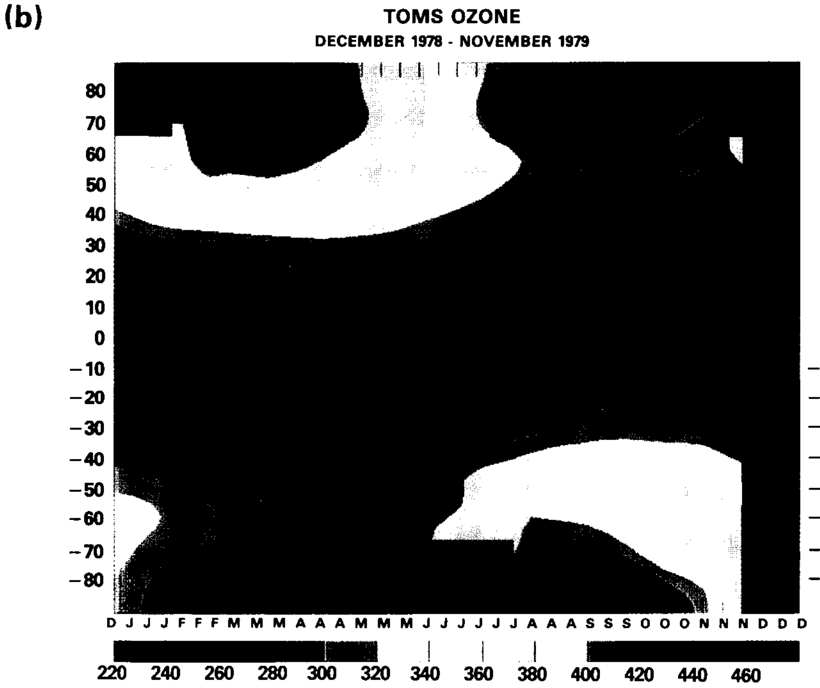

Figure 6 (a) Zonal mean values of total O_3 (Dobson units) retrieved from TIROS-N HIRS2/MSU soundings for each 1/3 of a month for the period Dec. 21-31, 1978 to November 1-10, 1979. (b) As in (a) but for O_3 derived from TOMS soundings.

The field of total O_3 southward of 40°S retrieved from analysis of HIRS2/MSU data from NOAA 10 with a 7:30 AM, PM local time crossing is shown in Figure 7a for the 24 hour period August 18, 9Z to August 19 9Z, 1987. Gray areas indicate data gaps. The TOMS field (on NIMBUS 7 with a local noon orbit) is shown in Figure 7b. TOMS produces no soundings in the vicinity of the South Pole because of nighttime conditions, even at noon. The general agreement between the fields is quite good. Some differences due to sampling time are apparent, as evidenced by slight differences in the locations of the highs and lows. It is interesting to note a relatively deep low in the HIRS2/MSU field at about 78°S, 140°W which is in an area inaccessible by TOMS.

The total O_3 is affected to first order by two quantities, the distribution of the mixing ratio of O_3 in the stratosphere, which is O_3 rich, and the depth of the stratosphere, which is given by the tropopause pressure. Figure 8a shows the tropopause pressure determined from the HIRS2/MSU soundings of temperature. It is apparent that high values of tropopause pressure, which correspond to a deep stratosphere, do indeed correspond to high total O_3 values. This indicates that to first order, the total O_3 field appears to be more of a measure of tropospheric circulation rather than stratospheric photochemical processes, at least on this particular day. Figure 8b shows another field determined from analysis of HIRS2/MSU data, the cloud top pressure, which is also related to tropospheric circulation and is likewise highly correlated with total O_3. Fields such as these complement the aircraft measurements of concentration of species involved in the O_3 photochemical cycle in helping to understand the relative roles of atmospheric dynamics and photochemistry in affecting the distribution of total O_3.

Computation of Outgoing Longwave Radiation

One of the most exciting recent developments involving our satellite retrieval research is the computation of outgoing longwave radiation (OLR) from the GLA retrieval products. Outgoing longwave radiation is primarily a function of ground-temperature and emissivity, the atmospheric temperature-humidity-ozone profile, and cloud top pressure and effective cloud fraction (the product of the fractional cloud cover and cloud emissivity at 11 μm). These parameters are all determined in the course of producing the retrievals (the surface emissivity is pre-determined for land and ocean, but ground temperature is determined consistent with the assumed emissivity). For the computation of OLR, the sounding products are used as input to the radiative transfer program of the GLA fourth order GCM, which was parameterized by Wu and Kaplan and documented by Krishnamurti (1982).

The input parameters to the radiation code are the soundings of the atmospheric temperature-humidity profiles, sea/land surface temperature, and cloud top pressure and effective cloud cover, as derived from analysis of the HIRS2/MSU data. OLR has been computed for every month of the FGGE year. For purposes of this discussion, the monthly mean values of July 1979 shown in Figure 9a have been chosen. In the tropics, where thermal variations are relatively low, the parameters which have the largest effect on the OLR are the cloud top pressure and effective cloud fraction. High effective cloud fraction with low cloud top pressure (high altitude) is found over areas associated with the Intertropical Convergence Zone (ITCZ) and the monsoon. These same features show up as low values in the OLR field. High values of OLR are

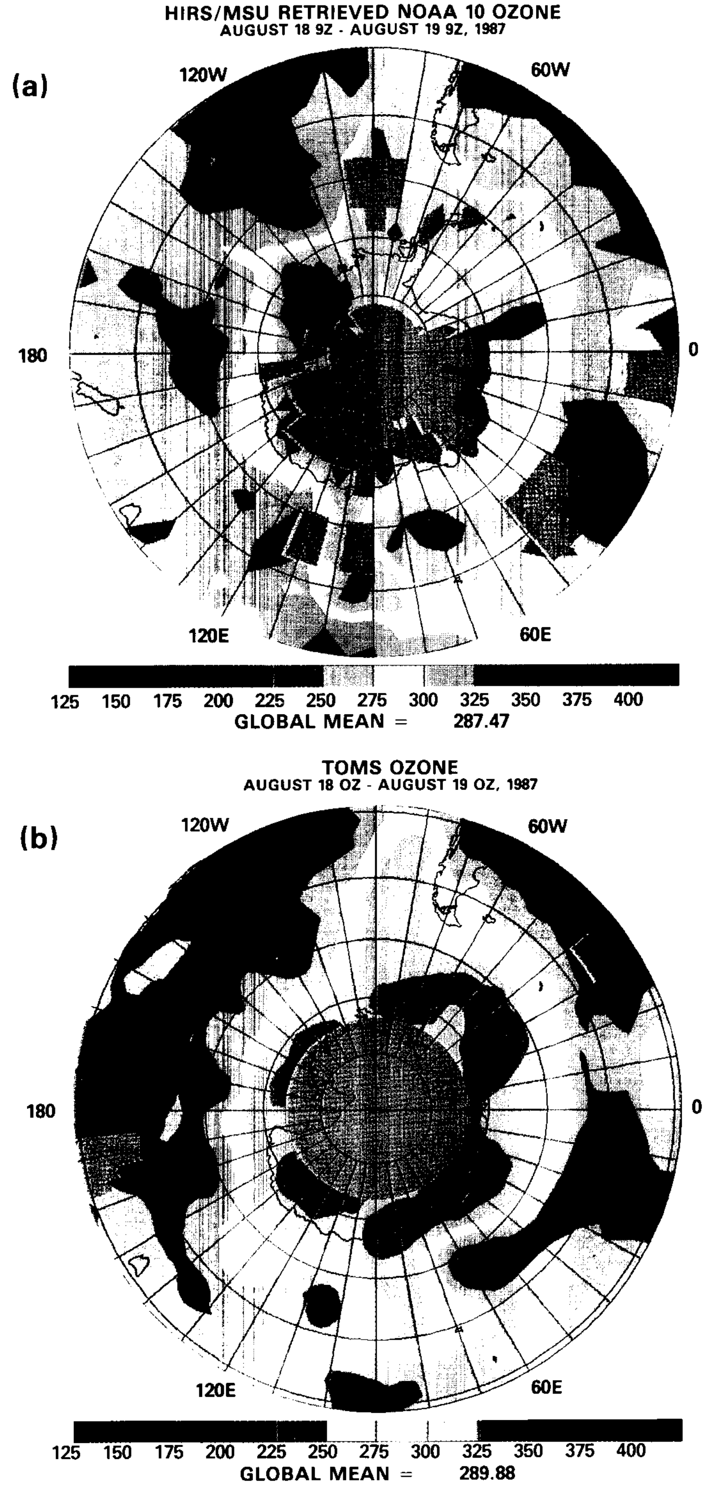

Figure 7 (a) Total ozone (Dobson units) derived from NOAA 10 HIRS2/MSU soundings August 18, 9Z, 1987 - August 19, 9Z, 1987. Grey indicates no sounding in a grid box. (b) As in (a) but derived from TOMS data for a 24 hour period starting 9 hours earlier.

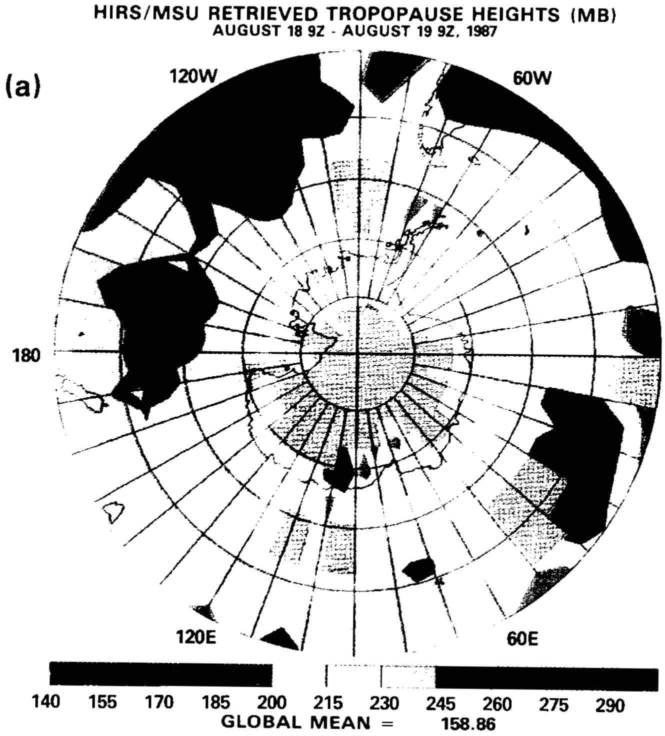

HIRS/MSU RETRIEVED TROPOPAUSE HEIGHTS (MB)
AUGUST 18 9Z - AUGUST 19 9Z, 1987

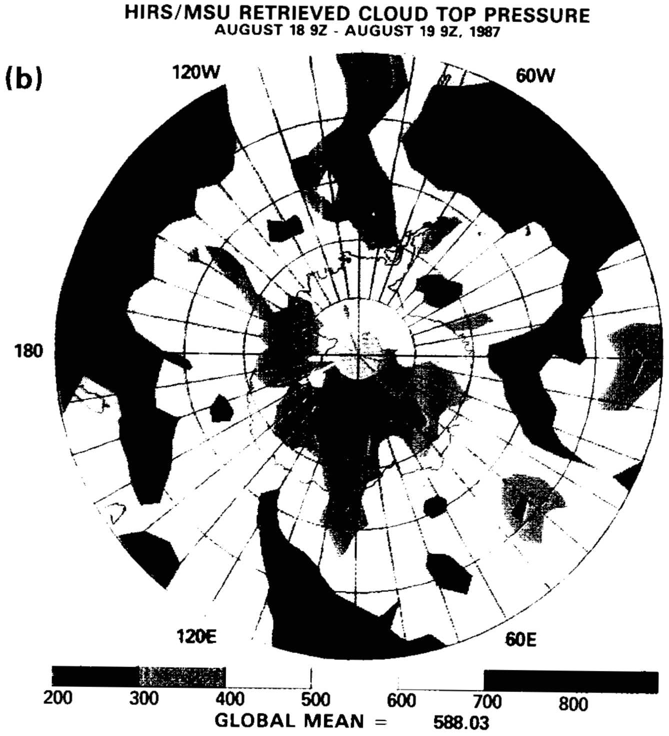

HIRS/MSU RETRIEVED CLOUD TOP PRESSURE
AUGUST 18 9Z - AUGUST 19 9Z, 1987

Figure 8 (a) Tropopause pressure (mb) derived from NOAA 10 HIRS2/MSU soundings August 18, 9Z, 1987 - August 19, 9Z, 1987. Grey indicates no sounding in a grid box. (b) As in (a) but for cloud top pressure (mb).

ORIGINAL PAGE
COLOR PHOTOGRAPH

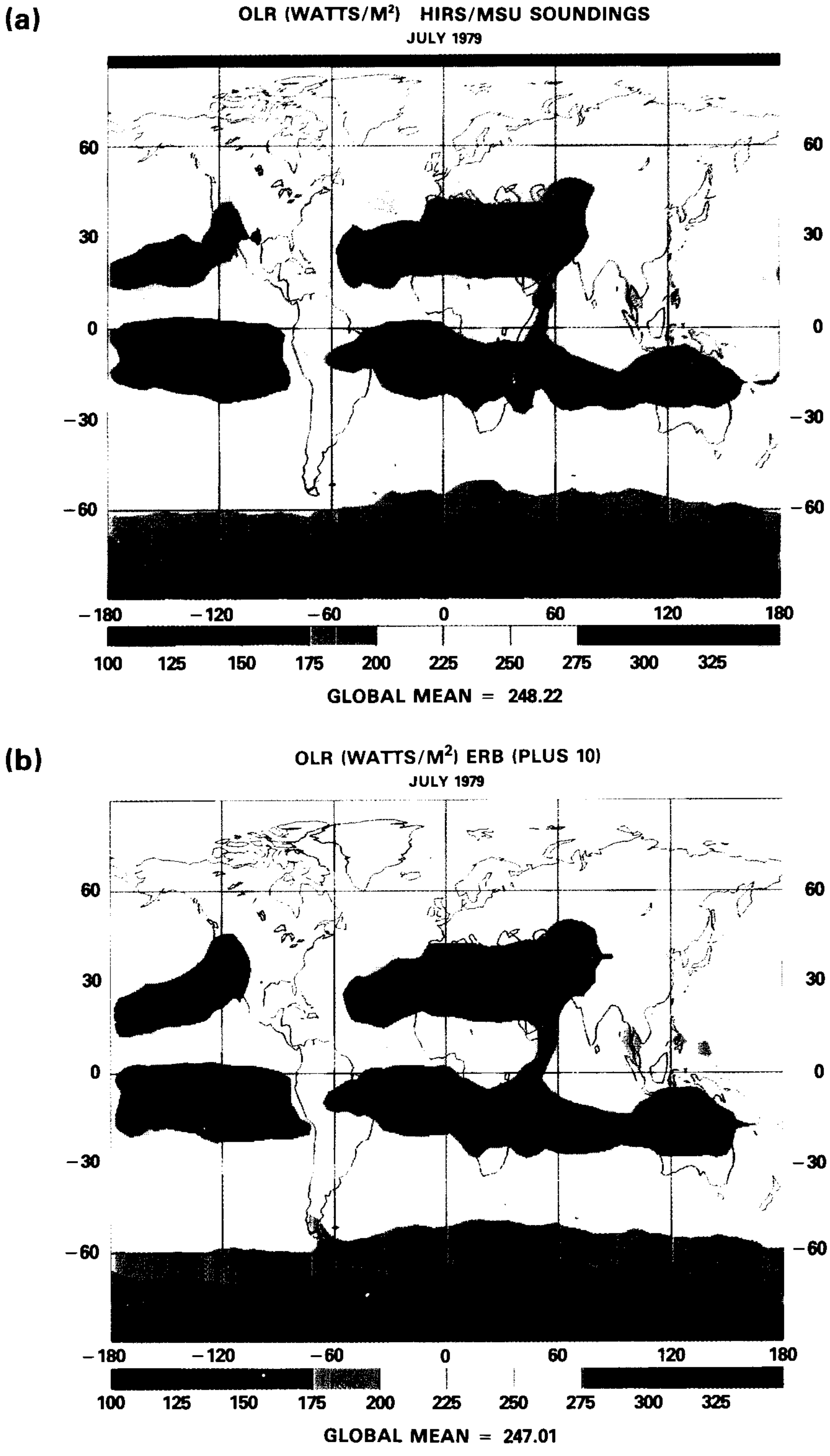

Figure 9 (a) Monthly mean values of OLR (W m^{-2}) derived from TIROS-N HIRS2/MSU soundings for July 1979. (b) As in (a) but using ERB data. 10 W m^{-2} have been added to all reported ERB values and the global mean.

generally found immediately to the north and south of the convective areas in regions of subsidence, which are either relatively clear or have stratus clouds at low altitudes. In the extra-tropics, OLR generally decreases with decreasing temperature and is more correlated with temperature.

The OLR computed using products retrieved from the HIRS2/MSU, which will be referred to as HIRS OLR, has been compared to two other determinations of OLR, the OLR derived for the narrow band (~ 11 μm) measurements of Advanced Very High Resolution Radiometer (AVHRR), which will be referred to as AVHRR OLR, and to the OLR derived from the Earth Radiation Budget (ERB) broad-band (5-50 μm) narrow field of view observations (NFOV) of NIMBUS 7, which will be referred to as ERB OLR.

In general, there is excellent agreement between the computed HIRS OLR field shown in Figure 9a and that derived from the ERB observations shown in Figure 9b, both in pattern as well as in magnitude. High OLR (~ 275 Wm^{-2}) is found in areas associated with oceanic trade wind systems, low level stratocumulus, and deserts and semi-arid areas, and low OLR (<225 Wm^{-2}) is found in areas associated with major convective cloud systems such as the ITCZ and monsoon, or regions having low temperatures such as the polar regions. The AVHRR OLR field (not shown) also shows good agreement with the other two. There are some systematic differences between all three fields, however. The monthly mean difference between HIRS OLR and AVHRR OLR for July 1979 is shown in Figure 10a. It is apparent that HIRS values are systematically greater in areas of high OLR and lower in areas of low OLR. This implies that the AVHRR somewhat damps the results. Figure 10b shows the monthly mean difference of HIRS and ERB OLR. The values are much smaller than in Figure 10a, but now there appears to be a tendency of HIRS to slightly underestimate the extreme values compared to ERB.

Table 2

Statistics of Global OLR Fields (Wm^{-2}) July 1979

Field	Mean	Stand. Dev.
HIRS	248.3	46.3
ERB	237.0	48.5
AVHRR	249.4	43.4
HIRS-ERB	11.3	6.2
HIRS-AVHRR	-1.1	7.5
AVHRR-ERB	12.4	10.0

Statistical comparisons of OLR determined from the three sources are shown in Table 2 for July 1979. Values given are means and standard deviations of the global OLR for each system as well as corresponding values for the difference fields. As noted in Table 2, the July 1979 global mean values of OLR computed from HIRS soundings and determined from AVHRR observations differ by 1.1 Wm^{-2}, while HIRS differs in the mean from ERB by 11.3 Wm^{-2}

ORIGINAL PAGE
COLOR PHOTOGRAPH

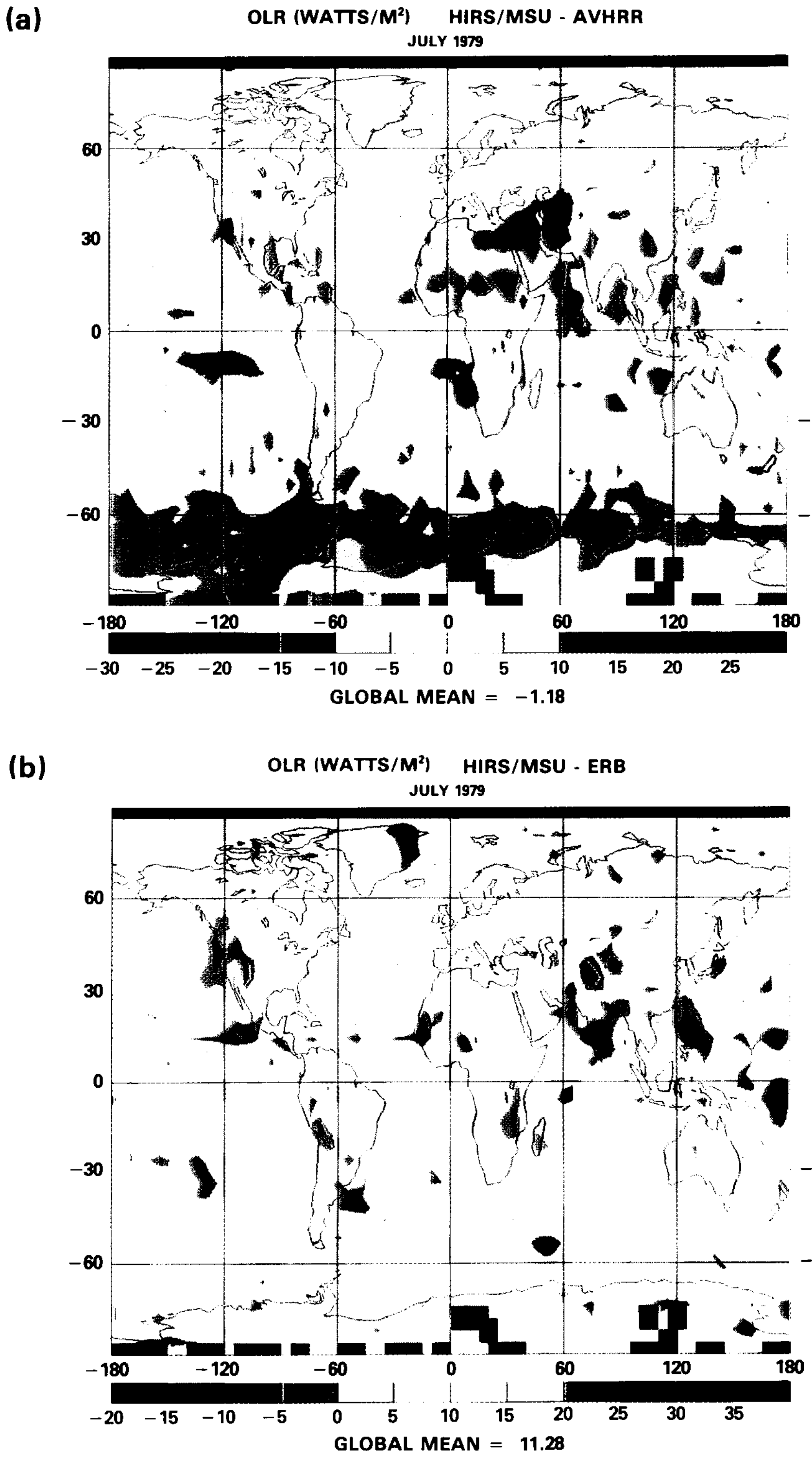

Figure 10 (a) The difference (W m^{-2}) of OLR for July 1979 derived from HIRS2/ MSU soundings and that derived from AVHRR. Red means HIRS2/MSU values are larger than AVHRR. (b) As in (a) but substituting ERB OLR values for AVHRR values. The color code is shifted 10 W m^{-2} to account for relative bias in ERB values.

and AVHRR from ERB by 12.4 Wm^{-2}. The HIRS-ERB difference shows a global standard deviation of 6.2 Wm^{-2}, HIRS-AVHRR is 7.5 Wm^{-2}, and AVHRR-ERB is 10.0 Wm^{-2}, which are all computed on the 4° x 5° latitude-longitude grid. While all the differences are small, the patterns of the differences are systematic and indicate that the differences are related to the values of OLR themselves, with ERB showing the biggest dynamic range, HIRS a close second, and AVHRR being the most damped. This is consistent with the values of the standard deviations of the measurement themselves with ERB being largest and AVHRR smallest. This damping effect is also observed in the zonal mean of OLR for July 1979 determined from each instrument (not shown). Values for ERB have been increased by 10 Wm^{-2} (as was done in Figure 10b), which was the bias for the entire FGGE year compared to HIRS OLR, to provide an easier comparison of the relative zonal structure of the three measures of OLR.

The relative monthly biases of the OLR fields between all three products varied less than 1.5 Wm^{-2} throughout the year. L. Kyle (private communication) has indicated that a 3 Wm^{-2} bias in the calibration of ERB has been found and this value is being added to the ERB OLR values. This reduces the bias between HIRS and ERB from 10 to ~ 7 Wm^{-2}.

The reasonable agreement between the computed OLR and OLR derived from measurements indicates that the GLA physical retrieval system derives relatively accurate soundings, and the radiative transfer code properly takes into account the cloud radiative properties, surface conditions, humidity, and temperature variations. This gives us the ability to relate variations of OLR in space and time to variations in other geophysical parameters. In particular, we have computed OLR_{CLR}, the OLR which would have been observed if no clouds were present, with the geophysical parameters otherwise being identical. This allows for the computation of ΔOLR ,the difference between OLR_{CLR} and OLR, which is the longwave radiative cloud forcing, an important parameter that cannot be measured directly.

The monthly mean field of ΔOLR for July 1979 is shown in Figure 11a. Features associated with high clouds in the tropics are considerably more pronounced in the ΔOLR field than in the OLR field shown in Figure 9a. Part of this enhancement results from the ability to use a finer scale (ΔOLR varies by the order of 60 Wm^{-2} over the globe while OLR varies by about 250 Wm^{-2}). In addition, most convection occurs over the warmest surface areas. Therefore, the effect of partial high clouds, which lowers total OLR, is being damped by the effect of underlying warmer surface temperature in clear parts of the scene, which increases the OLR. Even more significantly, sharp cloud features now appear in the extra-tropics, which were masked in the OLR field itself because of large meridional thermal gradients. Note, for example, the appearance in Figure 11a of large cloud effects in the vicinity 50°N-60°N, and even more so, at 50°S-60°S, a region associated with winter oceanic storm tracks. Figure 11b shows the monthly mean values of ΔOLR for January 1979. Here again, major convective areas such as the Intertropical Convergence Zone, South Pacific Convergence Zone, and South Atlantic Convergence Zone are depicted quite prominently. In addition, the winter storm tracks in the North Atlantic and North Pacific areas, which are not apparent in the OLR field for January 1979, are quite prominent in ΔOLR .

Zonal mean values of ΔOLR are shown in Figure 12a for July 1979. ΔOLR

ORIGINAL PAGE
COLOR PHOTOGRAPH

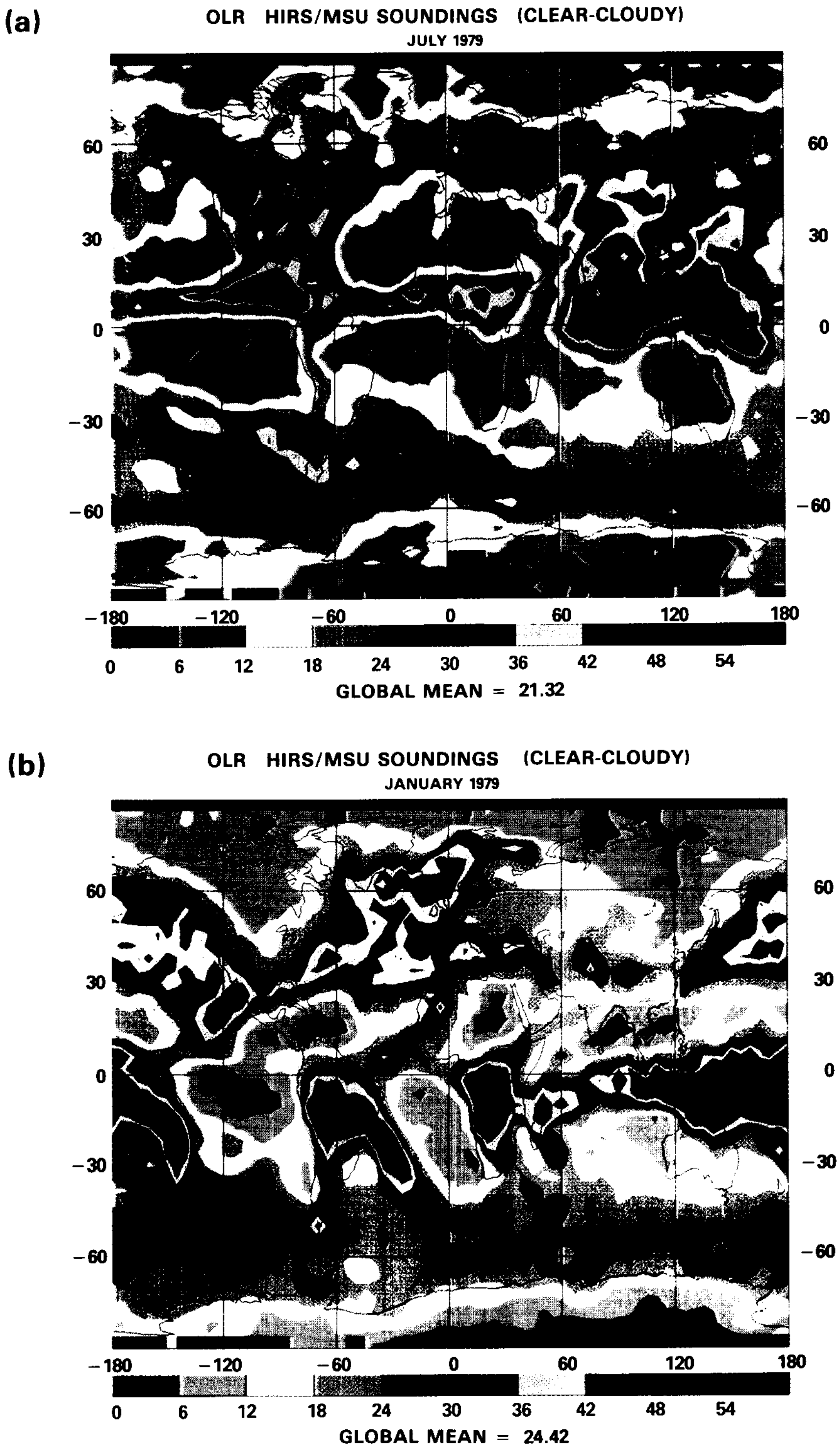

Figure 11 (a) Monthly mean values of ΔOLR (W m^{-2}) derived from TIROS-N HIRS2/MSU soundings for July 1979. Δ OLR is representative of the longwave cloud radiative forcing and is also indicative of precipitation. (b) As in (a) but for January 1979.

has a much sharper zonal structure around the ITCZ than does OLR, as shown in Figure 9a. In addition, secondary maxima, indicative of precipitation, occur in mid-latitudes which are not apparent in Figure 9a. Figure 12b shows the zonal mean of ΔOLR for the year of 1979. Overall features are similar to those in Figure 12a, but a local maximum is found at 8°S, resulting from increased precipitation in the Southern Hemisphere tropics in the Northern Hemisphere winter. The Northern Hemisphere extratropical maximum has also sharpened up and moved to about 36°N, which is indicative of more mid-latitude-precipitation in the Northern Hemisphere winter. The reverse effect has also occurred in the Southern Hemisphere extra-tropics.

Precipitation Estimates Derived From HIRS2/MSU Soundings

The cloud radiative forcing field, ΔOLR , is a measure of the extent to which the basic radiative state of the atmosphere has been disturbed. Figures 11a and 11b suggest that ΔOLR is closely related to precipitation with large values indicative of large amounts of thick clouds, and associated with more precipitation especially over oceans. Precipitation is inhibited over land, however, when the surface temperature is high during the day because heating from the ground raises the cloud base. An indicator of ground heating and possibly cloud base height can be constructed by using the difference of computed clear daytime OLR and clear nightime OLR, or ΔCLR. Large values of ΔCLR would tend to reduce precipitation. Large values of ΔCLR, indicative of large diurnal variation in surface temperature, also are a measure of antecedent precipitation because dry soil heats up much more rapidly than moist soil. Relating monthly mean fields of ΔOLR and ΔCLR to monthly precipitation derived from rain gauge measurements over land by Walker and Mintz (1988) for each month of the FGGE year indicates that a reasonable regression relationship exists between precipitation and ΔOLR and ΔCLR which is primarily linear with small quadratic terms in each variable. One set of coefficients was found to be applicable for the whole globe and the whole year.

Figure 13a shows the July 1979 monthly mean field of precipitation derived using this relationship on the fields of ΔOLR and ΔCLR computed from the monthly mean HIRS2/MSU sounding products. As expected, Figure 13a is qualitatively similar to ΔOLR shown in Figure 11a especially over oceans. The monthly mean field of precipitation obtained by Walker and Mintz from rain gauge measurements (and degraded to a 4° x 5° resolution) is shown in Figure 13b for comparison. The agreement of these two fields is quite reasonable when one bears in mind the many sources of error, especially sampling errors such as the 3AM, 3PM local time sampling of HIRS2 data, and the limited area sampling of rain gauge measurements.

The wet areas over eastern North America, north of the Mediterranean, the ITCZ, Eastern Asia and the southern tip of South America, and the dry areas over western North America, South America, North and South Africa, Saudi Arabia, and Australia are all reasonably derived. The relatively dry area over Central China shown in Fig. 13a is a known dry climatological feature of China for July [Lau et al. (1986)] based on 11 years of rain gauge data, which includes data provided by Academia Sinica of China. A dry zone over the Yangtze River basin is clearly shown in their compilation.

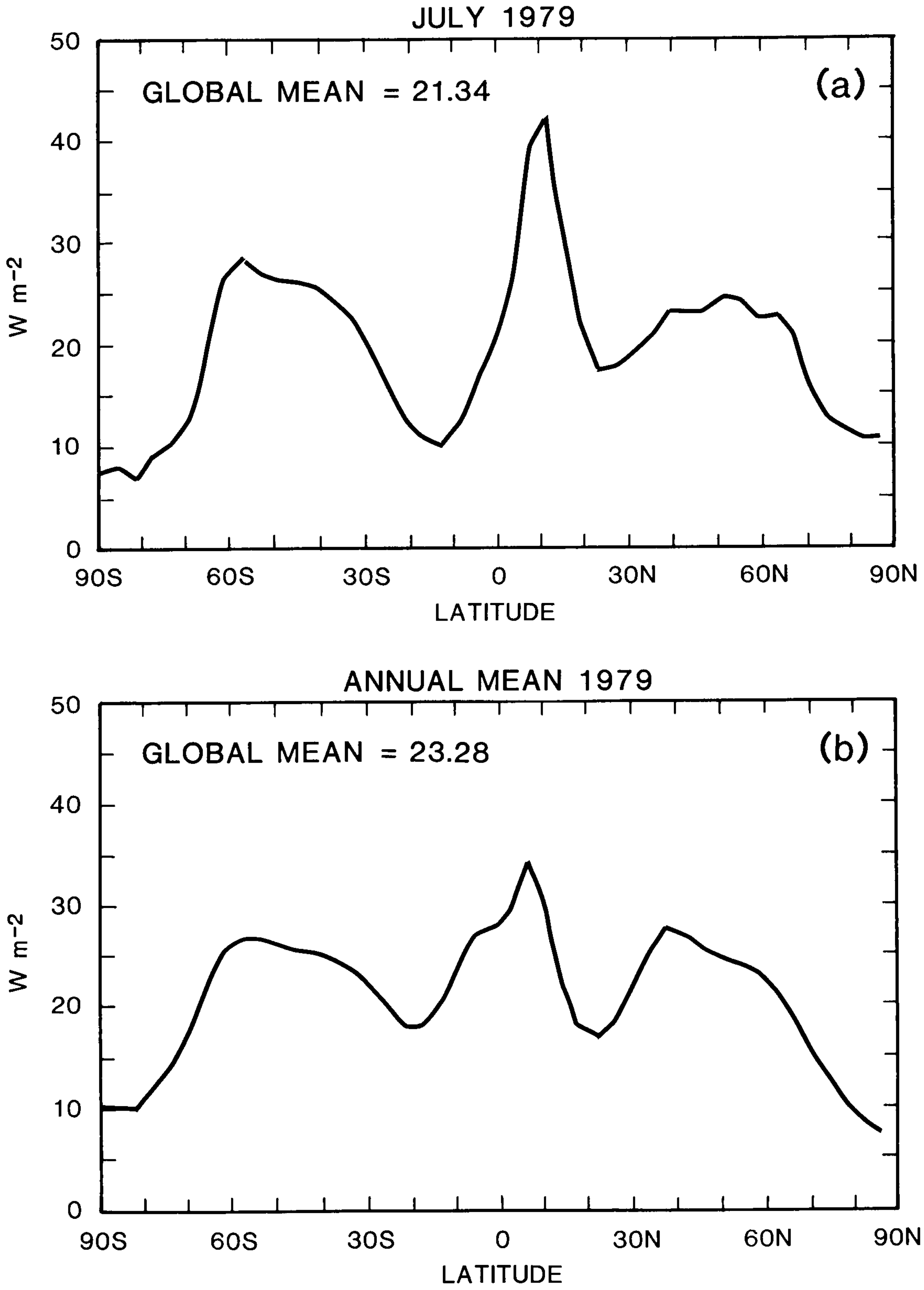

Figure 12 Zonal mean values of OLR clear-OLR cloudy (W m^{-2}) derived from HIRS2/MSU soundings for (a) July 1979 and (b) all of 1979. Global mean values are shown.

ORIGINAL PAGE
COLOR PHOTOGRAPH

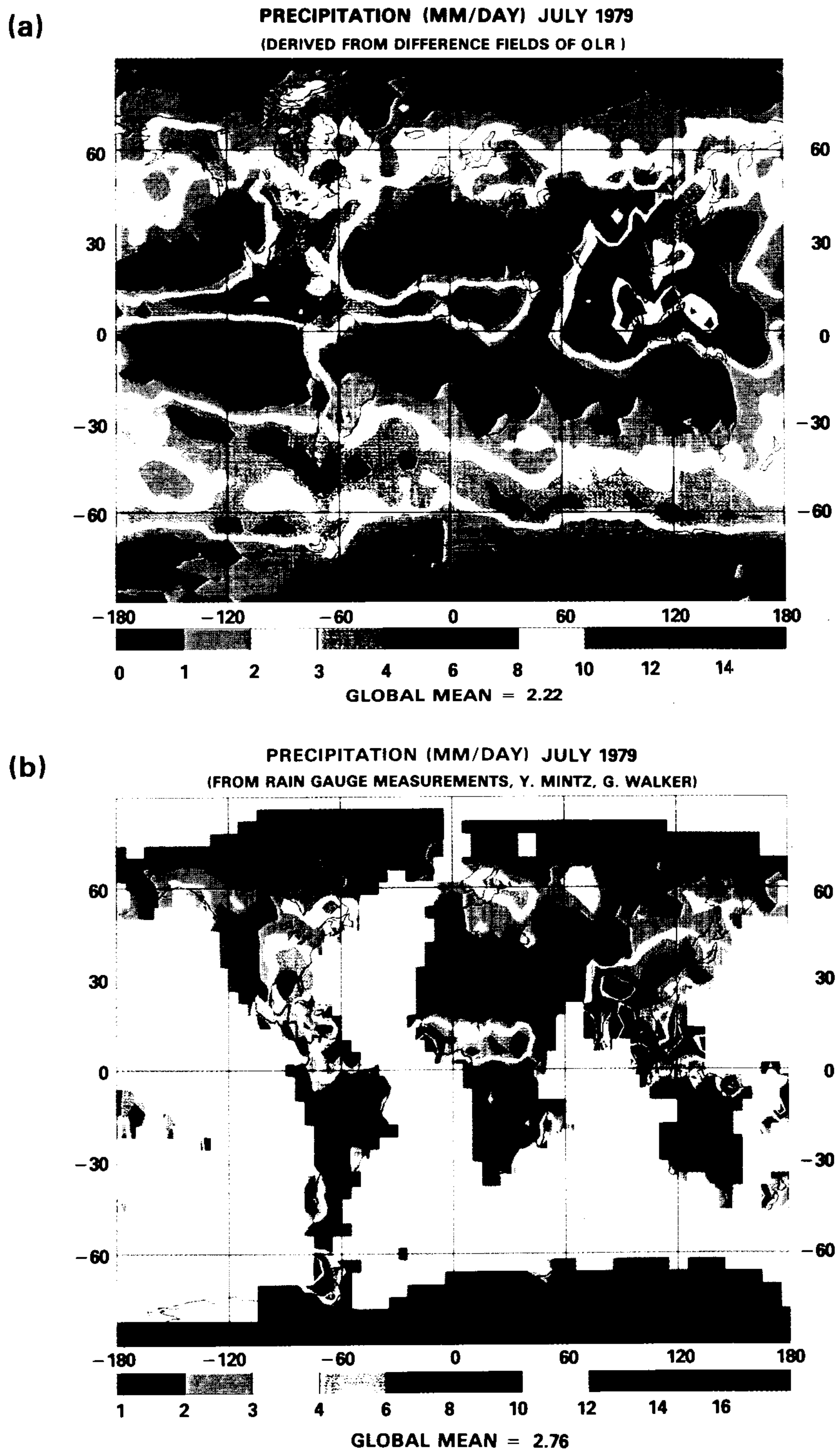

Figure 13 (a) Monthly mean field of precipitation (mm/day) for July 1979 derived from HIRS2/MSU soundings. (b) Monthly mean field of precipitation (mm/day) for July 1979 derived by Walker and Mintz from FGGE rain gauge measurements (degraded to 4°x5° resolution).

Over the oceans there are no ground truth measurements available. Nevertheless, the patterns shown are in good agreement with expectations based on atmospheric circulation. For example, in July the major ITCZ is in the Northern Hemisphere. The equatorial rain belt associated with the ITCZ, the monsoon rain band, and rain band associated with the winter storm tracks and polar front look reasonable. The oceanic dry zones associated with trade wind systems in both hemispheres are also reasonable.

Results Depicting The 1979 FGGE Year

Annual mean, monthly mean, and 10 day mean fields of all retrieved quantities have been produced throughout the 1979 FGGE year. As an example of the results, this section will show select fields on an annual basis, both as global annual mean fields and zonal mean fields for each 10 days through the year.

Annual mean fields of radiatively effective cloud fraction (fractional cloud cover multiplied by the cloud emissivity at 11μm and cloud top pressure are shown in Figures 14a and 14b. Even though seasonal variations have been averaged out, very clear annual mean circulation patterns showing areas of convection (red-high clouds) and subsidence (blue-low clouds) exist. It is interesting to note the preferred northern hemisphere location of the ITCZ, which is characterized by moderate amounts of high clouds in the region 0° to 160°W. From 60°E to 160°W the annual mean ITCZ is centered roughly on the equator.

The annual mean sea-land surface skin temperature (3AM, 3PM local time, average) and total clear air precipitable water are shown in Figures 15a and 15b. Comparison of Figure 15a with Figure 14b shows that areas of high clouds in the tropics over land correspond to areas of low surface temperature. This result is a consequence of the low diurnal variation of ground temperature in areas of large amounts of precipitation. These same areas also exhibit maxima in total precipitable water. Both findings are consistent with those of a regional study which was conducted over Africa.

The relationship of surface temperature with cloud height is reversed in the tropical oceans in which areas of high clouds correspond to warm oceanic areas, which also contain large amounts of precipitable water, while areas of low clouds correspond to cold oceanic areas with a relatively dry atmosphere. This is consistent with the concept of the atmospheric circulation being forced by the ocean. The situation is more complex, however, because ocean temperatures also respond to atmospheric winds.

The annual mean sea surface temperatures shown in Figure 15a are in fact very close to expected climatological values (Reynolds, 1982). An annual mean sea-surface temperature anomaly for 1979 has been produced by averaging daily anomaly fields obtained by subtracting Reynolds' monthly mean sea-surface temperature climatological values, interpolated to the satellite location and time from the satellite derived sea-surface temperatures. These anomaly fields have also been produced every ten days. The patterns evolve very slowly throughout the year. It was found that 1979 was not particularly anomalous, but small systematic anomaly patterns do exist. The most striking feature is an 0.5° - 1.0°C cold anomaly in the band 10°N - 20°N throughout the

ORIGINAL PAGE
COLOR PHOTOGRAPH

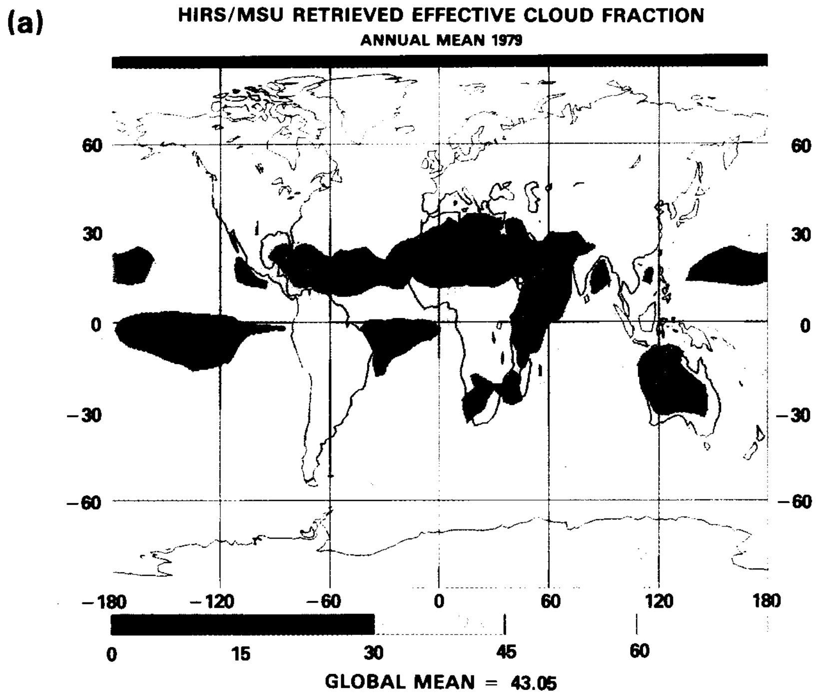
(a) HIRS/MSU RETRIEVED EFFECTIVE CLOUD FRACTION

ANNUAL MEAN 1979

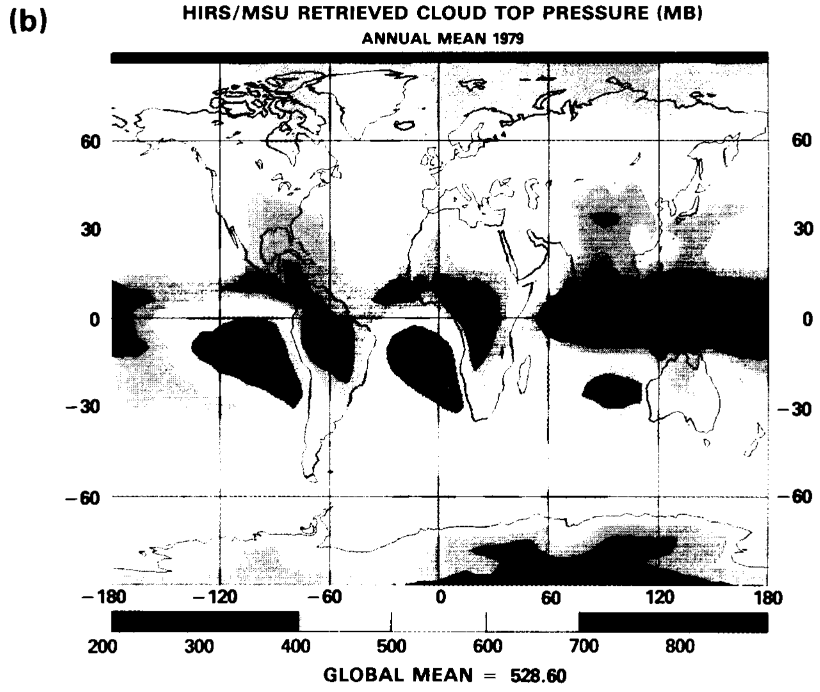
(b) HIRS/MSU RETRIEVED CLOUD TOP PRESSURE (MB)

ANNUAL MEAN 1979

Figure 14 (a) Annual mean retrieved effective cloud fraction (%) for the period December 1978 - November 1979. The global annual mean effective cloud fraction is 43%. (b) Same as (a) but for cloud top pressure (mb). The global annual mean cloud top pressure is 528.6 mb.

ORIGINAL PAGE
COLOR PHOTOGRAPH

(a)

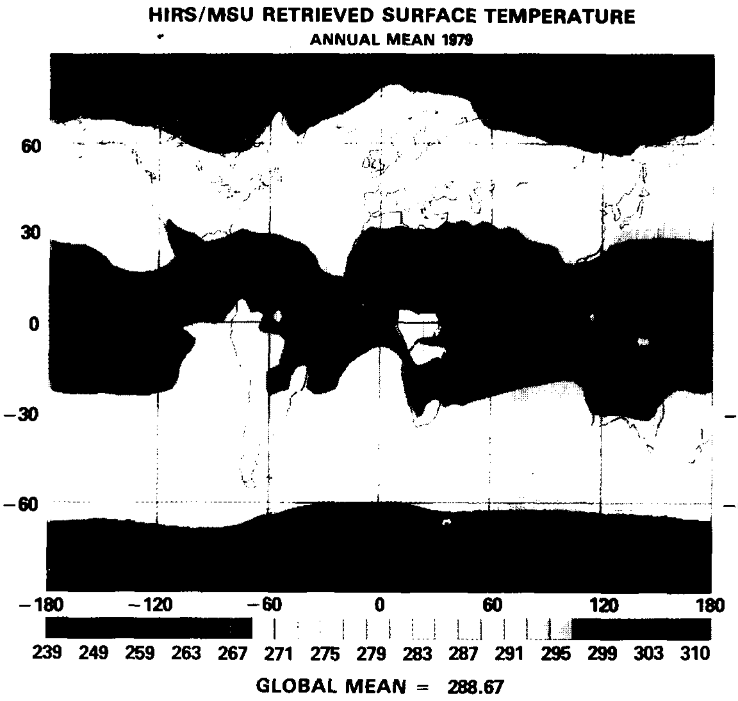

(b)

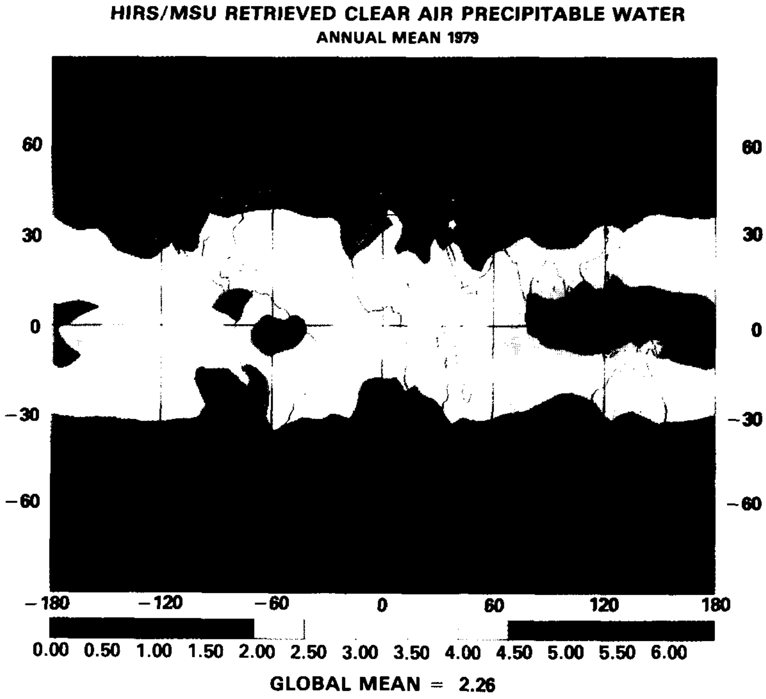

Figure 15 (a) Annual mean retrieved average of 3PM and 3AM surface skin temperature (K) for the period December 1978 - November 1979. The global annual mean is 288.7° K. (b) As in (a) but for clear air precipitable water (cm). The global annual mean is 2.26 cm.

Pacific Ocean. There was also a 0.5°C warm anomaly north of 45°N in the eastern Pacific and Atlantic Oceans.

In addition to annual mean values, it is of interest to look at temporal changes of a number of geophysical quantities. Figures 16a and 16b show the zonal mean cloud fraction and cloud top pressure averaged over every third of a month (roughly 10 day periods) for the period December 21, 1978 to November 30, 1979. Areas of large amounts of cloudiness are shown in red in Figure 16a and high clouds (low cloud top pressures) are shown in red in Figure 16b. The temporal motion of the ITCZ, which is characterized by moderate amounts of high clouds in the vicinity of the equator, is clearly observed in Figures 16a and 16b. This region is centered about 8°S latitude in the period December through early March, and is centered about 8°N in June through October. The region of the ITCZ is also narrower in the summer and it is interesting to note that it only begins its return to the southern hemisphere in late November. The regions immediately north (or south) of the ITCZ are characterized by the existence of small amounts of very low clouds in the winter season, but have more mid-level clouds in the summer.

Figures 17a and 17b show zonal mean values of surface skin temperature and clear-air precipitable water for the same period. Both fields have patterns which are very similar to each other with surface skin temperature and humidity closely following the seasonal cycle. The amplitude of the oscillation is very small in the southern hemisphere, which is mostly ocean, and increases toward the north with the largest amplitudes northward of 40°N latitude. However, this seasonal dependence at high latitudes was almost totally absent in the cloud parameters.

Figure 18a shows the zonal mean values of OLR. In the tropics, the patterns of OLR clearly follow those of the cloud parameters, and the motion of the ITCZ and the surrounding area of subsidence is clearly observed. In the extra-tropics, OLR patterns strongly resemble those of ground temperature. This occurs because the colder ground leads to lower values of OLR in clear areas, and also produces colder air and colder clouds giving lower values of OLR in cloudy areas as well. In addition, the zonal mean cloud parameters show very little temporal structure in the extra-tropics. The 10 day zonal mean values of OLR_{CLR}-OLR are shown in Figure 18b. The thermal effects evident in Figure 18a are no longer present. Moreover, the cloud effects in the tropics are much better defined in Figure 18b than in 18a, and cloud forcing, which is indicative of precipitation, now shows large values in mid-latitudes, especially in the northern hemisphere winter when storms are prevalent over the oceans.

III. NUMERICAL WEATHER PREDICTION (J. Pfaendtner)

Fourth-Order Model Development (H. M. Helfand, Y. Sud)

The horizontal resolution of the GLA Fourth-Order Weather Forecast Model has been doubled by changing from a 4° latitude by 5° longitude to a 2° latitude by 2.5° longitude grid. As can be seen in Figure 19, this has added about 24 hours of useful predictive skill to forecasts of sea-level pressure (SLP) and 6 to 12 hours of useful skill to 500 mb geopotential height field

ORIGINAL PAGE
COLOR PHOTOGRAPH

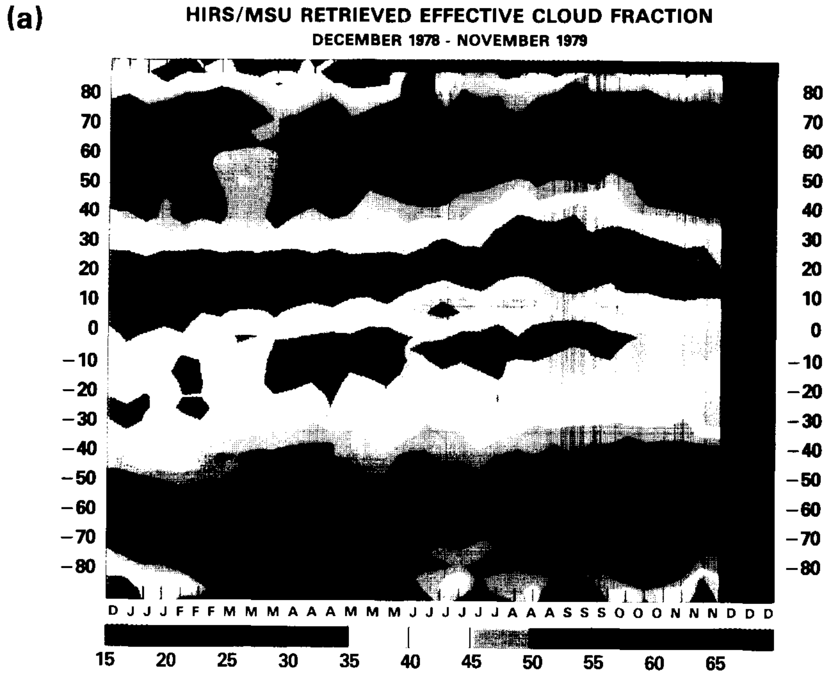

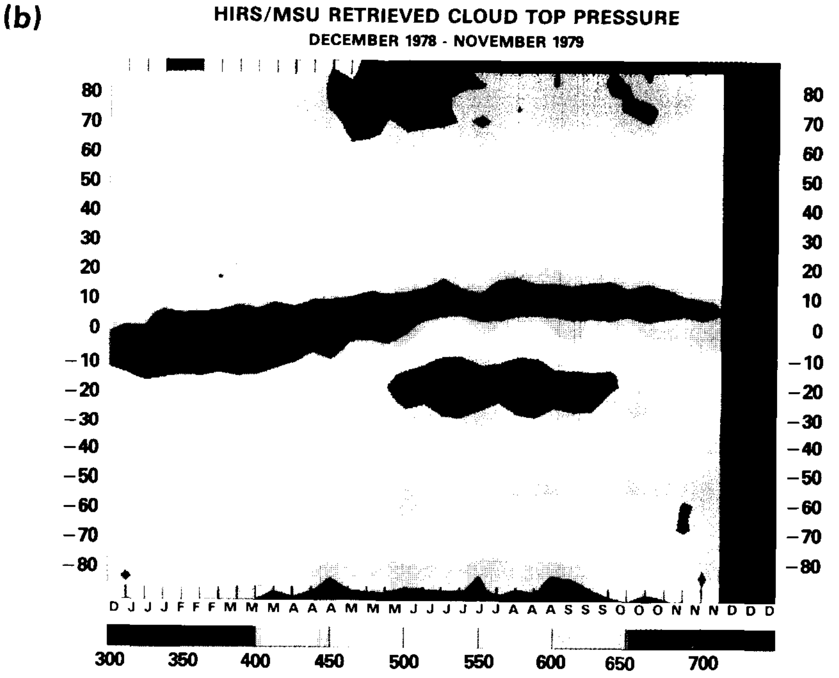

Figure 16 (a) Zonal mean effective cloud fraction (%) every 1/3 of a month for the period December 21-31, 1978 to November 21-30, 1979. (b) As in (a) but for cloud top pressure (mb).

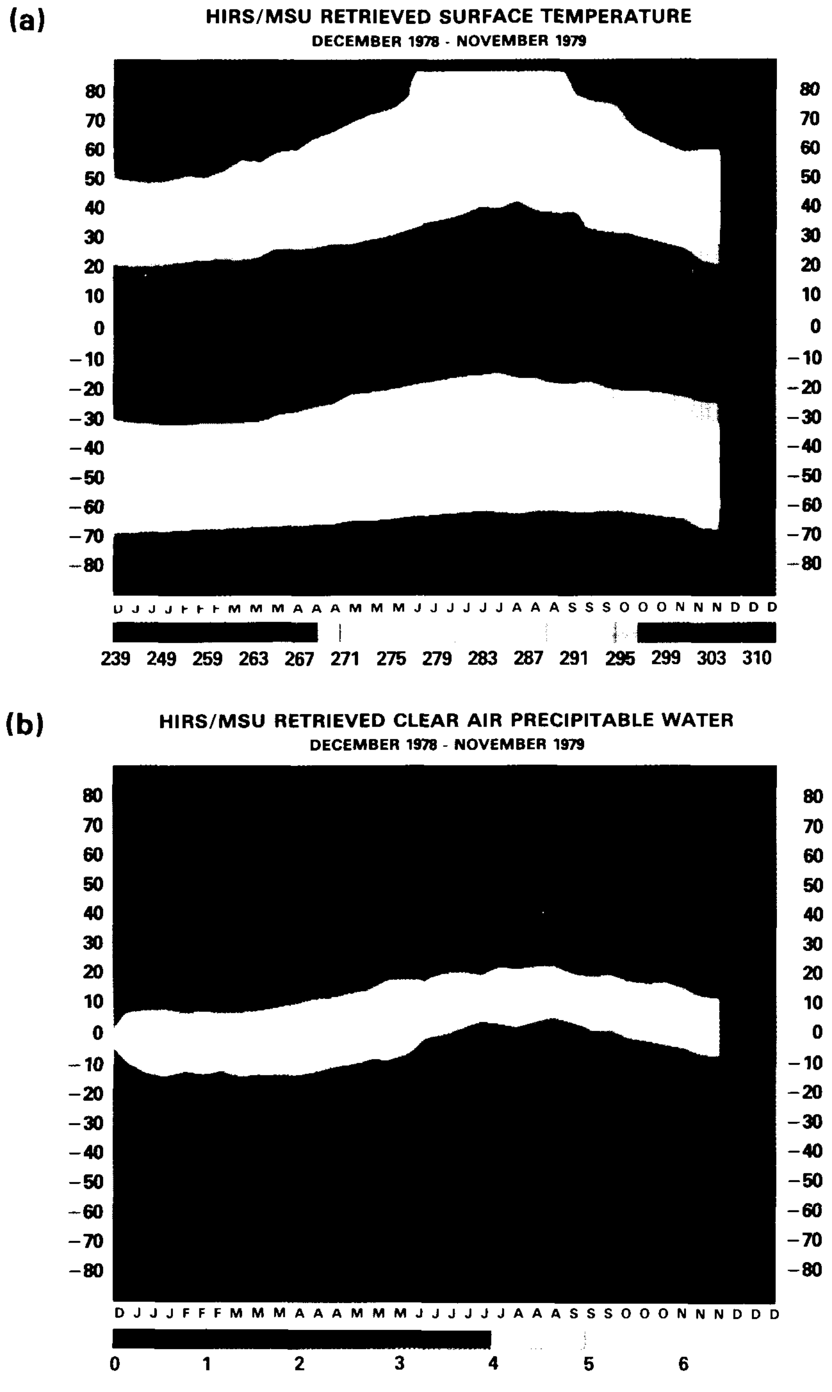

Figure 17 (a) Zonal mean average of 3PM and 3AM surface skin temperature (K) every 1/3 of a month for the period December 21-31, 1978 to November 21-30, 1979. (b) As in (a) but for clear air precipitable water (cm).

ORIGINAL PAGE
COLOR PHOTOGRAPH

ORIGINAL PAGE
COLOR PHOTOGRAPH

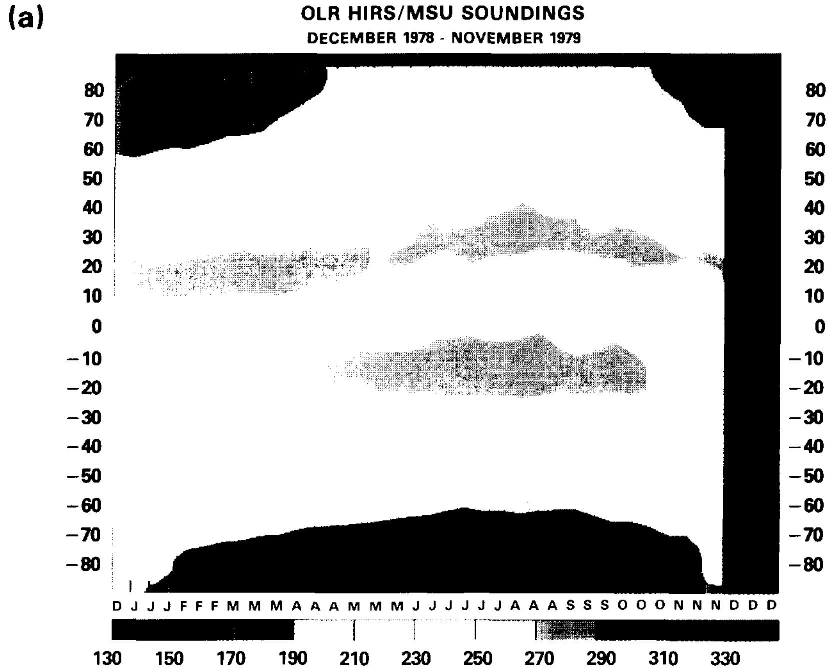

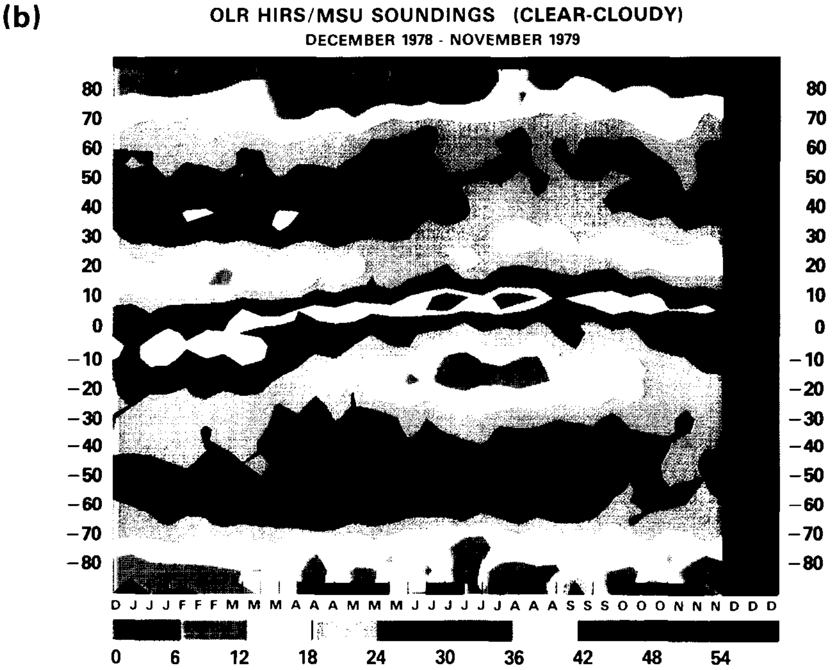

Figure 18 (a) Zonal mean outgoing longwave radiation (W m^{-2}) computed from HIRS2/MSU soundings every 1/3 of a month for the period December 21-31, 1978 to November 21-30, 1979. (b) As in (a) but for the difference of OLR computed assuming clear conditions and that computed using retrieved cloud conditions.

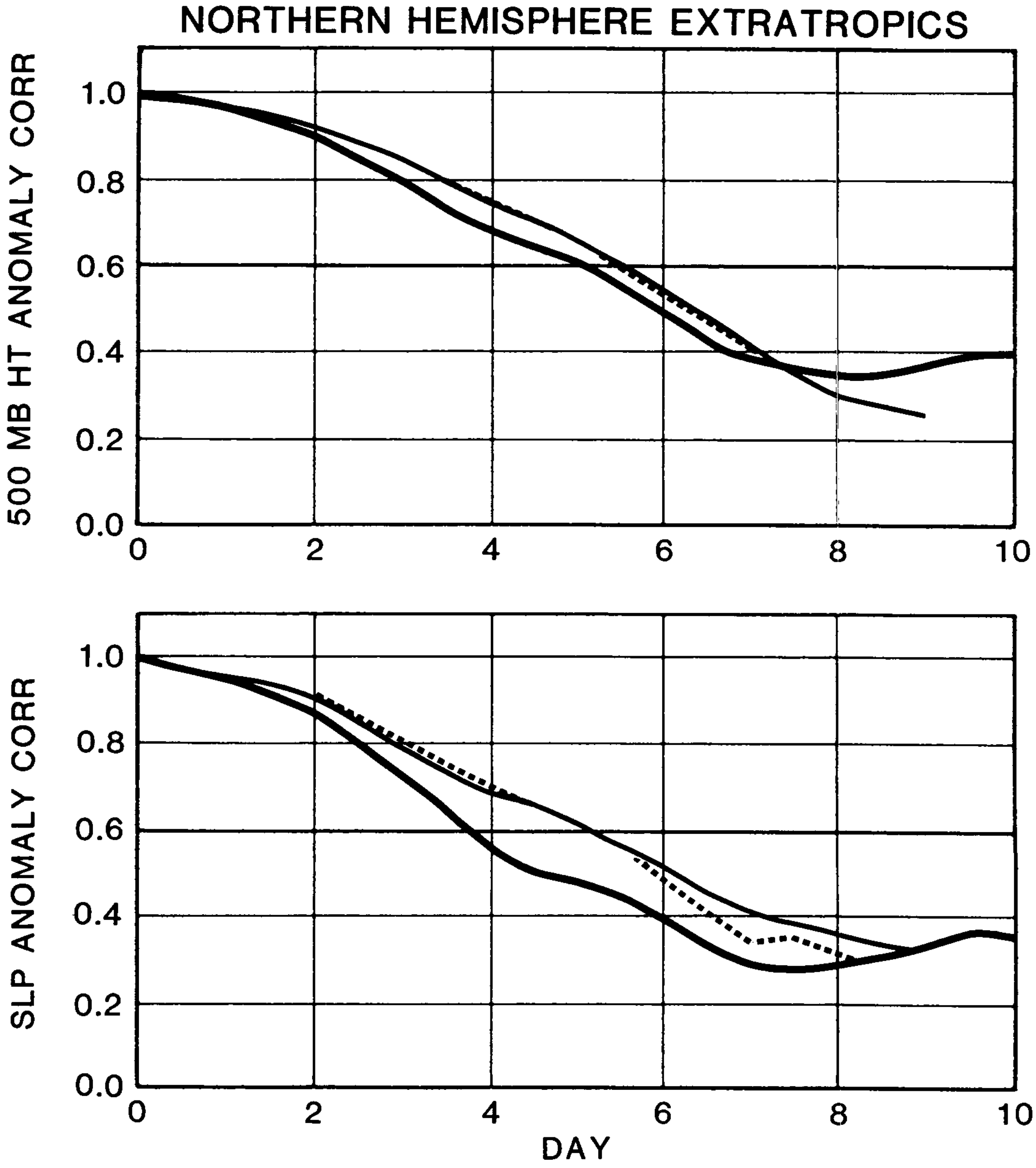

Figure 19 Ensemble mean anomaly correlations for 500 mb geopotential height (top panel) and sea-level pressure (bottom panel) over the extratropics of the Northern Hemisphere. The heavy line represents an ensemble of 5 winter forecasts with the 4° by 5° model without gravity-wave drag. The solid and dashed lines represent ensembles with the 2° by 2.5° model with and without gravity-wave drag, respectively.

predictions over the extratropics of the Northern Hemisphere. An anomaly correlation coefficient greater than 0.6 is considered to be indicative of useful predictive skill. Over Europe, SLP forecasts have improved by 24 hours after 3 $^1/_2$ days and 500 mb forecasts have improved by that amount by day 4 (Figure 20). Forecast improvements over North America (Figure 21) are equally impressive. However, after 6 $^1/_2$ to 7 days, the anomaly correlations for the coarse-resolution model exceed those of the fine-resolution model (although the average correlations for this time signify a loss of useful skill at either resolution). This "crossover" in resolution impact can be attributed to the excessive "climate drift" of the fine-resolution model.

Following the work of Palmer et al. (1986) and McFarlane (1987), a subgrid-scale, orographic gravity-wave-drag (GWD) parameterization has been introduced into the high-resolution model to alleviate the errors and biases associated with the model's climate drift. The fine-resolution forecast ensemble has been repeated with the GWD parameterization. Anomaly correlations for Northern Hemisphere extratropical SLP (Figure 19) have improved after day 6 and the resolution "crossover" has been delayed by one day. Improvements in 500 mb height anomaly correlations are less evident, but the GWD scheme has resulted in smaller rms errors in both scores throughout the entire forecast period. Skill at the 500 mb level has been improved in the GWD ensemble after 6 days over Europe (Figure 20) and after 5 days over North America (Figure 21). More dramatic is the improvement in sea-level-pressure forecast skill over Europe; however, there is a loss of SLP skill over North America after 3 days.

These results suggest that the gravity-wave-drag parameterization gives an overall improvement to the high-resolution GLA model, but that further development of the GWD parameterization is necessary, especially as regards forecast skill over North America. Accordingly, studies are being carried out on the effects of modifying the scheme's lower and upper boundary conditions and its specification of the vertical distribution of wave-stress divergence.

The Arakawa-Schubert (1974) cumulus parameterization scheme has been implemented in the Fourth-Order Model together with parameterizations for (a) the evaporation of raindrops falling from stratiform and convective clouds, (b) the radiative feedback due to fractional cloud-cover, and (c) the diffusion of moisture and momentum due to dry convection. These changes have led to an improved simulation of the July climatology and to a better forecast of the Presidents' Day Storm of February 1979. (Figure 22).

The development of a nonuniformly-spaced 12-level version of the GLA model has continued with three layers in the lowest 100 mb. This model explicitly resolves the vertical structure and dynamics of the planetary boundary layer (PBL) by using Monin-Obukhov similarity theory to predict the structure of the extended surface layer and a second-order turbulence closure model to predict turbulent fluxes between the resolved layers. The model is run with the Arakawa-Schubert cumulus parameterization, the evaporation of falling raindrops, and fractional cloud cover.

The 12 layer model has produced a slightly more skillful forecast for the period of the President's Day Storm than has the standard 9-layer model with the Arakawa-Schubert parameterization and other modifications (Figure 23). Further testing of the 12-layer model is currently in progress.

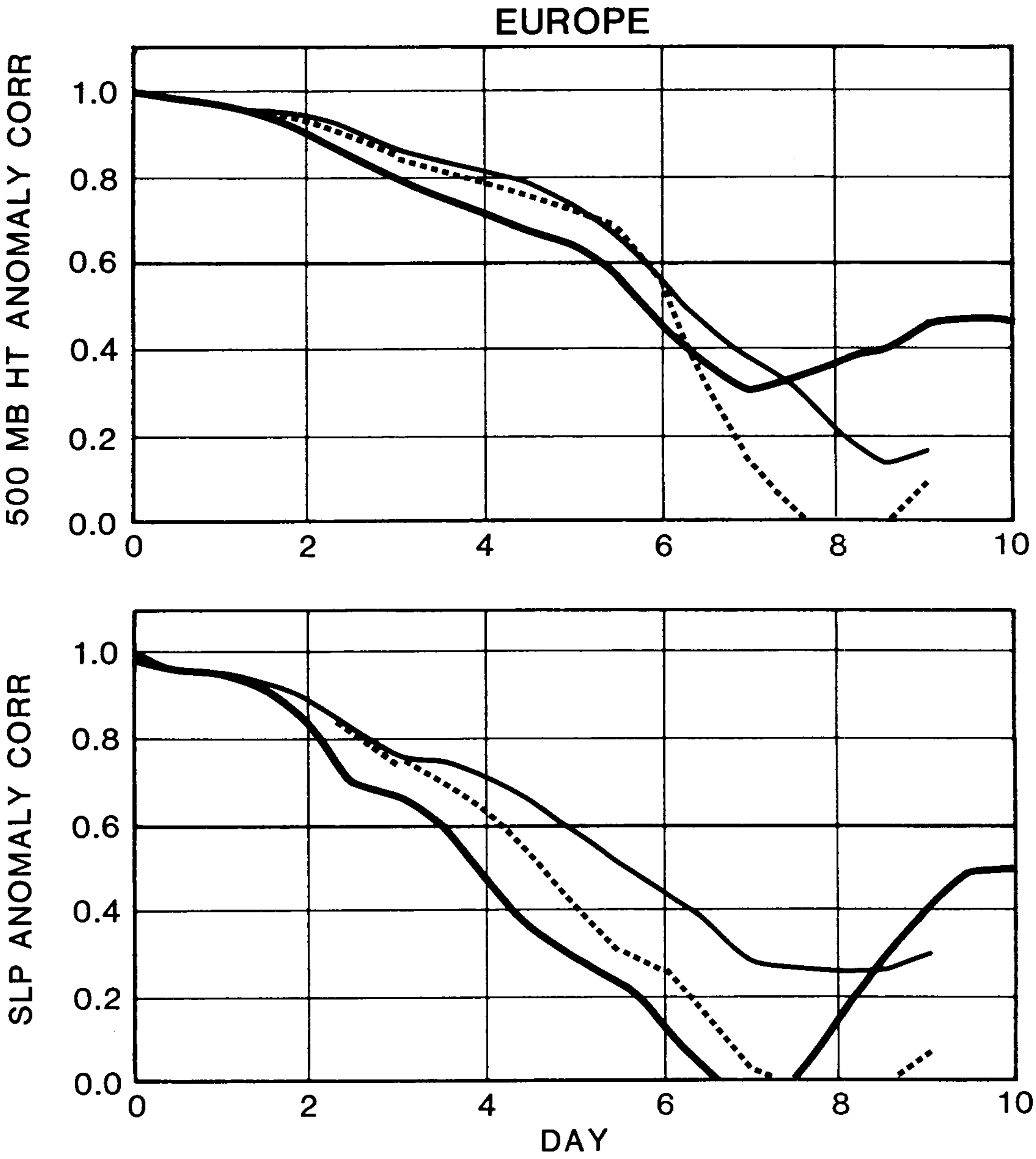

Figure 20 The same as Figure 19 but over Europe.

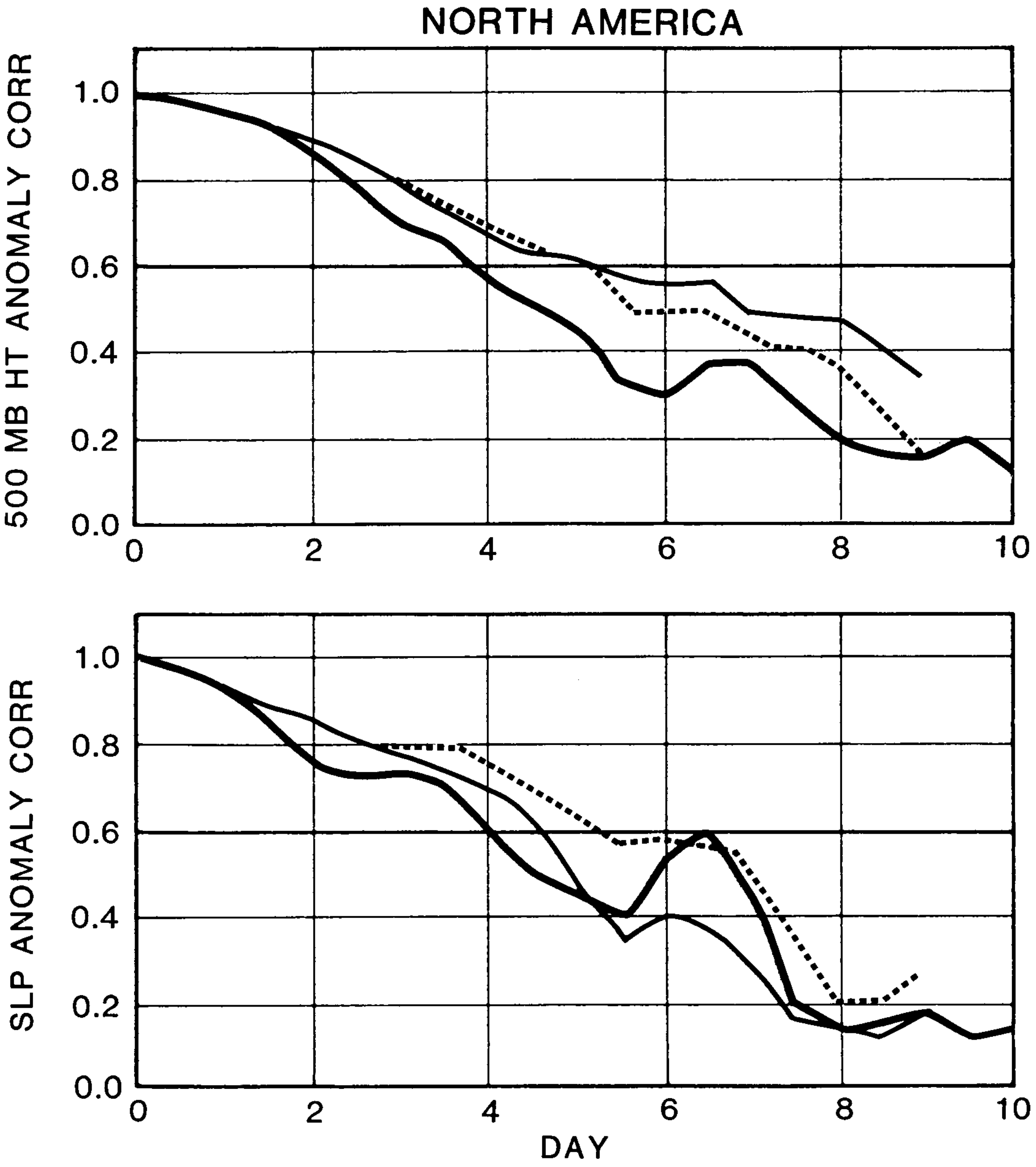

Figure 21 The same as Figure 19 but over North America.

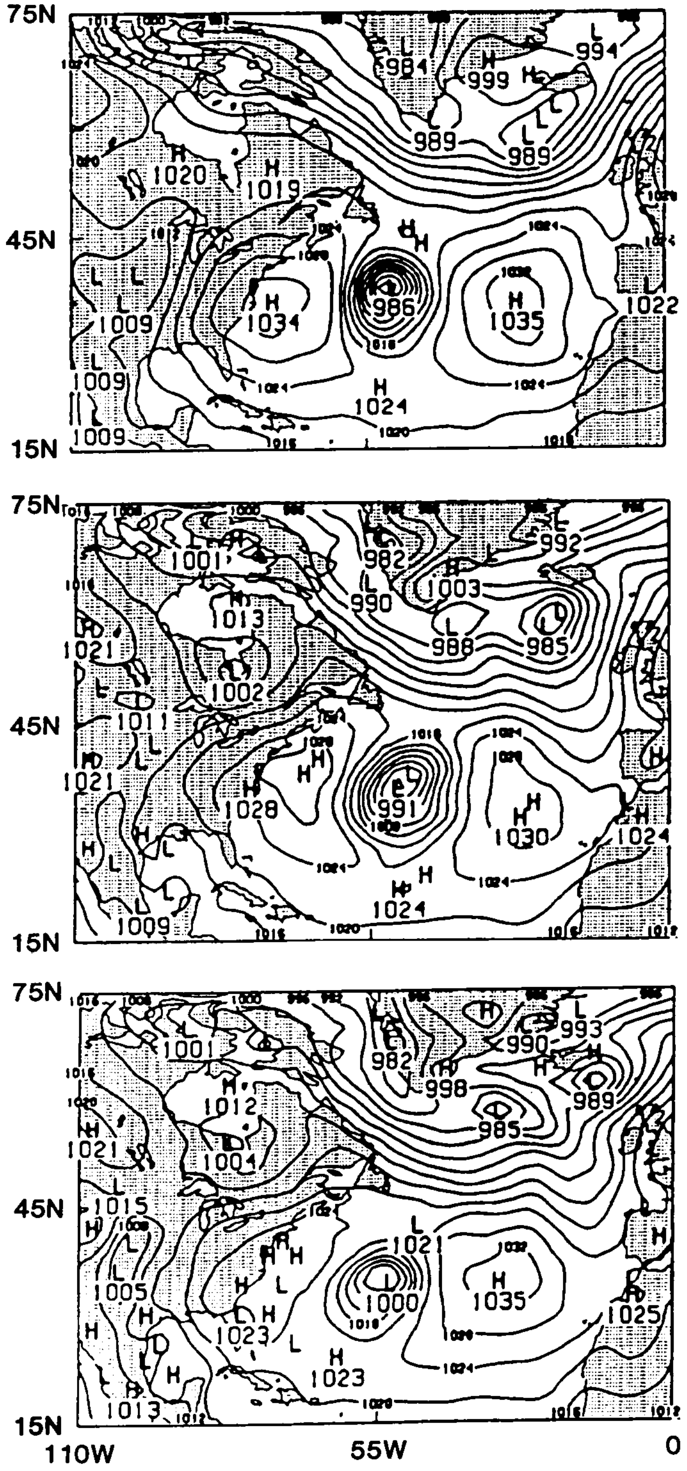

Figure 22 The Presidents' Day Storm. The top panel is a European Centre analysis for sea-level pressure for 00 GMT 21 February 1979. The middle and bottom panels are 72-hour SLP forecasts for this time by the 2° by 2.5° GLA model (with gravity-wave drag) with and without the Arakawa-Schubert cumulus parameterization, respectively.

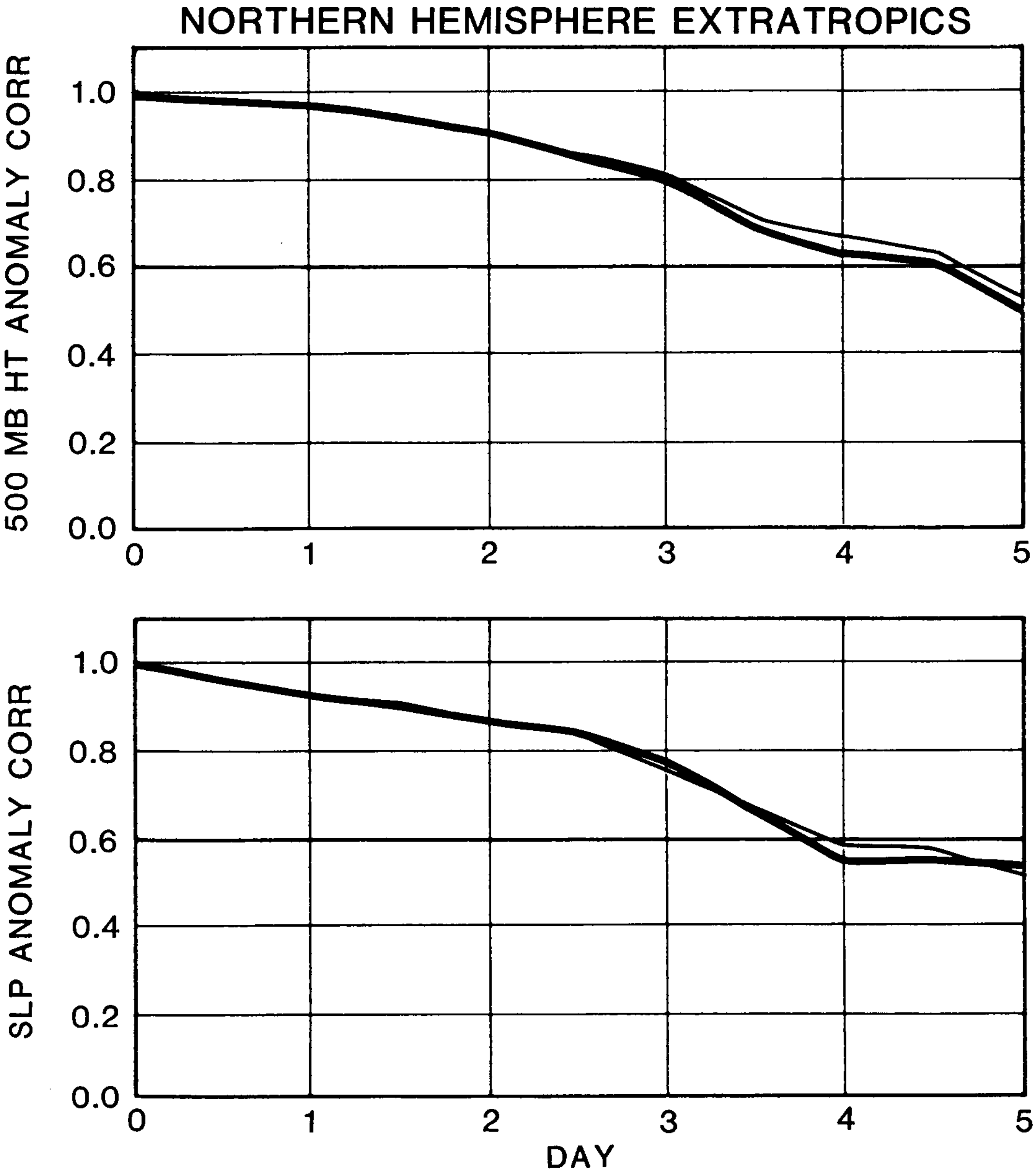

Figure 23 Anomaly correlations for 500 mb geopotential height and sea-level pressure for the extratropics of the Northern Hemisphere for forecasts initiated from 00 GMT 18 February 1979. The heavy line represents a forecast with the standard 9-layer model with Arakawa-Shubert parameterization while the light line represents a forecast with the 12-layer model with the "explicitly resolved PBL" and the Arakawa-Schubert scheme.

Four-Dimensional Data Assimilation (W. Baker, S. Bloom[1], J. Pfaendtner)

The objective of four-dimensional data assimilation is the production of a blend of observational data and model-produced forecast fields on a regular three-dimensional spatial grid at regular time intervals. This blend of observations and forecast first guess, the analysis, must be consistent with both the dynamics of the atmosphere and with known or plausible error characteristics of the observations and the forecast fields. The analyses can be used to initialize forecast models for numerical weather prediction. In addition, together with diagnostic quantities such as heating rates, vertical velocity, and precipitation generated by the model during the data assimilation processes, the analyses are used in diagnostic investigations of the general circulation.

At GMSB, recent data assimilation research has focused on the development and refinement of an optimum interpolation (OI) objective analysis scheme. Such a scheme is currently used by most operational global forecast centers and research groups. A main strength of the OI approach is its explicit use of observational and forecast error statistics. This feature of OI is especially important in a research environment such as that at GMSB. Investigations and evaluations of existing and future satellite-based components of the meteorological observing system play a large role in the research program. Because instrument error characteristics are an integral part of the OI process, the OI is ideally suited to help quantify the expected benefits of alternate observing system configurations and instrument designs.

The OI is described in detail in Baker *et al.* (1987). Two versions have been developed, a 12 level, three-dimensional, tropospheric version with a top analysis level at 50 mb, and an 18 level, two dimensional tropospheric-stratospheric version with a top analysis level at 0.4 mb. This latter version is coupled with a tropospheric-stratospheric model and is discussed in the next sub-section. The OI is multivariate in surface pressure and the surface wind components over the oceans. In contrast to the geostrophic coupling used for the height-wind analysis at the atmospheric levels over the surface, the OI uses a form of Ekman balance for the oceanic pressure-wind surface analysis.

Figure 24 depicts the main features of the four-dimensional data assimilation system proposed for use with data from the Earth Observing System (Eos) instruments. An important and unique feature of this system is that the retrieval process (computation of geophysical parameters from space-borne instrument data) is done interactively during the data assimilation process. The current prototype system includes the GLA physical retrieval method (described in Section III.) which provides temperature and moisture soundings as well as estimates of surface temperature, albedo, cloud height and amount, and total ozone using the HIRS2 and MSU radiance data from the NOAA polar orbiters.

At present, only the temperature soundings are being used in the

---

[1] Universities Space Research Association

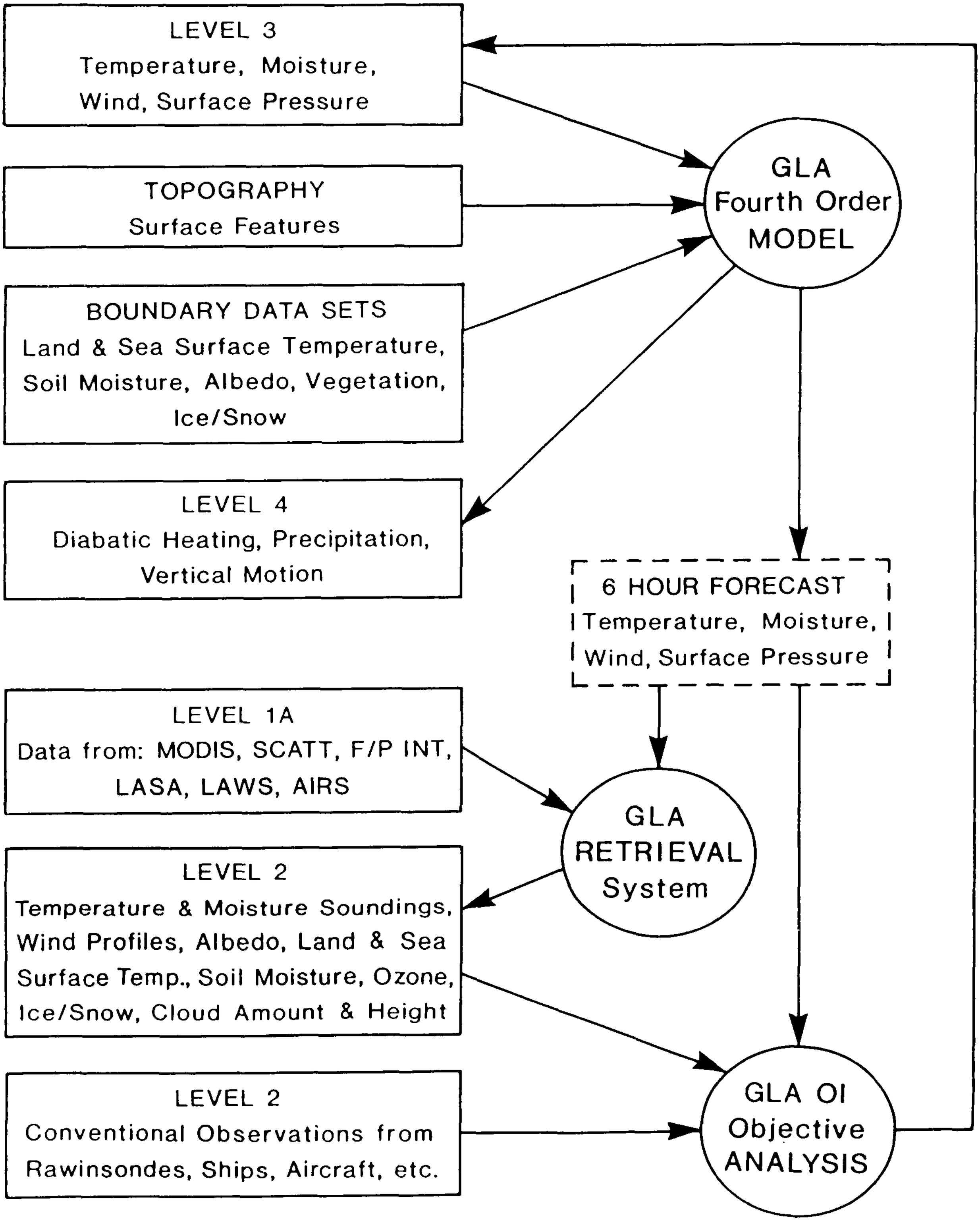

Figure 24 Schematic flow diagram of the proposed Eos interactive analysis/forecast/retrieval system.

subsequent data assimilation, but the quality of the other geophysical parameters, which are interesting in their own right, is also potentially improved because the retrieval process benefits from the accurate first guess information provided by the model. Present and future research will be aimed at increasing the interdependences and feed-backs in the system by assimilating additional parameters. For example, use of the humidity profiles in the subsequent moisture analysis and the sea surface temperature retrievals to perform a sea surface temperature anomaly analysis should improve the accuracy of the entire system. Comparison of model-produced cloud information with cloud parameters produced by the retrievals allows for consistency checks and a means of improving our understanding of cloud processes.

In addition, the system provides an optimal framework in which to do the retrieval process for new space-borne instruments. More sophisticated retrieval algorithms designed to make use of the high quality atmospheric state variables and other first guess data provided by the system cannot help but be more accurate than those which do not have the advantage of this additional information. For example, there is an active program aimed at using the data assimilation system and the first guess information it provides to retrieve dynamically consistent oceanic surface wind fields from scatterometer data. Plans have also been initiated to incorporate data and retrieval processes for future instruments such as AIRS (Atmospheric Infrared Sounder), MODIS (Moderate-Resolution Imaging Spectrometer), NSCAT (NASA Scatterometer), and LAWS (Laser Atmospheric Wind Sounder) into the four-dimensional data assimilation system.

Stratospheric/Tropospheric Data Assimilation System (W. Baker, K. Takano[1])

A four-dimensional stratospheric/tropospheric data assimilation system with a top analysis level at 0.4 mb (Takano et al., 1987) has been developed and used to produce physically-consistent gridded analyses for the stratosphere as well as the troposphere. The system consists of a two-dimensional optimum interpolation analysis scheme with a 19 level stratospheric/tropospheric general circulation model. Stratospheric data including LIMS (Limb Infrared Monitor of the Stratosphere), TIROS-N retrievals, rocketsondes, and VTPR (Vertical Temperature Profile Radiometer) soundings are used in addition to the other FGGE level IIb data.

Through the use of this system, physically-consistent mass and motion fields are obtained, as well as other quantities not directly measured such as stratospheric vertical velocity and heat and momentum fluxes. These can then be used to study the stratospheric general circulation without the need to assume geostrophic winds in the stratosphere, as was required in previous studies. In addition, the temperature and motion fields produced by the system are essential for stratospheric constituent transport and stratospheric chemistry studies.

When the stratospheric/tropospheric model is initialized using the optimum interpolation stratospheric/tropospheric analysis, it produces a

[1] Courant Institute of Mathematics

significantly more skillful medium range prediction than when initialized using previously available NMC stratospheric temperature analyses winds derived geostrophically. Figure 25 compares the mean zonal winds predicted by the model at days 4 and 10 for two forecasts. The initial conditions for 12 GMT, 17 February 1979 for these two forecasts are also shown. In the one case, that labeled GLA/NMC, the initial conditions were created by combining the GLA tropospheric analysis with the operational NMC stratospheric analysis. The other initial conditions, labeled OI, were obtained from the stratospheric optimum interpolation system. After four days, both forecasts and the verifying OI analysis exhibit easterlies in the polar stratosphere associated with the sudden stratospheric warming descending into the lower stratosphere. The forecast easterlies, especially in the OI case, are weaker than in the verification. However, after 10 days both the OI verification and the OI forecast show much stronger easterlies whereas the GLA/NMC forecast has no easterlies at all. The stratospheric westerly jet is also better represented in the OI forecast. The subtropical jet is well represented in both experiments throughout the prediction.

Numerical Prediction Experiments Related to the Summer 1980 U.S. Heat Wave

(R. Atlas, N. Wolfson[1], Y. Sud)

A diagnostic study and numerical experiments are being conducted with the GLA fourth-order model in order to study the initiation, maintenance, and decay of the severe summer 1980 U.S. heat wave and drought as well as the predictability of similar events. This has consisted of: (1) an analysis of the wave structure associated with the summmer 1980 heat wave and a comparison of this wave structure with climatology and with other anomalous years, (2) the development of an objective procedure for characterizing heat waves in numerical model predictions and tests of this index on summer 1980 observations and numerical forecasts, (3) a medium range numerical forecast experiment designed to assess the role of boundary forcing in the maintenance and decay of the heat wave, and (4) a series of long-range predictions from different initial data and boundary conditions to determine if any skill actually exists in numerically forecasting the initiation of the heat wave on a variety of time scales. These include: (a) nine two and one-half month control (C) forecasts with climatological boundary conditions - three from 1980 at 0000 GMT 14 May, 0000 GMT 15 May, and 0000 GMT 16 May, and three each from the non-heat wave years 1979 and 1982 for the same dates, (b) three two and one-half month forecasts from 0000 GMT 14 May 1980, 0000 GMT 15 May 1980, and 0000 GMT 16 May 1980 in which either observed sea-surface temperatures (SST) from 40°S to 60°N for 1980 or derived soil moisture (SM) values over North America for 1980 were used to replace the corresponding climatological values, and (c) three additional two and one-half month (SM + SST) forecasts from 0000 GMT 15 May 1980 and 0000 GMT 16 May 1980 in which both observed SST and derived SM values for 1980 replaced the corresponding climatological values.

The results of these experiments show sensitivity of the extended-range

---

[1] Tel Aviv University, Department of Geophysics and Planetary Sciences, Ramat Aviv, Tel Aviv, Israel.

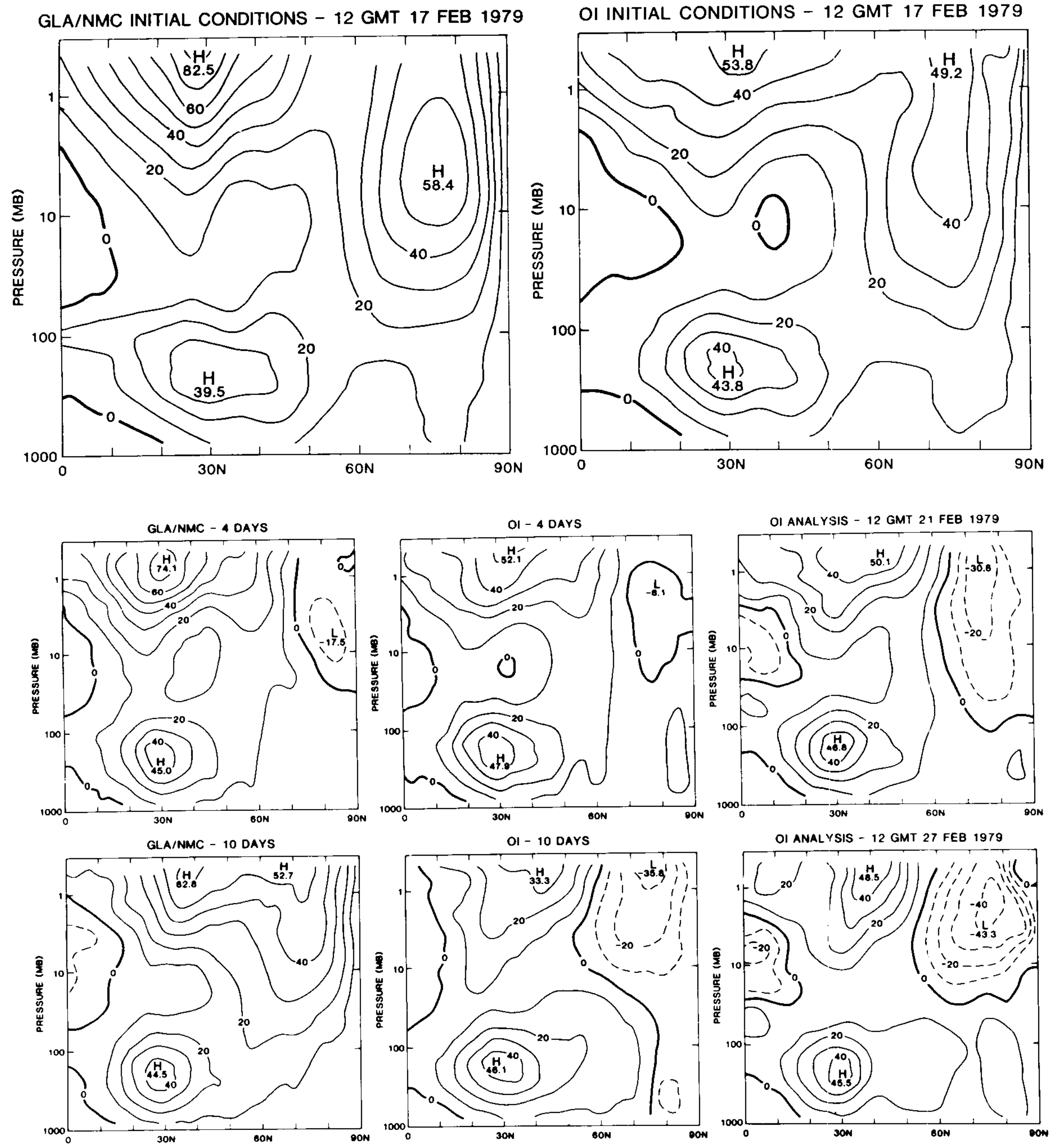

Figure 25 Mean zonal winds in ms^{-1}. Top: 12 GMT 17 February 1979 analyses. Middle: Four-day forecasts and verifying OI analysis. Bottom: Ten-day forecasts and verifying OI analysis.

predictions of the heat wave to both the initial conditions and boundary forcing. Comparison of the boundary forcing experiments showed the combined influence of soil moisture and sea surface temperature anomalies to be more significant than either effect alone and indicated that the effect of a specific boundary data set is strongly influenced by the other boundary conditions. In addition, the effect of anomalous boundary forcing was found to be enhanced by the removal of the model's climate drift. This latter effect is illustrated in Figure 26, which shows the accuracy of the model predictions of the heat wave index (HWI) over the northern and southern plains of the U.S.

Global Surface Wind and Flux Fields from the Assimilation of Seasat Data

(R. Atlas, A. J. Busalacchi[1], S. Bloom, M. Ghil[2], E. Kalnay[3])

Surface fluxes of heat, moisture, and momentum between the oceans and atmosphere play a major role in the formation, movement, and modification of water and air masses, and in the development and intensification of storms near coasts and over the open ocean. The determination of these fluxes is extremely important for numerical modeling and diagnostic studies of these and other atmospheric and oceanic phenomena and for numerical prediction on a variety of time scales. However, such determinations have been limited to a large extent by the lack of adequate observations of even the most fundamental meteorological variables over the oceans.

With the launch of the Seasat satellite in June 1978, a new data source for surface winds became available. On board was the Seasat-A Satellite Scatterometer (SASS) which measured radar backscatter from centimeter scale capillary waves. An empirical relationship referred to as the SASS 1 model function was used to infer surface wind velocity from these measurements. However, SASS 1 provided up to four possible wind directions, called aliases, with each report. Thus, before these data could be utilized in meterological analyses or in diagnostic and numerical studies, this ambiguity in wind direction had to be removed.

We have recently applied an objective scheme to dealias, or remove, the directional ambiguity from the complete 96-day global Canadian Atmospheric and Environmental Service SASS 1 data set from 0000 GMT July 7, 1978 to 0000 GMT October 10, 1978 (Atlas et al., 1987). These data have been assimilated using the GMSB analysis/forecast system to produce global-gridded surface wind fields at 6-hour intervals. In addition, as a by-product of the assimilation process, global-gridded fields of surface wind stress and of sensible and latent heat fluxes across the air-sea interface were generated at 6-hour intervals and time averaged to produce monthly mean fields.

Figures 27 and 28 present the monthly mean wind stress and latent heat flux fields for July-September 1978 obtained from the GLA model assimilation. These fields are in good general agreement with previously

1 NASA/Goddard Laboratory for Oceans
2 University of California - Los Angeles
3 NOAA/National Meteorological Center

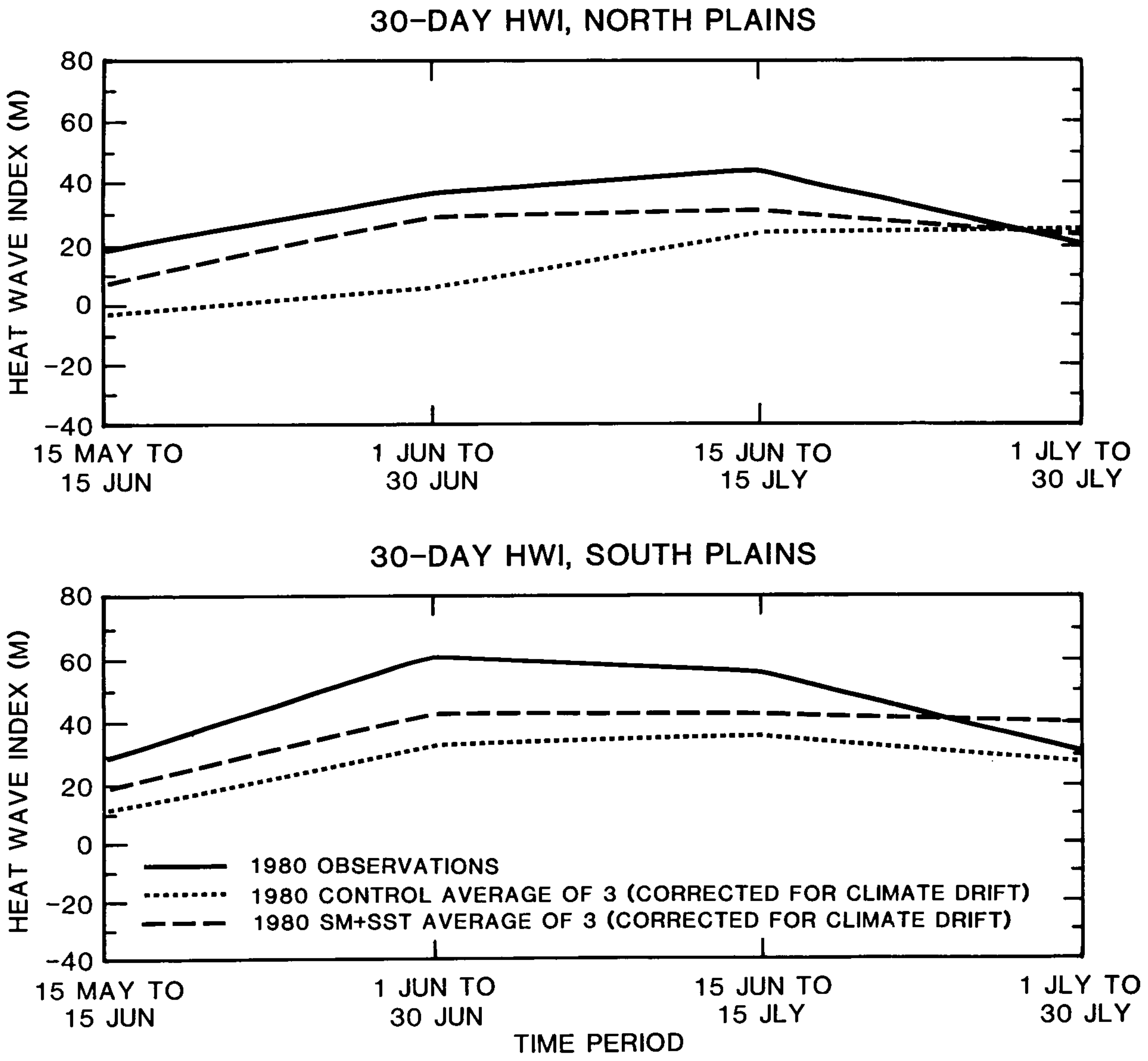

Figure 26 Thirty day average 1980 observed Heat Wave Index (HWI) and 1980 C and SM+SST forecasts of HWI (after removing the estimated model climate drift) for the North and South Plains.

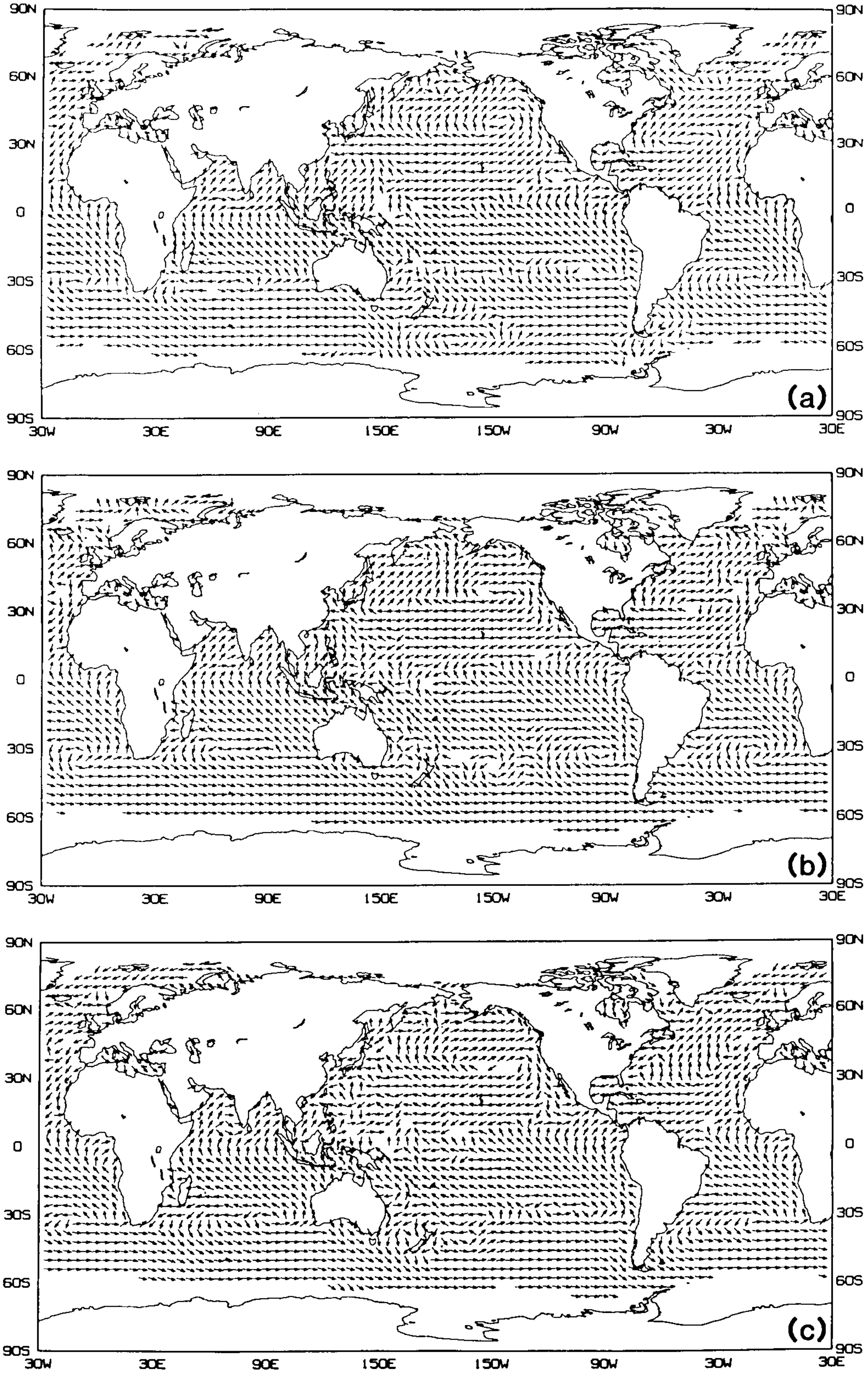

Figure 27 Monthly mean wind stress directions from the GLA assimilation using SASS winds for (a-c) July-September 1978.

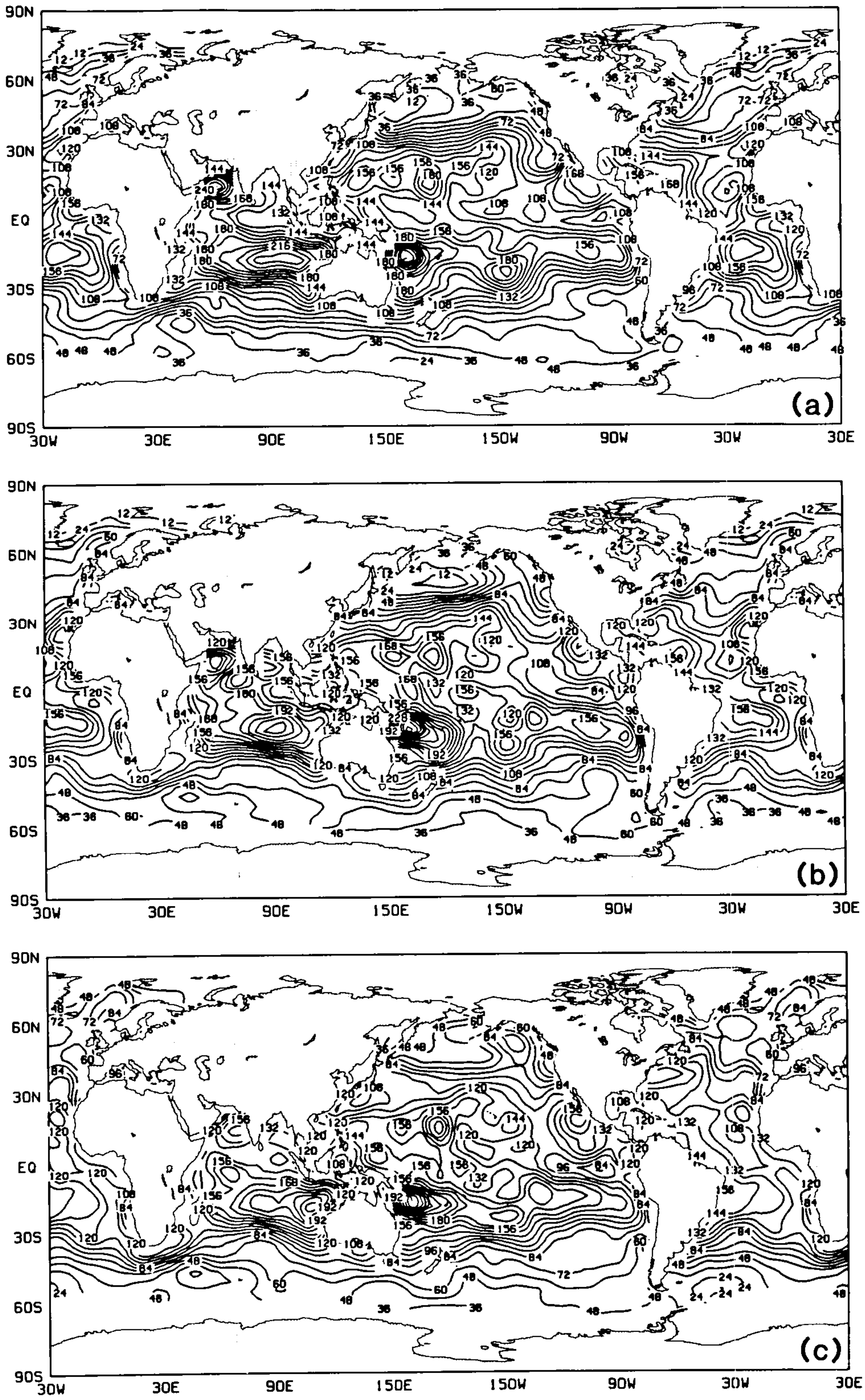

Figure 28 Monthly mean latent heat flux (in watts per square meter) fields from the GLA assimilation using SASS winds for (a-c) July-September 1978.

published climatologies. But they show considerable more detailed structure due primarily to the unprecedented coverage of Seasat.

IV. CLIMATE RESEARCH HIGHLIGHTS (D. Randall)

Climate research in the Global Modeling and Simulation Branch spans a wide variety of topics. We have chosen to highlight cloud-climate studies, ocean-atmosphere studies, earth-atmosphere interaction studies, and seasonal cycle simulation studies.

Cloud-Climate Studies (D. Randall)

A key problem in climate dynamics is to determine the role of cloudiness in climate change. The clouds are a reflecting blanket; they cool the planet by reflecting sunlight back to space, and warm it by trapping terrestrial radiation. It is not clear a priori whether cooling or warming wins out. Important new observational datasets which can shed light on this question are being produced through the International Satellite Cloud Climatology Project (ISCCP), the First ISCCP Regional Experiment (FIRE), and Earth Radiation Budget Experiment (ERBE).

In order to provide a framework for analysis and interpretation of these data, simulation studies of global cloudiness and its effects on climate have been carried out with the UCLA/GLA GCM. Results from the GCM are being analyzed to determine the simulated global distribution of cloudiness, the interactions of the clouds with large-scale circulations and the hydrologic cycle, and sensitivity to aspects of the model's formulation. Data from ISCCP, HIRS2/MSU, Nimbus 7, and conventional sources have already been used for validation. Particular attention is being given to cloud radiative forcing (CRF), the interactions of cloudiness with cumulus convection and boundary layer turbulence, and diurnal variability.

The CRF is defined as the difference between a radiation flux in the presence of clouds and that which would occur in the absence of clouds with all other fields unchanged. Here we briefly examine some CRF results from a July simulation with the GCM.

According to the model results, the net CRF is a cooling of -19.3 Wm^{-2} for the planet as a whole. The solar component of -47.6 Wm^{-2} thus dominates, although the longwave component of 28.3 Wm^{-2} is of comparable magnitude. These forcings are associated with a simulated planetary albedo of 29% and a simulated outgoing longwave flux of 233 Wm^{-2}, which are in good agreement with satellite observations. In a global sense, both the longwave and shortwave CRFs are felt almost entirely by the surface; the atmosphere is hardly affected. This is true even locally for the solar CRF, but as shown in Fig. 29, the terrestrial CRF has broad regions of intense positive and negative values which nearly cancel in the global mean. In the Western Equatorial Pacific, the warming approaches 100 Wm^{-2}, while near the poles the cooling exceeds -40 Wm^{-2}. For comparison, a precipitation rate of 1 mm day^{-1} corresponds to a latent heating of 27 Wm^{-2}.

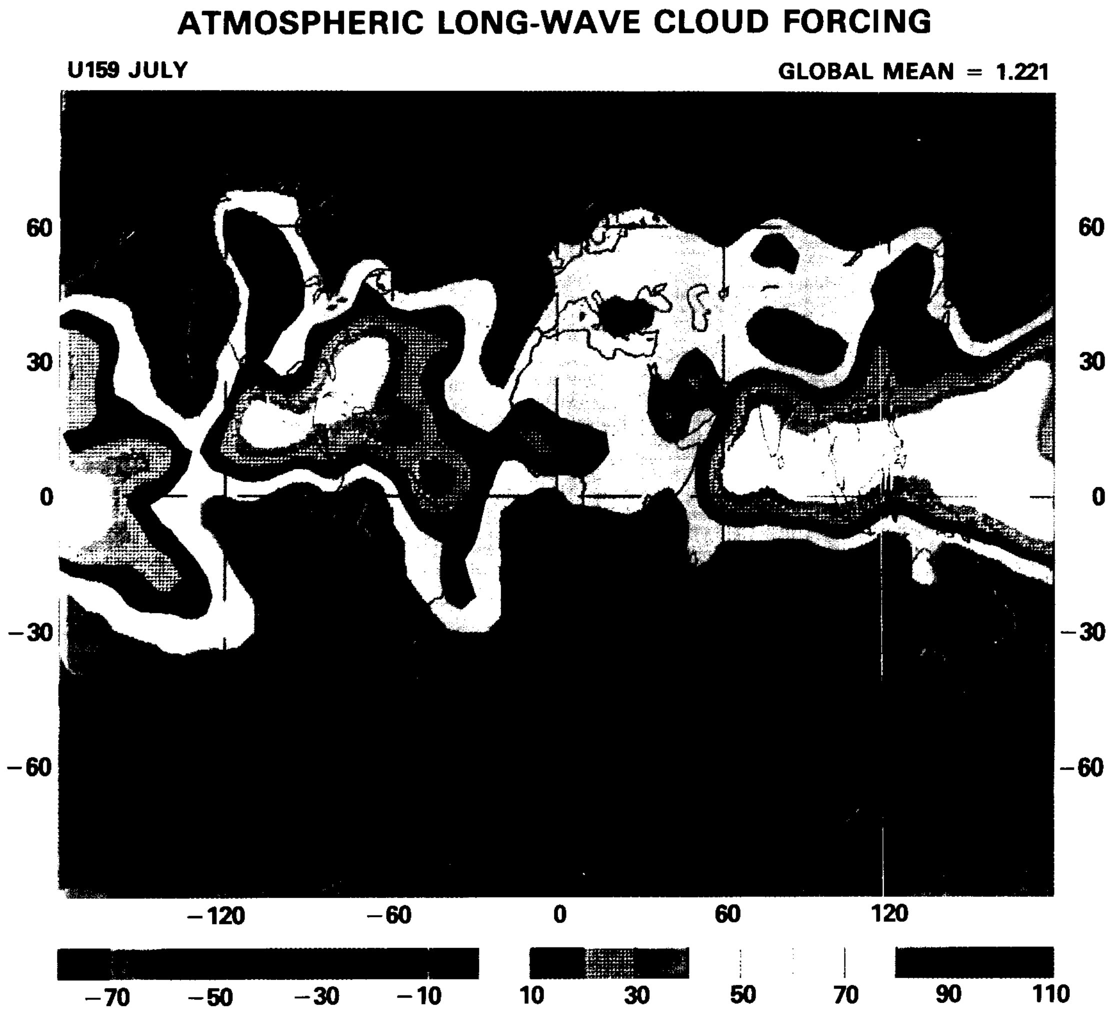

Figure 29 July atmospheric long-wave cloud radiative forcing simulated by the UCLA/GLA general circulation model.

ORIGINAL PAGE
COLOR PHOTOGRAPH

The clouds warm or cool the atmosphere depending on the altitude at which they occur. A high cold cloud tends to warm the atmosphere because it absorbs intense radiation from the earth's surface while emitting only weakly. In contrast, a low warm cloud tends to cool the atmosphere because it emits strongly both upward and downward while strong absorption occurs only on its lower side. Since high clouds are common in the tropics, while low clouds occur frequently near the poles, the zonally averaged atmospheric CRF is a warming in the tropics and a cooling in higher latitudes, thus demanding a poleward heat transport by the atmosphere in addition to that required by latent heating. The zonal structure of the atmospheric CRF is also very strong, with warming at longitudes of rising motion where high clouds occur, and cooling at longitudes of sinking motion where low clouds occur. The vertical motion field induced by the atmospheric CRF thus tends to feed back positively on the clouds. This tantalizing result suggests the possibility of radiative-dynamic instabilities.

Sensitivity tests with the GCM show that the high cloudiness associated with cumulus convection tends to suppress convection over land. This negative feedback is due to cloud shadows which lead to a reduction in the surface evaporation. A similar negative feedback with a longer time scale may operate over the oceans. A coupled ocean-atmosphere model is needed to investigate this.

Unlike some other climate models, the UCLA/GLA GCM includes the diurnal insolation cycle. The diurnal variability of cloudiness and precipitation simulated by the model is very pronounced even over the oceans, and has an orderly geographical structure. Encouraging agreement with observed diurnal variations has been found. These realistic results have encouraged us to use the model to address a long-standing and controversial issue: Why is there a diurnal cycle of precipitation over the oceans? Among the possible explanations that have been proposed, we have investigated three: (1) absorption of solar radiation by clouds in the upper troposphere tends to stabilize the lapse rate, and so, inhibits moist convection during the day, but not at night, (2) solar warming induces diurnally varying large-scale vertical motions that, in turn, modulate the moist convection, and (3) diurnal heating of the continents forces diurnally varying circulations that extend over the oceans, influencing oceanic moist convection. These three hypotheses are not mutually exclusive; each can be partially correct.

Our results, obtained through a series of numerical experiments with the GCM, can be summarized as follows. First, a diurnal cycle of precipitation does occur even in the absence of continents, but its amplitude is only about half that obtained for the oceans in a control run with continents. This indicates that the diurnal cycle of precipitation over the oceans is partly due to the remote influence of the continents. Second, in a one-dimensional version of the GCM with prescribed vertical motion that is independent of the time of day, a diurnal cycle of precipitation occurs with phase and amplitude qualitatively similar to observations. This shows that direct coupling between radiation and convection does play a role in forcing the diurnal cycle of precipitation over the oceans. Finally, the diurnally varying vertical motions in the all-ocean run actually show *minimum* rising motion at the time and place of maximum rainfall, ruling out any possibility that vertical motions drive the diurnal cycle of the rainfall. Our results, therefore, tend to support the first hypothesis listed above.

In the coming year we plan to use FIRE data to develop an improved parameterization of marine stratocumulus clouds including the effects of the diurnal cycle, cloud-top entrainment instability, and fractional cloudiness.

Atmosphere-Ocean Interactions (M. Suarez)

In order to study the low-frequency behavior of the coupled ocean-atmosphere system, and particularly the El Nino/Southern Oscillation (ENSO), a coupled ocean-atmosphere model has been developed in collaboration with P. Schopf of the Goddard Laboratory for Oceans. Some of the results from this model, and the theory of ENSO we have developed from them, are discussed below.

The model consists of a two-layer primitive equations ocean coupled to a two-level primitive equations atmosphere. The ocean model is on an idealized, rectangular, equatorial basin while the atmospheric model is global. The ocean model predicts the thickness, temperature, and currents in two layers chosen to represent the tropical mixed-layer and thermocline. The atmospheric model is forced by relaxing its thermal structure to a "radiative equilibrium profile" with a large pole-to-equator temperature difference. This forcing is independent of longitude and time and is symmetric about the Equator. The two models are coupled by driving the ocean with a surface wind stress proportional to the atmosphere's lower level wind, and by adding to the atmosphere a mid-tropospheric heating proportional to the air-sea temperature difference.

The results presented below were obtained by integrating the coupled model for 35 years starting from a resting isothermal state. During the first 100 days, the Newtonian forcing produces an atmospheric general circulation including vigorous mid-latitude synoptic-scale transients. The resulting tropical easterly winds then spin-up an oceanic tropical circulation with an east-west sloping thermocline and an equatorial cold tongue in the eastern part of the basin. By year five, the system has reached an equilibrium with considerable low-frequency variability. Fig. 30 shows time sections of (a) equatorial anomalies of SST, (b) ocean surface height, and (c) lower level zonal wind. These have time-scales and horizontal structures (not shown) similar to those of observed El Nino events.

To explain these results, we have proposed a theory that relates the time-scale selection apparent in the figure to the time-scale of wave propagations in a closed equatorial ocean basin. The main difficulty in producing a "wave dynamics" theory for this time scale is that, whereas the propagation times in the basin are of the order of 300 to 400 days, the period to be explained is on the order of 1000 to 1200 days. Our theory solves this problem in two ways. First, it shows that the signal is reflected in the coupled region in such a way that solutions have periods of at least twice the propagation time. Second, a simple non-linear analog system is used to argue that periods of three to four times the propagation time are typical.

Recently, we have begun development of a much more elaborate model of the tropical ocean/global atmosphere system through which we hope to obtain a better understanding of ENSO. Separate development of the new atmosphere and ocean models is nearly complete, and we are now working on the coupling. The new ocean is a multi-layer reduced-gravity model on a equatorial basin with realistic geography. The new atmosphere includes topography, parameteriza-

ORIGINAL PAGE IS
OF POOR QUALITY

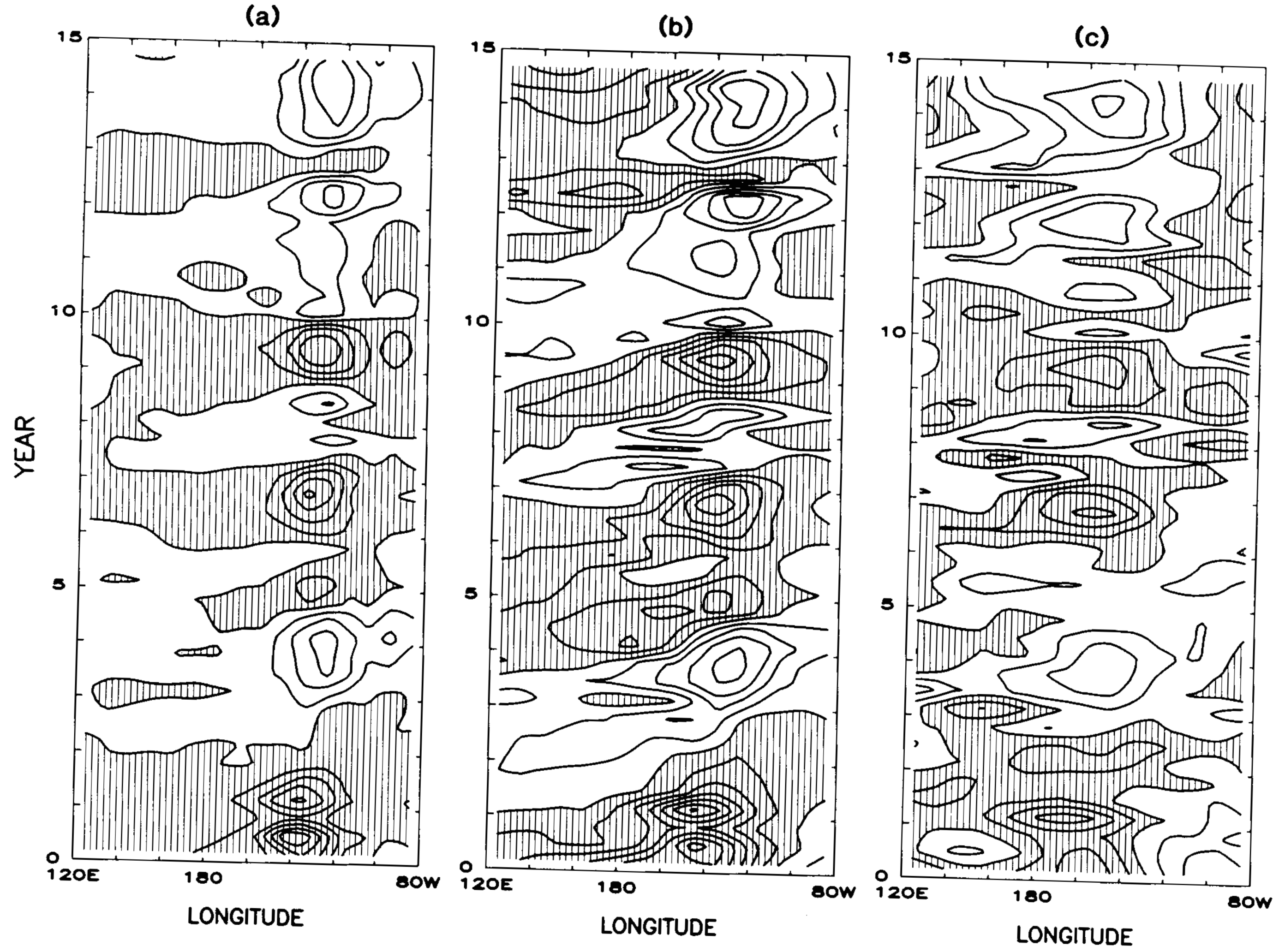

Figure 30 Time-longitude history of anomalies averaged between 2°S and 2°N from a 15 year simulation by the coupled models. (a) Sea surface temperature, contour interval = 0.5°C. (b) Ocean surface height, contour interval = 1 cm. (c) Lower level zonal wind, contour interval = 0.25 m/s. Negative anomalies are hatched.

tions of short and long wave radiation, boundary layer turbulence, and the hydrologic cycle. These models can be integrated with or without a seasonal cycle and in various basin configurations. They will eventually be developed into global coupled climate models.

Atmosphere-Land Surface Interactions (Y. Sud)

Over the last decade the importance of surface albedo and soil moisture anomalies for climate variability has been clearly established. Our work at GMSB has focused mainly on deserts and desert-border regions. We have shown that an increase in the surface albedo of a desert border region, which typically has very low evapotranspiration, produces boundary layer cooling. This cooling promotes sinking and drying aloft in accordance with the surface-albedo feedback hypothesis of J. Charney. The net effect is to reduce the rainfall in the desert-border region which helps to further promote desertification.

GCMs have been used to examine the sensitivity of summer rainfall in semi-arid regions to changes in the soil moisture. Our early results have indicated that regional soil moisture deficits have little effect on surface rainfall. In these early experiments, the deficits did produce decreased evapotranspiration and increased sensible heat flux, but the increased sensible heating led to thermally induced moisture convergence which compensated for the reduced evapotranspiration. As a result, the overall influence of the soil moisture deficits on the simulated rainfall was small.

We now believe that these early results were incorrect. An improved version of the GLA GCM shows significant sensitivity of precipitation to regional soil moisture anomalies. The main reason for the change in our results is that we have now included a realistic upward moisture mixing by vigorous dry convection. The enhanced surface sensible heat flux in dry-soil regions causes the boundary layer to deepen into the dry free atmosphere aloft. Downward mixing leads to a drying near the surface which inhibits the onset of moist convection. Meanwhile, the upper-level moisture is carried away by horizontal divergence. This revised GLA GCM has been used to study how North African circulation and rainfall depend on the surface albedo and soil moisture of the Sahara Desert. The results, which are shown in Fig. 31, indicate that surface evaporation can have a strong influence on the amount of North African rainfall and the northward intrusion of the ITCZ into the Sahel and/or southern Sahara.

Another important factor influencing local precipitation is surface roughness which is mainly determined by the height of the vegetation. We have performed controlled experiments to determine the influence of surface roughness on: a) deserts, b) the Indian Monsoon, and c) global circulation and rainfall. Figure 32 shows how decreased surface roughness affects the lateral convergence of water vapor in the frictionally controlled low-level model flow. Increased moisture convergence can lead to greater rainfall. This mechanism is particularly important in the tropics.

We have investigated the biogeophysical processes of desertification and the physical mechanisms responsible for Sahelian droughts. Deteriorating vegetation leads to increased surface albedo, weaker evapotranspiration, and reduced surface roughness. Our model results show that these changes tend to

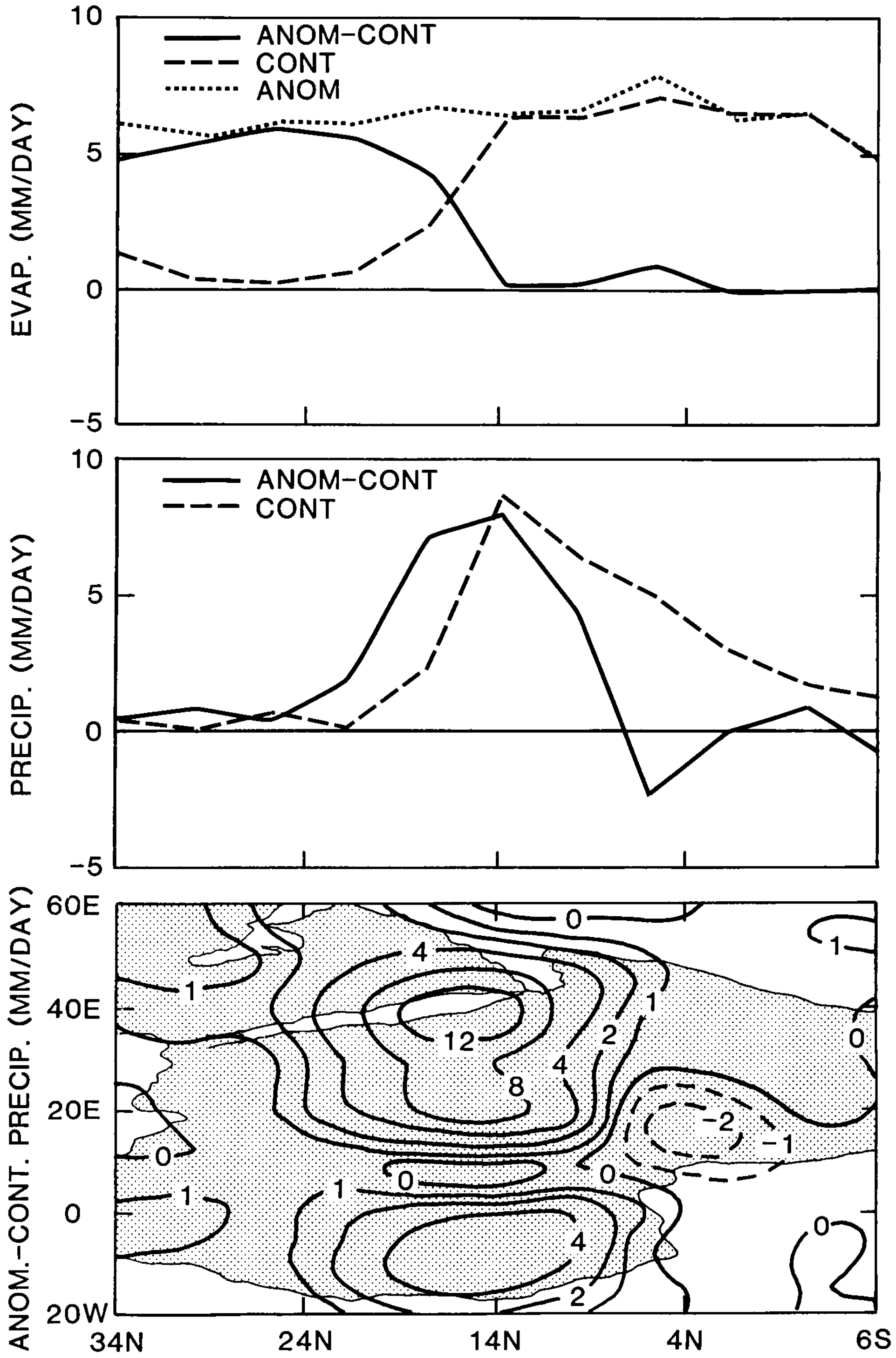

Figure 31 July average evaporation and precipitation in mm/day. Top: Zonal average evaporation for anomaly simulation, control simulation and the differences between anomaly and control. Middle: Zonal average precipitation for control run and the differences between anomaly and control runs. Bottom: Precipitation differences between anomaly and control runs.

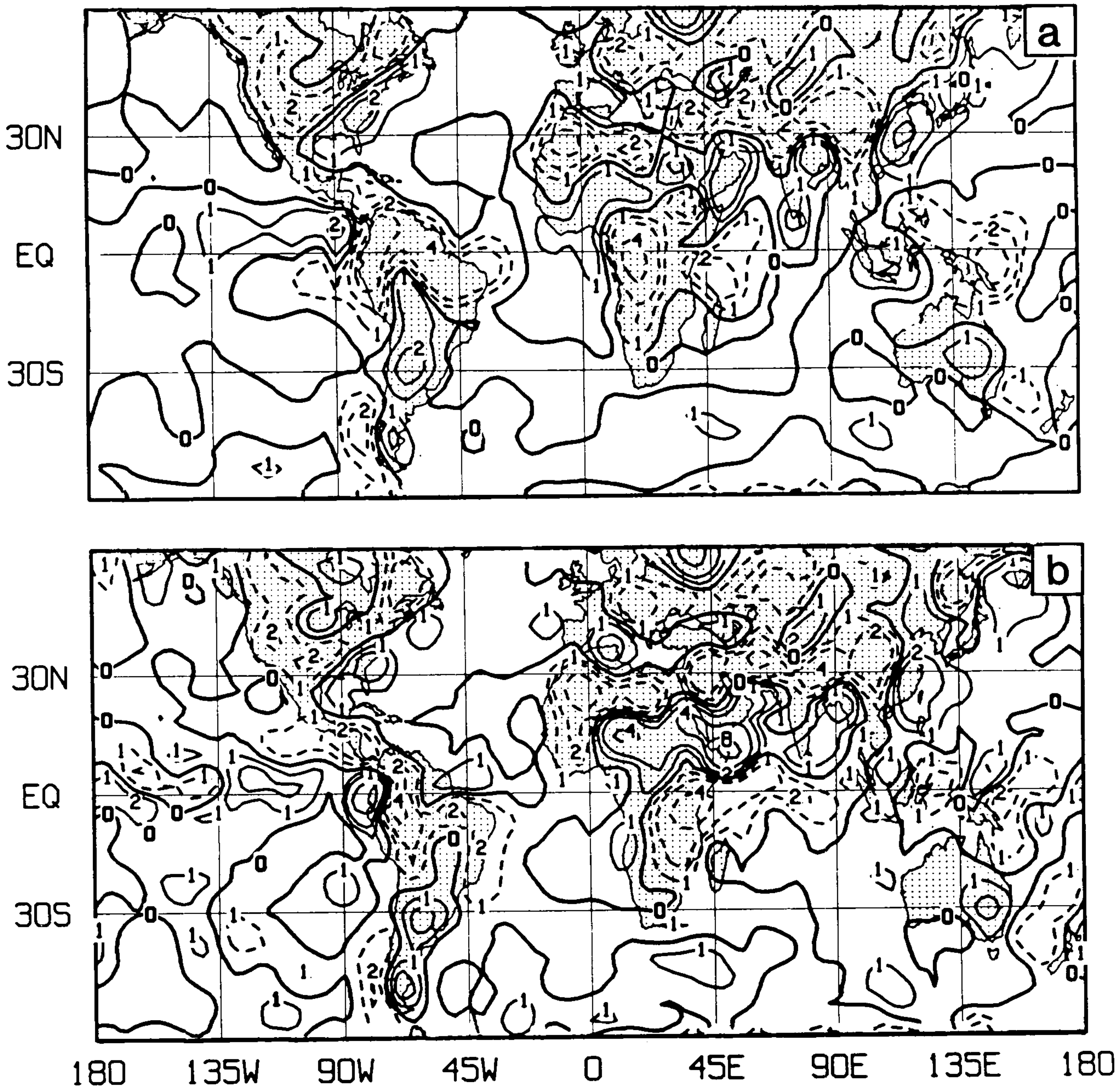

Figure 32 Influence of surface roughness of land on moisture convergence for simulated July. Shown are differences between the average of three anomaly (smooth) and control simulations. (a) Curl of surface stress divided by Coriolis parameter. (b) Moisture convergence.

reduce the rainfall, which causes the vegetation to deteriorate further. Through this biogeophysical feedback loop, an incipient drought can become self-promoting. This mechanism may be responsible for the ongoing expansion of the Sahara Desert.

We are also trying to explain the observed month-to-month fluctuations of Sahelian rainfall. Observational and modeling studies have revealed correlations between Sahelian rainfall anomalies and sea-surface temperature anomalies (Fig.33). These studies have shown that El Nino-like sea-surface temperature anomalies can lead to fluctuations in the Hadley circulation (Fig.34), which, in turn, affect rainfall throughout the tropics, including northern Africa.

Through these studies, our understanding of the basic mechanisms of earth-atmosphere interactions is improving. In the near future, we plan to use realistic satellite-derived distributions of vegetation and soil moisture as input to GCM simulations. In addition, we plan to use satellite-observed distributions of sea surface temperature and snow/ice extent. These realistic boundary conditions will enable us to more fully understand the impact of land-ocean-atmosphere interactions on rainfall and circulation.

Seasonal Cycle Simulation Studies (D. Straus)

During the past thirty years, general circulation models (GCMs) have been used in increasingly ambitious studies of the atmosphere. Early goals were to accurately simulate the annual or seasonal (usually winter or summer) mean climate using time-independent boundary conditions. Many of the important features of the atmospheric general circulation were correctly reproduced. These successes encouraged the use of GCMs to understand and predict climate fluctuations on a variety of time scales. Increasing computing power has made multi-year integrations practical, so it is now possible to model the seasonal cycle of the atmospheric general circulation.

The seasonal march of solar forcing and the associated changes in surface forcing due to the contrasting thermal properties of land and ocean produce large changes in the location and intensity of the tropical rain belts and in the amplitude and phase of the extra-tropical stationary waves, which then modulate the transient fluctuations. Seasonal changes in the circulation, temperature, and rainfall are larger than any recorded long-term climate changes.

We have investigated the seasonal cycle of the general circulation as simulated by the older GLAS Climate Model in a two-year integration in which the boundary conditions followed a prescribed seasonal cycle. Previous studies have shown that the GCM is remarkably successful in simulating the monthly and seasonal response of the atmosphere to observed changes in the boundary conditions at the earth's surface. One of the conclusions of our work is that the model is less successful in simulating the seasonal cycle.

The annual march of the 200 mb zonally averaged u-wind is shown in Fig. 35 which compares the GCM results with FGGE observations. The overall simulation of the seasonal cycle is quite good, although the Southern Hemisphere winter jet is clearly too strong and is located about 10 degrees too close to

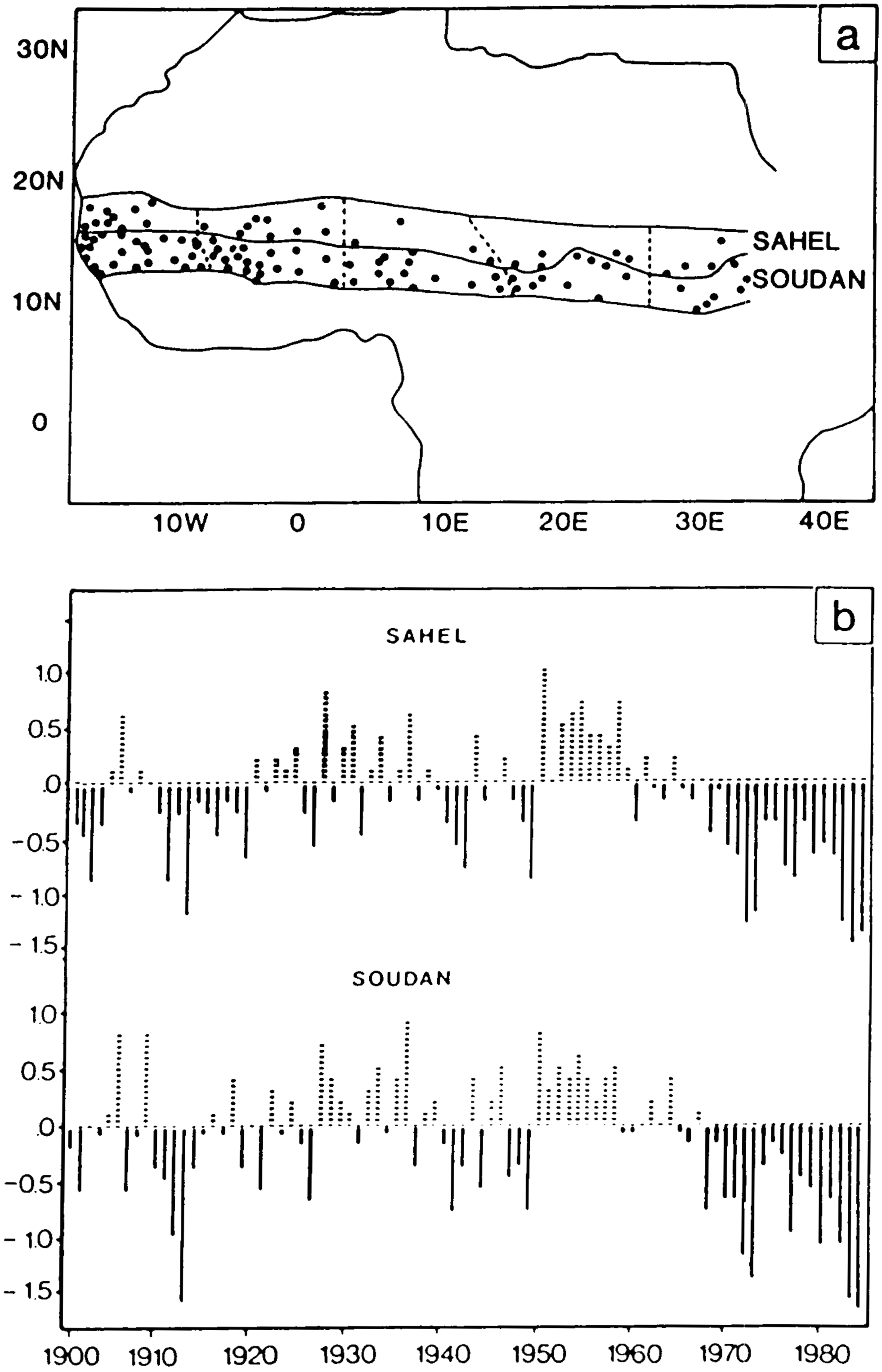

Figure 33 Annual Rainfall Index values for the Soudan and Sahel belts of sub-Saharan Africa. Top panel: Station distribution. Bottom panel: Rainfall Index anomalies. (Courtesy of Nicholson, 1985).

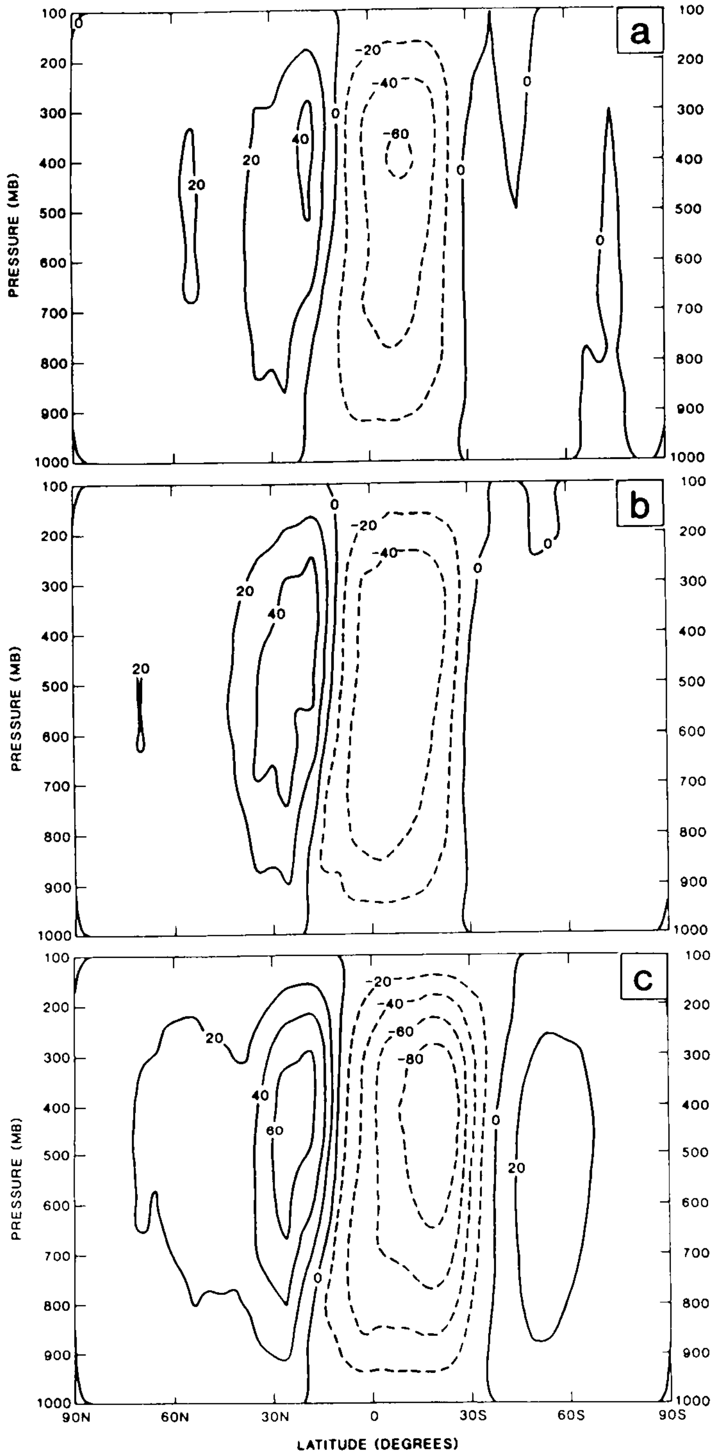

Figure 34 African Sector Hadley cell (10^9 kg sec^{-1}) for July for prescribed sea-surface temperature anomalies: (a) warm phase El Nino scale anomalies from 40S to 60N as observed in July 1983, (b) Climatological normal sea-surface temperatures i.e., no anomalies and (c) cold-phase El Nino scale sea-surface temperature anomalies from 40S to 60N as observed in July 1975.

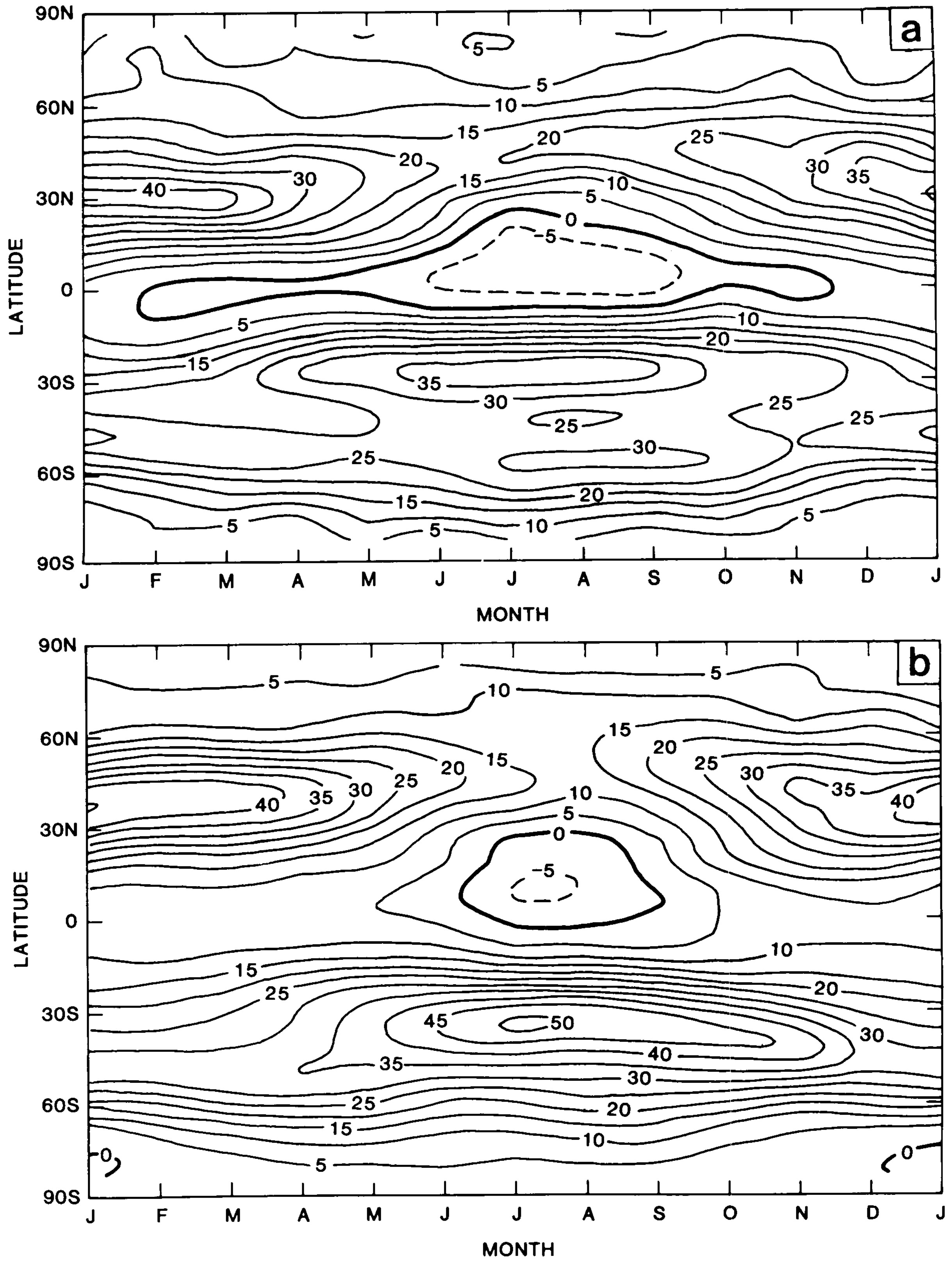

Figure 35 Latitude/time section of monthly mean 200 mb zonal wind. (a) From FGGE observations. (b) From the GCM.

the Equator. As a proxy for precipitation (which tends to be dominated by small scale features), we instead show the upper level (200 mb) velocity potential, which reflects the large-scale divergence pattern. Fig. 36 illustrates the seasonal march of the observed 200 mb velocity potential. The dominant feature is the minimum (associated with upper level divergence) over the Pacific Ocean. The simulated seasonal mean maps of the 200 mb velocity potential (Fig.37) correctly show a region of intense upper level divergence over the Pacific Ocean throughout the year. The gradients are consistently stronger than observed, especially in northern Fall. The simulated seasonal shifts in the position of the upper level divergence center (and the lower level precipitation maximum) are in the right direction for each seasonal transition, but the shifts are not extensive enough. In the GCM, the upper level divergence center in the Pacific tends to cling to the Equator, while in nature, this feature exhibits more seasonal movement. This type of error is also seen in annual cycle integrations with other GCMs.

Fig. 38 shows winter longitude-pressure sections of the observed and simulated stationary eddy fields for the northern winter. There are serious model errors above 200 mb, but the lower and middle levels of the troposphere are well simulated. The stationary and transient eddies are more realistic in Winter than in Summer, and are better simulated for the Northern than the Southern Hemisphere. This is also true of some other GCMs.

Although there are obvious similarities between the simulation and the observations, we have emphasized the discrepancies, since progress in understanding and predicting the atmosphere can only be achieved through the elimination of these errors. In the future we plan to extend our work to a number of other GCMs. We hope that our effort will stimulate other modeling groups to report more fully on their simulations of the seasonal cycle.

V. OBSERVING SYSTEM SIMULATION EXPERIMENTS (R. Atlas)

Background

Since the advent of meteorological satellites in the 1960's, a considerable research effort has been directed toward the design of spaceborne meteorological sensors, the development of optimal methods for the utilization of satellite soundings and winds in global-scale models, and an assessment of the influence of existing satellite data and the potential influence of future satellite data on numerical weather prediction. Observing system simulation experiments (OSSE's) have played an important role in this research and in the planning of Data Systems Tests (DST) and the First GARP (Global Atmospheric Research Program) Global Experiment (FGGE). Such studies have aided in the design of the global observing system, the testing of different methods of assimilating satellite data, and in assessing the potential impact of satellite data on weather forecasting.

The earliest simulation studies proceeded according to the following sequence of steps: First, an artificial history of the atmosphere is created by numerical integration of a model. Second, simulated "data" are created from the history by addition of random variations to the history values for temperature, wind, and pressure. Third, the numerical integration that

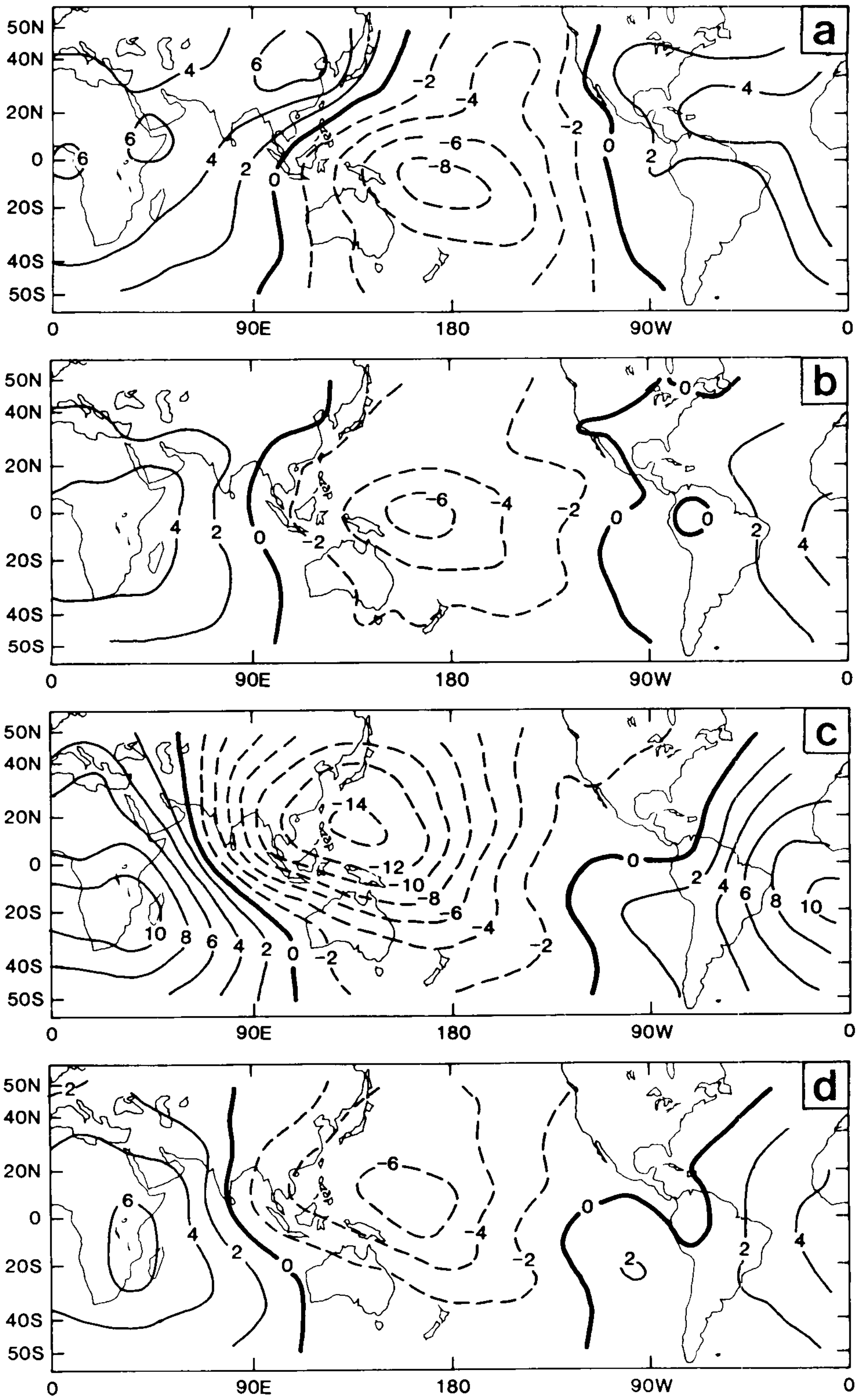

Figure 36 Observed seasonal mean 200 mb velocity potential. Contour interval is 2 x 10^6 m^2/sec. (a) Dec.-Feb. average, (b) March-May average, (c) June-August average, (d) Sept.-Nov. average.

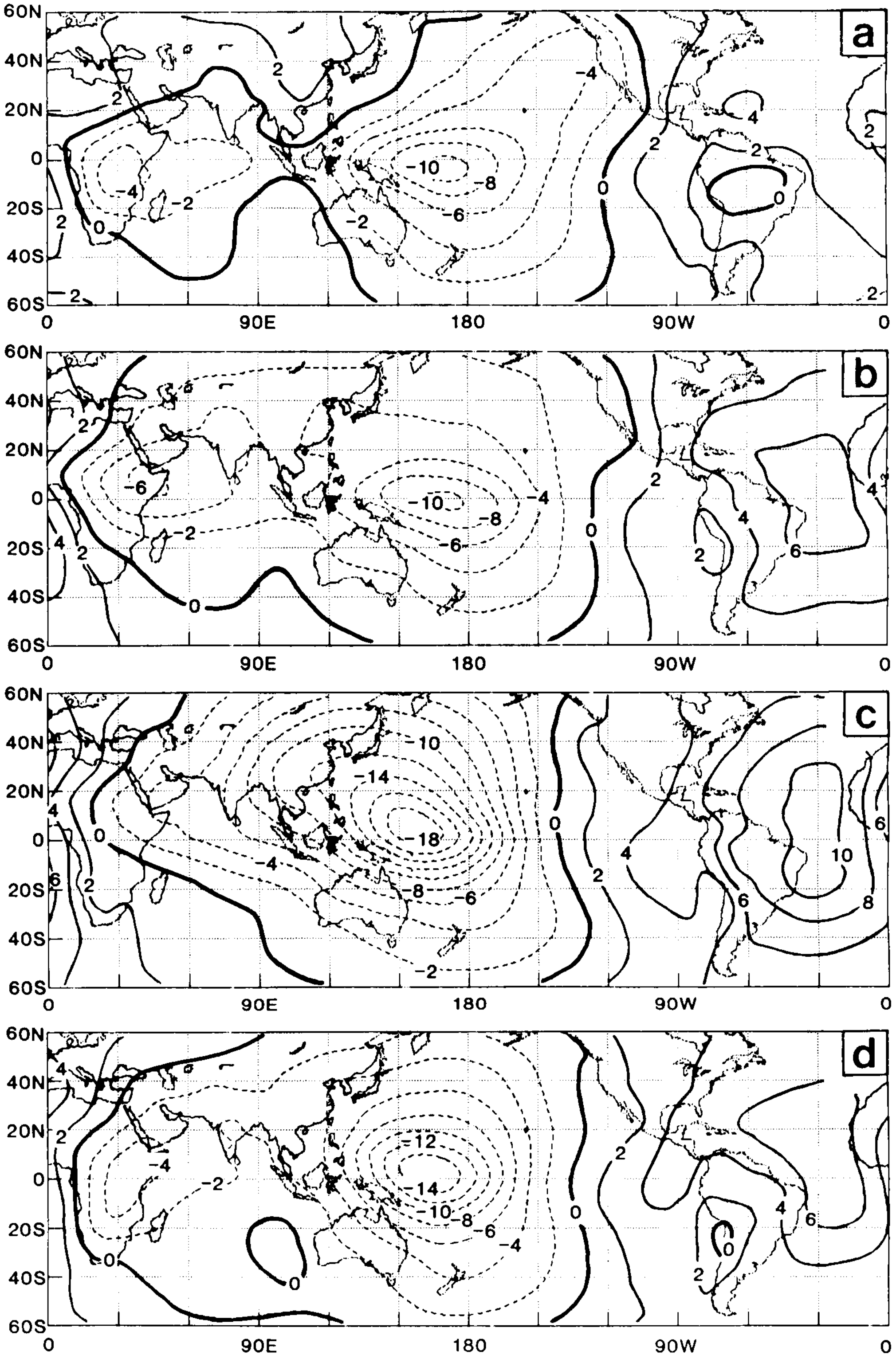

Figure 37 Seasonal mean 200 mb velocity potential from the GCM. The contour interval and seasonal averages are the same as in Figure 36.

**ORIGINAL PAGE IS
OF POOR QUALITY**

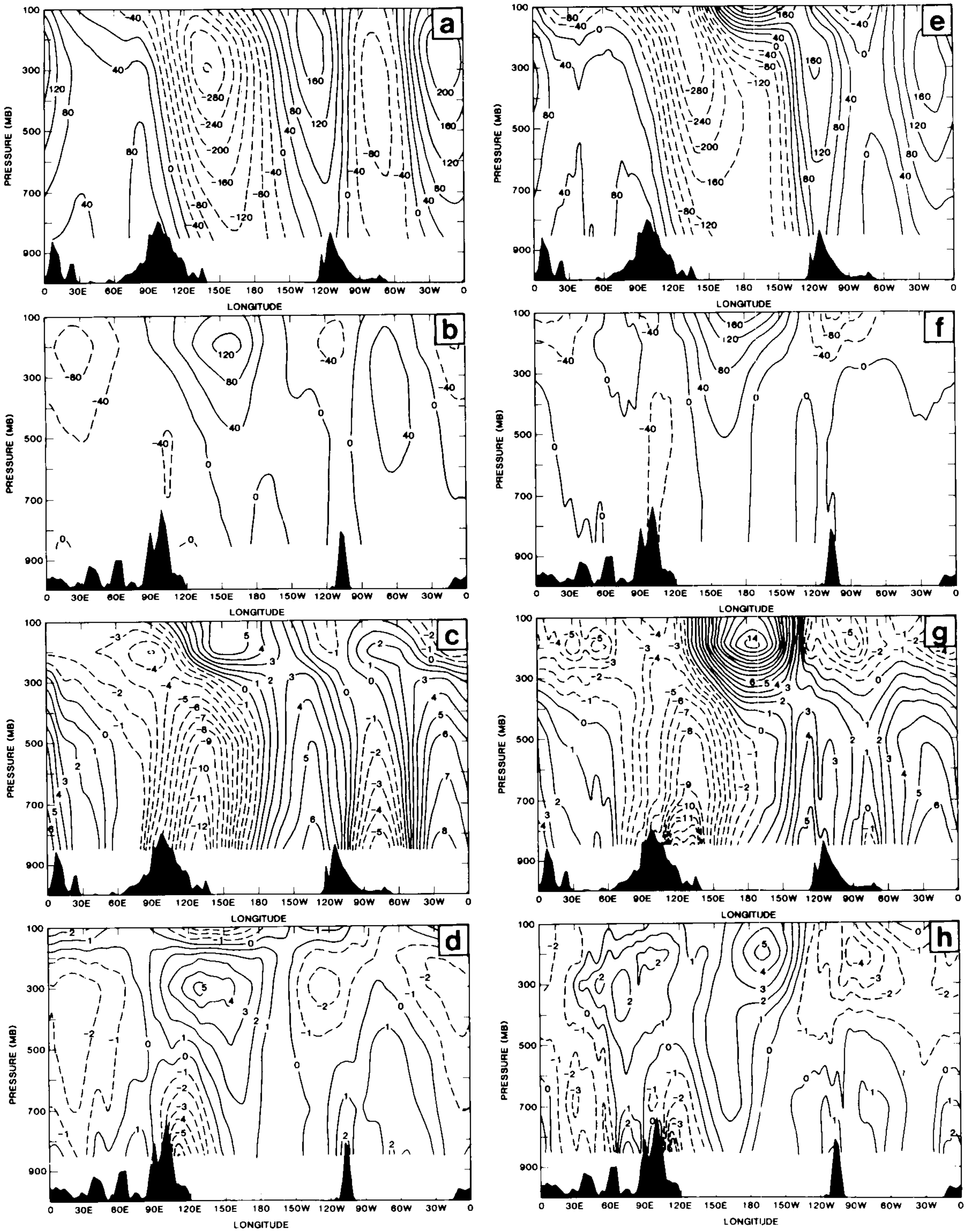

Figure 38 Longitude-pressure section of stationary eddy fields during northern winter (Dec.-Feb. average). (a) and (b) show the observed eddy height field at 46 and 26 degrees North, while (c) and (d) show the observed eddy temperature field at 46 and 26 degrees North. Panels (e)-(h) show the corresponding fields for the GCM. Local topography is indicated in black.

created the history is repeated, but with the meteorological variables in the model replaced by the simulated data at locations and times corresponding to the assumed pattern of observations.

If the data had no errors, and therefore were identical with the history values, and were inserted at all grid points, the new integration would be identical with the history. However, when errors are present, the inserted data perturb the simulated atmospheric circulation, and cause it to depart from the history. The difference between the history and the perturbed circulation resulting from the data insertion is a measure of the effect of the errors in the simulated data. The effect of the errors usually is expressed in terms of differences of the meteorological variables, such as wind components, averaged over all points of the model grid. These differences are considered to represent the errors in the determination of global atmospheric states resulting from the assumed errors in the observing system.

In order to simulate different types of data and data coverage and assess their impact on forecasting skill, a somewhat different approach has been utilized. In this procedure a forecast model is integrated for a long period, such as one or two months. This long run is then assumed to be the true atmosphere or "nature". "Observations" are then extracted from the nature run, following a suitable geographical and temporal distribution, and random "observational" errors are added. These simulated observations are then assimilated with an analysis cycle, and the same model is used as a "forecast model" from the analyzed fields.

An examination of the underlying rationale for the simulation studies as previously conducted, as well as a comparison of the results of these studies with the results of subsequent real data impact tests, indicated several important limitations. The most important weakness of these so-called "identical twin experiments" stems from the fact that the same numerical model has been used both to generate the simulated observations and to test the effectiveness of these observations. Other weaknesses relate to the model-dependence of the studies and the specification of observational errors as random.

The real data impact studies have also indicated that major deficiencies in the global observing system still exist and that current satellite sounders are far from optimal. Advanced passive infrared and microwave sounders and active scatterometer and lidar sounders in a variety of combinations have recently been proposed to improve the accuracy of satellite observations and extend the useful range of numerical weather prediction. Realistic observing system simulation experiments are required to determine which of the proposed instruments will provide the greatest improvements, as well as the optimal design of the future global observing system.

Current Simulation Studies

Recently, an advanced analysis/forecast simulation system has been developed and this system is now being used in a cooperative effort between the European Centre for Medium Range Weather Forecasts, the National Meteorological Center, and the Goddard Laboratory for Atmospheres to begin to provide a quantitative assessment of the potential impact of proposed observing systems on large scale numerical weather prediction. The analysis/forecast simulation system consists of four elements. First, an atmospheric model integration to provide a complete record of the "true" state of the atmosphere called the "nature" or "reference atmosphere". This record is then used to fabricate observational reports and to evaluate analyses and forecasts. Second, a conventional data assimilation cycle that is used as the "control experiment." The control experiment is like an operational analysis/forecast cycle based on conventional observations, except that it makes use of fabricated conventional data obtained from the nature run to produce the analyzed fields. Third, a satellite data assimilation that differs from the control in also including fabricated satellite data in the analysis/forecast cycle. Fourth, forecasts produced from both control and satellite initial conditions. Comparison of these forecasts with the nature provides an assessment of the impact of satellite data.

Two important considerations are involved in the design of the assimilation runs: the nature of the initial conditions and the forecast model used. In reality, short-range forecasts have errors stemming from three different sources: (1) inaccuracy of the initial state, (2) model errors that can be ascribed to numerical truncation (horizontal and vertical truncation errors due to insufficient resolution), and (3) model errors that can be ascribed to the "physics" of the model. The latter include parameterization of subgrid processes like radiation, cumulus convection, and friction, as well as sources of external forcing, like orography, sea/land contrast, and even the use of an artificial rigid top boundary condition common to all numerical models.

For realistic simulation studies, all three sources of errors should be simulated. In most previous simulation experiments, the same model was used to produce the nature run and the assimilation runs and forecasts. Therefore, the errors in the forecasts were due only to errors in the initial conditions. This method (described earlier and referred to as an "identical twin experiment") has the apparent advantage that it isolates the effect of initial data errors and avoids both "numerical" and "physical" errors. On the other hand, it has a very important shortcoming: since the model and "nature" have the same climatology, the accuracy of the simulated forecasts may be far superior to the accuracy of real forecasts. As a result, the external error growth due to the fact that current models are only approximations of the atmosphere is not present in the "identical twin" experiments. This has the effect of increasing the skill of conventional forecasts at low levels of data coverage, because the perfect forecast model is able to "fill up" data gaps. Consequently, at low levels of data, the impact of an observing system is overestimated, whereas the impact of high levels of data, such as provided by satellites, can be underestimated.

Finally, if simulation studies are to provide an accurate indication of how simulated data will influence forecasts in the real world, the simulated observational error characteristics should be realistic. For simulated observational errors to be representative of real observational errors, they should be introduced at actual observing locations and should not be just white noise. Random errors with a standard deviation on the order of GARP errors saturate the spectrum at high frequencies and their effect is mostly averaged out. Horizontal and vertical correlations of error and their dependency on the synoptic situation should be introduced appropriately.

In the simulation studies that we are currently performing, we have attempted to minimize some of the difficulties of the earlier studies by (1) using different models in generating the nature run and in data assimilation and forecasting, (2) simulating both conventional and satellite observations more realistically , and (3) calibrating the simulation results against real data impact experiments.

Recent Results

Experiments have been conducted to calibrate the simulation system and determine its realism, and to begin to assess the impact of a wind profile observing system relative to the impact of satellite temperature sounding data and/or cloud-track winds. To this end, both real data and simulated data assimilation cycles were performed for the period from 0000 GMT 10 November to 0000 GMT 25 November 1979. The real data experiments included a Control cycle in which only conventional data were assimilated, and a FGGE cycle in which conventional and special FGGE data sets including TIROS-N temperature soundings and geostationary satellite cloud-track winds were assimilated. The main simulated data assimilation experiments consisted of corresponding Control and FGGE cycles, as well as a Control plus TIROS-N temperature profiles experiment, a control plus cloud-track winds, and a Control plus wind profiles.

Figure 39 summarizes the results for these initial simulation experiments. S_1 skill scores, averaged for eight forecast cases, are presented for the Southern Hemisphere. These results show a significant improvement in Southern Hemisphere forecast accuracy resulting from the assimilation of simulated satellite wind profile data, and indicate that wind profile data are more effective than temperature data in controlling analysis errors. In the Northern Hemisphere, the influence of simulated wind profiles was smaller, but on occasion, showed a significant positive impact. Figure 40 presents an example of a 5-day forecast of a cyclone over the Great Lakes that was substantially improved by the use of wind profile data.

In addition to these experiments, a number of preliminary simulation experiments have been conducted in order to assess the potential influence of high quality surface wind data, such as might be obtained by the planned NASA or ESA scatterometers, on Southern Hemisphere analyses and numerical forecasts. These experiments consisted of five assimilation cycles of five days duration and a five-day forecast from each and included: a "Control", in which only simulated conventional data were assimilated, a Control plus 1000 mb winds, a Control plus 1000 and 850 mb winds, a Control plus 1000, 850, and 700 mb winds, and a Control plus complete wind profiles (1000-100 mb), in which perfect simulated winds at TIROS-N locations and at each of the mandatory levels between 1000 mb and 100 mb were assimilated in conjunction with all conventional data.

These experiments were designed to test the improvement in analysis and forecast impact which might be obtained if surface wind data were effectively used to modify 850 mb or both 850 and 700 mb wind analyses, as well as the impact of such data relative to that which might be obtained with a lidar wind

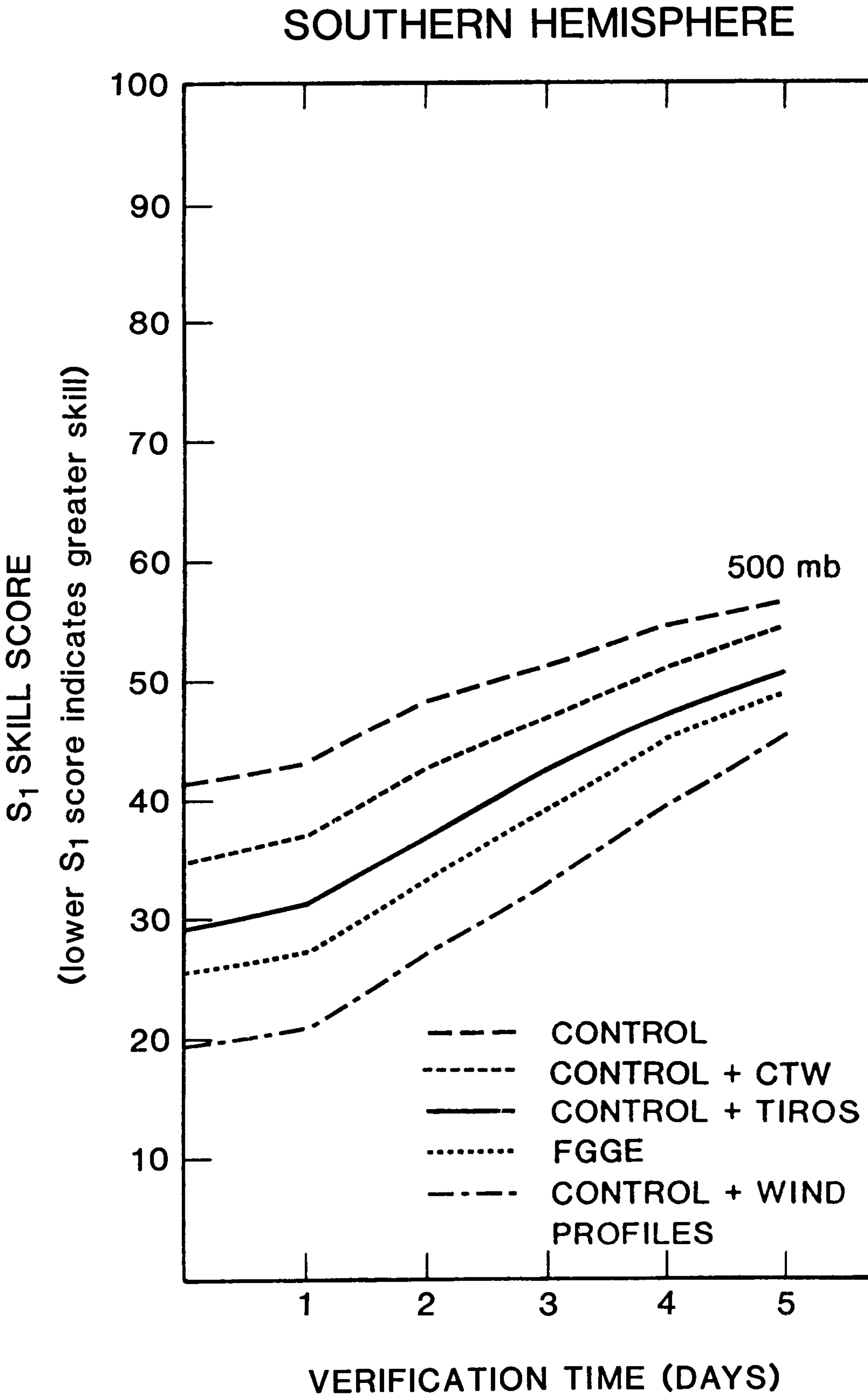

Figure 39 Impact of simulated data on Southern Hemisphere 500 mb height forecasts

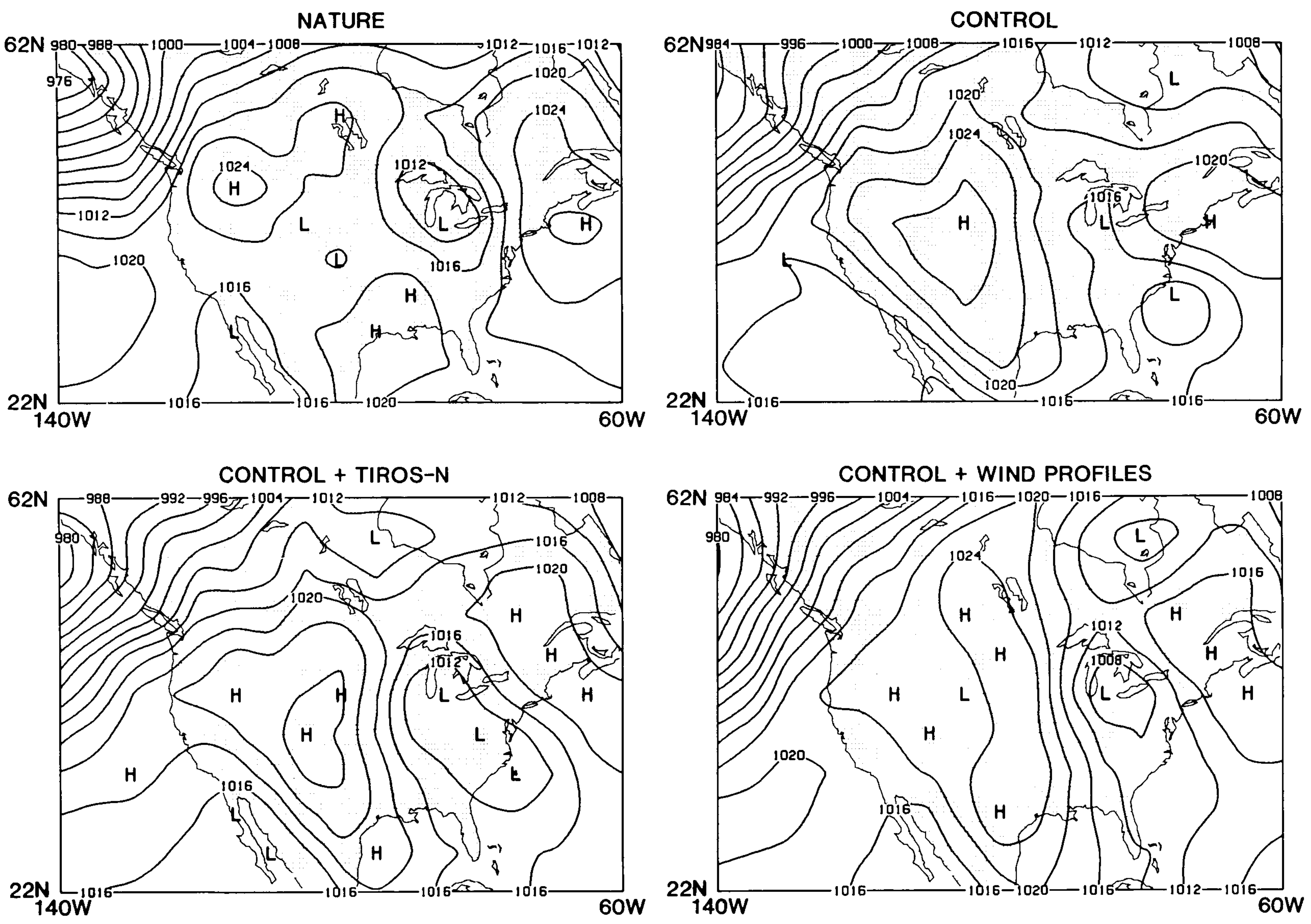

Figure 40 Simulated 5-day sea-level pressure forecasts from 23 November 1979 and the corresponding nature field for verification.

profiler.

Figure 41 shows the impact of 1000 mb, 1000 mb - 850 mb, 1000 - 700 mb, and complete wind profiles on 500 mb height analyses for a portion of the Southern Hemisphere after 120 h of data assimilation, while Fig. 42 shows the impact of these winds on S_1 skill scores for a forecast of sea level pressure, verified over the entire Southern Hemisphere. As indicated by the figures, the impact of surface wind data on analyses and forecasts would be significantly enhanced if procedures were developed to accurately extend their influence to 850 and 700 mb. However, this impact would still be substantially less than that which could be obtained with a complete wind profiler system.

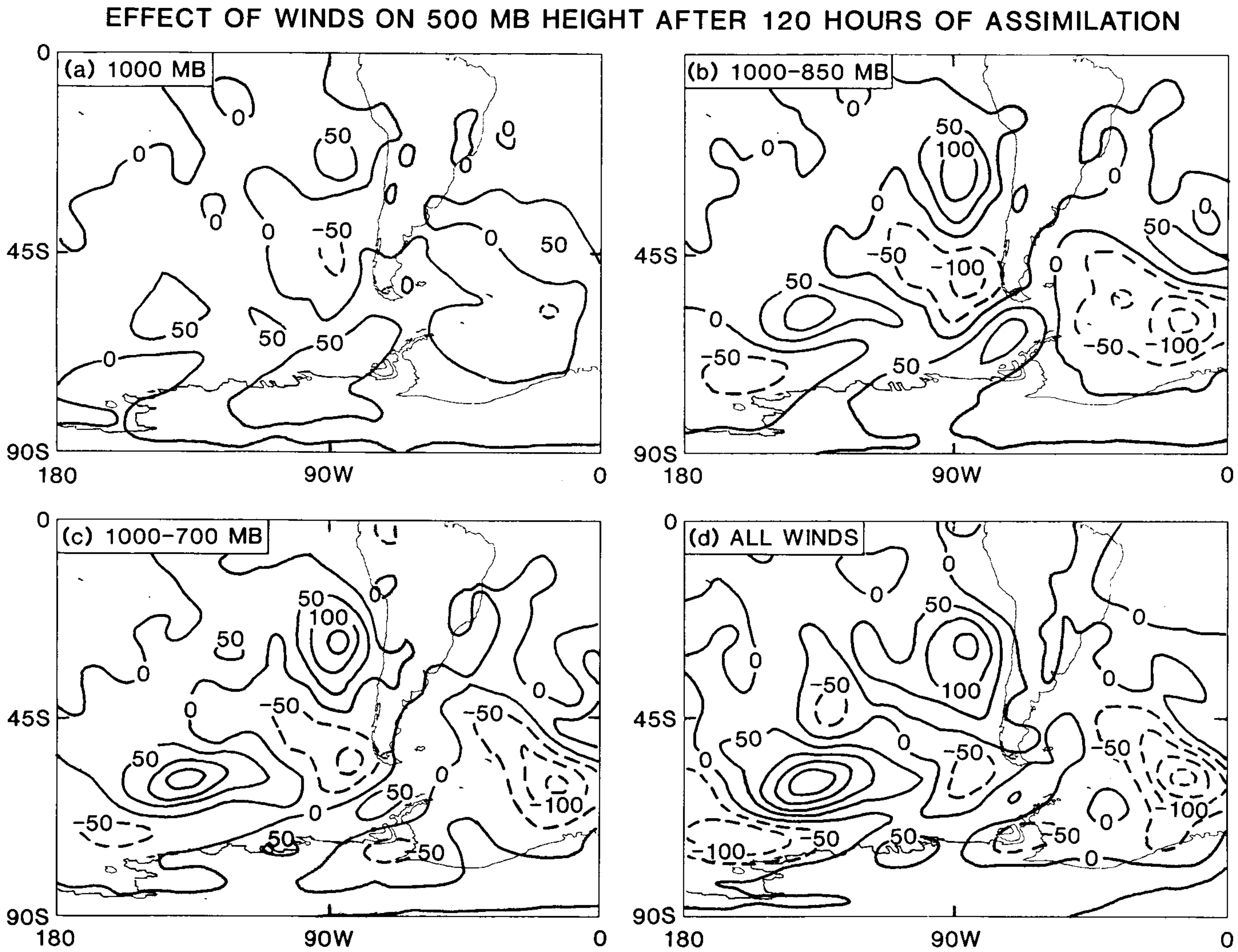

Figure 41 Difference from control of (a) control plus 1000 mb winds, (b) control plus 1000-850 mb winds, (c) control plus 1000-700 mb winds and (d) control plus complete wind profiles after 120 hours of assimilation.

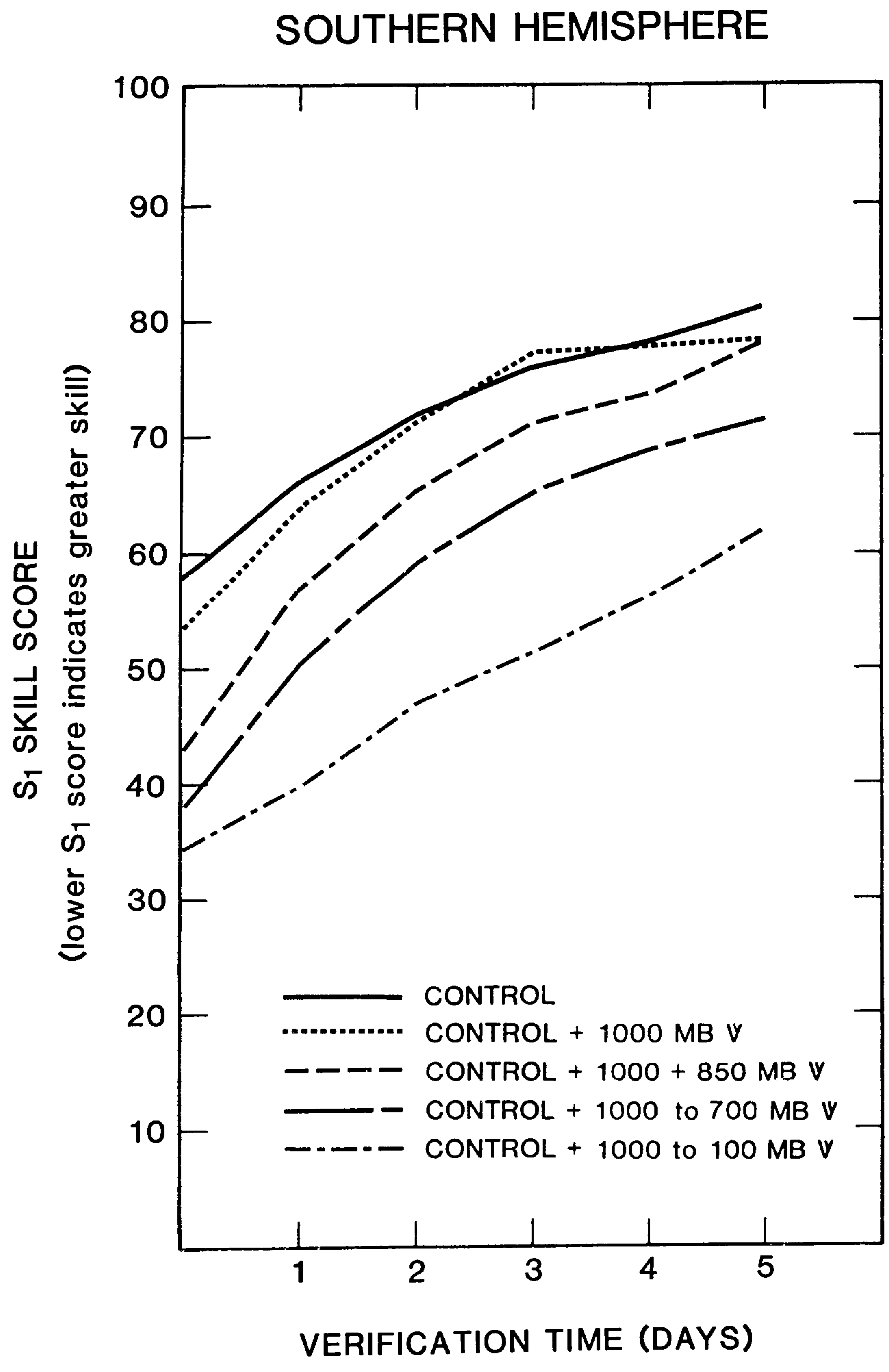

Figure 42 Impact of low level winds relative to full wind profiles on Southern Hemisphere sea level pressure forecasts.

References

Arakawa, A., and W. H. Schubert, 1974: Interaction of a cumulus cloud ensemble with the large-scale environment, Part I. J. Atmos. Sci., 31, 674-701.

Atlas, R., A. J. Busalacchi, M. Ghil, S. Bloom and E. Kalnay, 1987: Global surface wind and flux fields from model assimilation of Seasat data. J. Geophys. Res., 92, 6477-6487.

Baker, W. E., 1983: Objective analysis and assimilation of observational data from FGGE. Mon. Wea. Rev., 111, 328-342.

Baker, W. E., S. C. Bloom, J. S. Woollen, M. Nestler, E. Brin, T. W. Schlatter and G. W. Branstator, 1987: Experiments with a three dimensional statistical objective analysis scheme using FGGE data. Mon Wea. Rev., 115, 272-296.

Kalnay, E., R. Balgovind, W. Chao, D. Edelmann, J. Pfaendtner, L. Takacs and K. Takano, 1983: Documentation of the GLAS Fourth Order General Circulation Model, NASA Technical Memorandum 86064 [NTIS N8424028].

Krishnamurti, V., 1982: The Documentation of the Wu-Kaplan radiation parameterization. NASA Tech. Memo 83926, NASA/Goddard Space Flight Center, Greenbelt, MD 93 pp.

Lau, K. M., G. J. Jang and S. H. Shen, 1986: Seasonal and interseasonal climatology of summer monsoon or rainfall over east Asia. Institute of Atmospheric Physics, Academia Sinica, Beijing, People's Republic of China, 1-14.

McFarlane, N. A., 1987: The effect of orographically excited gravity wave drag on the general circulation of the lower stratosphere and troposphere. J. Atmos. Sci., 44, 1775-1800.

Palmer, T. N., G. J. Shutts and R. Swinbank, 1986: Alleviation of a systematic westerly bias in general circulation and numerical weather prediction models through an orographic gravity wave drag parameterization. Quart. J. R. Met. Soc., 112, 1001-1039.

Reuter, D., J. Susskind and A. Pursch, 1988: First guess dependence of physically based temperature humidity-retrievals from HIRS2/MSU data. J. Atmos. Ocean. Tech., in press.

Reynolds, R., 1982: A monthly averaged climatology of sea surface temperature. NOAA Tech. Rep. NWS 31.

Susskind, J., J. Rosenfield and D. Reuter, 1983: An accurate radiative transfer model for use in the direct physical inversion of HIRS2 and MSU temperature sounding data. J. Geophys. Res., 88C, 8550-8568.

Susskind, J., J. Rosenfield, D. Reuter and M. T. Chahine, 1984: Remote sensing of weather and climate parameters from HIRS2/MSU on TIROS-N. J. Geophys. Res., 89D, 4677-4697.

Susskind, J., and D. Reuter, 1985: Retrieval of sea-surface temperatures from HIRS2/MSU. J. Geophys. Res., 90C, 11602-11608.

Susskind, J., D. Reuter and M. T. Chahine, 1987: Cloud fields derived from analysis of HIRS2/MSU sounding data. J. Geophys. Res., 92, 4035-4050.

Takano, K., W. E. Baker, E. Kalnay, D. J. Lamich, J. E. Rosenfield and M. Geller, 1987: Forecast experiments with the NASA/GLA Stratospheric/tropospheric data assimilation system. Short and Medium-Range Numerical Weather Prediction, Collection of Papers Presented at WMO/IUGG NWP Symposium, Tokyo, 4-8 August 1986, 83-89.

Walker, G. K., and Y. Mintz, 1988: Atlas of surface-measured precipitation December 1978 - November 1979 - the FGGE year. (In preparation).

NASA
National Aeronautics and
Space Administration

Report Documentation Page

1. Report No. NASA TM-4085	2. Government Accession No.	3. Recipient's Catalog No.

4. Title and Subtitle

Research Highlights of the Global Modeling and
Simulation Branch for 1986-1987

5. Report Date

December 1988

6. Performing Organization Code

611.0

7. Author(s)

Wayman Baker, Editor; Joel Susskind, James Pfaendtner,
David Randall, and Robert Atlas, Co-editors

8. Performing Organization Report No.

88B0279

10. Work Unit No.

9. Performing Organization Name and Address

Goddard Space Flight Center
Greenbelt, Maryland 20771

11. Contract or Grant No.

13. Type of Report and Period Covered

Technical Memorandum

12. Sponsoring Agency Name and Address

National Aeronautics and Space Administration
Washington, D.C. 20546-0001

14. Sponsoring Agency Code

15. Supplementary Notes

Wayman Baker, Joel Susskind, David Randall, and Robert Atlas: Goddard Space Flight Center, Greenbelt, Maryland.
James Pfaendtner: Sigma Data Services Corporation, Reston, Virginia.

16. Abstract

This document provides a summary of the research conducted in the Global Modeling and Simulation Branch and highlights the most significant accomplishments in 1986-1987. The Branch has been the focal point for global weather and climate prediction research in the Laboratory for Atmospheres through the retrieval and use of satellite data, the development of global models and data assimilation techniques, the simulation of future observing systems, and the performance of atmospheric diagnostic studies.

17. Key Words (Suggested by Author(s))

Satellite Retrievals, Numerical Weather
Prediction, Climate Observing System
Simulations

18. Distribution Statement

Unclassified - Unlimited

Subject Category 47

19. Security Classif. (of this report)	20. Security Classif. (of this page)	21. No. of pages	22. Price
Unclassified	Unclassified	80	A09

NASA FORM 1626 OCT 86